Reynolds Number Effects on Mixing in the Turbulent Shear Layer

Thesis by

Christopher Llewellyn Bond

In Partial Fulfillment of the Requirements

for the Degree of

Doctor of Philosophy

California Institute of Technology

Pasadena, California

1999

(Submitted October 3, 1997)

Acknowledgements

Many people helped with this work, but I will only list the most influential here:

- I first would like to thank Mr. Earl Dahl, without whom none of these experiments could have been performed.
- My fellow student Mike Slessor provided both insightful discussions of the work and significant help with the schlieren system.
- Norm Keidel and Mike Gerfen of Caltech's Central Engineering Services provided much needed help with the design of the facility upgrade.
- The members of the Aeronautics shop performed a number of smaller machining jobs required for these experiments, often on short notice.
- I would also like to thank my advisor, Paul Dimotakis, for his help in distilling conclusions from the frequent and often perplexing problems encounterd over the years.

Abstract

Experiments have been performed in turbulent shear layers to assess the effects of Reynolds number on mixing. The experiments extend the upper range of incompressible, chemically-reacting flow data from 1.6×10^5 to 3.5×10^5 and, in a subsequent collaboration with M. Slessor and others, to 7×10^5. The experiments address an ambiguity in recent measurements of mixing in compressible shear layers, whose differences from measurements in incompressible shear layers could have been due either to compressibility or Reynolds number effects. The current results, collectively with previous results, show that the decrease of mixing with increasing Reynolds number first seen by Mungal *et al.* (1985) continues to the Reynolds numbers studied, but do not show a further decrease in mixing. The conclusions must be tempered by the presence of changes in the initial boundary layers and acoustic environment, and by the compressibility ($M_c = 0.25$) of the highest Reynolds number ($Re = 7 \times 10^5$) case.

Contents

Figures

Tables

Chapter 1 Introduction

The planar shear layer, both incompressible and compressible, has been investigated as an example of a simple, turbulent-mixing flow. The current research and the related one-and-a-half decade effort on molecular mixing and chemical reactions preceding it have been driven by the idea that to understand turbulent molecular mixing in general it would be helpful to understand the behavior of a conceptually simple turbulent flow. Molecular mixing is of interest both because it represents mixing at the molecular scale (as required for non-premixed combustion) and because it is a result of dynamics at all scales of the turbulent flow. As such, it represents a challenge for turbulence modeling, and represents features of the flows that models and computations must correctly represent to predict reacting flows. A relatively recent review (Dimotakis 1991) discusses molecular mixing and related issues, including growth rate, heat release, Schmidt number effects,*etc.*

The Reynolds number, Re, is, in general, defined as $Re \equiv \rho U L/\mu$, where ρ is the density, U is the characteristic velocity, L is the characteristic length and μ is the viscosity. For the values referred to in this work the density and viscosity of a unreacted mixture of the freestream gases is used. The velocity scale for the shear layer is the difference of the freestream velocities, $\Delta U = U_1 - U_2$ (the shear across the layer). The appropriate length scale is the local thickness, $\delta(x)$, of the layer. Re_x is also used, based on the downstream distance, x, where the measurements are taken. In discussion of initial conditions, another Reynolds number is also used, Re_θ, the boundary layer Reynolds number, where the velocity, U, is the free stream velocity and the length is the momentum thickness, θ, of the boundary layer.

The effects of Reynolds number, which this work attempts to address, are, in one sense, weak. Past the mixing transition (Konrad 1976; Koochesfahani & Dimotakis 1986), a large change in Reynolds number is needed to significantly affect mixing in the shear layer. Meanwhile, inlet boundary layers, the splitter plate wake, acoustic

forcing, and acoustic feedback within the flow can all have stronger effects on the flow (Dimotakis 1991). However, between the mixing transition and the highest Reynolds numbers realized in experiments, there is a three-decade change in Reynolds number. The difference between these experiments and actual applications may be similarly large. As a consequence, Reynolds number effects must be considered, since, with the large range possible in Reynolds number, the effects may be significant.

The current work attempts to assess these Reynolds number effects. It also clearly demonstrates the sensitivity of the flow to other influences. As was shown in subsequent work (Slessor *et al.* 1998), at selected flow conditions the flow can depend significantly on the initial conditions with tripped and untripped splitter-plate boundary layers causing significant changes in molecular mixing far downstream.

1.1 Previous work on molecular mixing

1.1.1 Methods

Historically, the first attempts to measure the fluid composition in free shear layers were made using the passive-scalar method (Fiedler 1974, Konrad 1976, Batt 1977, Rajagoplan & Antonia 1981), and have continued, often in conjunction with chemical-reaction methods (Koochesfahani & Dimotakis 1986, Masutani & Bowman 1986, Karasso & Mungal 1996). A marker, e.g., temperature, fluorescent dye, *etc.*, is placed in one of the two streams of the shear layer and is then monitored downstream to measure the fluid composition. Even if under-resolved, these measurements can provide accurate average values of the concentration. To estimate the amount of mixed fluid, the measurement needs to resolve the smallest scales of the scalar field. Failure to resolve these smallest scales can significantly overstate the mixed fluid amount (Breidenthal 1981, Koochesfahani & Dimotakis 1986, Clemens & Paul 1995, Karasso & Mungal 1996).

To avoid resolution difficulties, especially since it is effectively infeasible to fully resolve the flow at very high Reynolds numbers, it is necessary to use a diagnostic

whose response can be used to distinguish between mixed and unmixed (but possibly well-stirred) fluid. With such a diagnostic, underresolved measurements will register the average response, which for such a diagnostic is not the average fluid composition, as it is for passive scalar measurements.

Measuring the product formed by chemical reactions eliminates the difficulty of mistaking unmixed fluid as mixed fluid, since product is only formed where fluid is molecularly mixed (Breidenthal 1981, Koochesfahani & Dimotakis 1986). For an ideal, mixing-limited chemical reaction, the amount of product only depends upon the amount of mixed fluid, the composition of the mixed fluid, and the reactants in the two streams. With fast chemistry, a pair of experiments, known as a "flip" experiment (Koochesfahani *et al.* 1985, Koochesfahani & Dimotakis 1986), can be used to measure molecularly-mixed fluid. In practice, infinitely-fast chemical reactions do not exist, so the measurements depend upon reactions that are sufficiently faster than the mixing process (high Damköhler number limit).

Another method for separating the mixed and unmixed fluid is the "cold chemistry" method (Paul & Clemens 1993, Clemens & Paul 1995, Island 1997). This method measures the laser-induced fluorescence of NO. One stream is seeded with NO, while the other side carries a significant percentage of O_2. Since the electronic transition stimulated is also de-excited collisionally by O_2, the fluorescence (primarily) indicates the presence of unmixed fluid from the NO-seeded freestream. The results from a pair of such experiments can be combined, allowing the mixed-fluid to be inferred by subtracting the pure freestream fluid from the total fluid. Combined with a passive scalar measurement, such a pair can also be used to infer the average mixed-fluid composition. The three measurements would measure the average amount of unmixed high-speed freestream fluid, the average amount of unmixed low-speed freestream fluid, and the average composition, allowing the average mixed-fluid composition to be measured by compensating the average composition for the effects of the unmixed fluid.

1.1.2 Reynolds number effects

Konrad (1976) made the first measurements of the mixed-fluid composition in a turbulent free mixing layer. He found that the mixed fluid was dominated by a single composition apparently related to the large-scale structure of the flow. Even with equal-density freestreams, the mixed fluid composition was biased towards the high-speed fluid. Konrad also found that the flow went through a mixing transition where the mixed fluid fraction significantly increased, at a Reynolds number (Re) around 2×10^4.

Mungal *et al.* (1985) investigated the effects of Reynolds number on product formation in the gas-phase mixing layer. They found a decrease of product fraction with increasing Reynolds number, with the product fraction decreasing by 6% for each factor of two increase in Reynolds number. These experiments were performed at a single stoichiometric ratio (here defined as the number of moles of high-speed fluid needed to fully consume one mole of low-speed fluid), $\phi = 1/8$, which limits the ability to relate the results to overall molecular mixing. The decreasing product fraction seen in the experiments could have been caused by decreasing molecular mixing, or by a change in the composition of the mixed fluid.

Koochesfahani & Dimotakis (1986) made measurements in a high Schmidt number (Sc) liquid-phase mixing layer, using laser-induced fluorescence. The Schmidt number is defined as the ratio of viscous diffusion (of momentum) to molecular diffusion, $Sc \equiv \nu/\mathcal{D}$, where $\nu = \mu/\rho$ is the kinematic viscosity and where $\mathcal{D}$ is the mass diffusivity. Typical values are $Sc \sim 1000$ for liquid-phase flows and $Sc \sim 1$ in gas-phase flows. These measurements were made using a reversible (acid-base) reaction and a pH-sensitive dye. The "flip" experiment, using a pair of these chemically-reacting flows, gave measurements of the product and mixed-fluid fraction. A flip experiment was performed at conditions slightly beyond the mixing transition ($Re = 2.3 \times 10^4$), as well as an additional chemical-product measurement at a higher Reynolds number. The "flip" experiment showed asymmetric product formation (indicating a non-unity entrainment ratio), but nearly symmetric product profiles, with the peaks of the two

product profiles at the center of the mixing layer, indicating a uniform mixed-fluid composition across the mixing layer. The higher-Reynolds number case showed little or no change in product formation, indicating a weak (or non-existent) dependence of product formation on Reynolds number.

Frieler & Dimotakis (1988) performed a study of mixing in inhomogeneous mixing layers and found that, although the mixed fluid composition of the shear layer was significantly affected by the freestream density ratio, the molecularly-mixed-fluid fraction was almost independent of the density ratio. This result is of interest in the context of the Mungal *et al.* (1985) experiments, since the decrease in product they observed represents an incomplete measure of mixing.

Frieler (1992) performed a series of experiments to look at the effects of Reynolds number on molecular mixing. These experiments used the same facility and method as the Mungal *et al.* (1985) experiments, but were performed at both $\phi = 1/8$ and $\phi = 8$. By performing "flip" experiments, the molecular mixing was measured, with a significantly smaller effect of Reynolds number on molecular mixing seen. This suggested that the increasing Reynolds number of the flow was altering the composition of the molecularly-mixed fluid, as well as the extent of the molecular mixing.

Karasso & Mungal (1996) made both passive scalar and chemical-reaction measurements in liquid (high-Sc) mixing layers. They confirmed that, at least at higher Reynolds numbers, passive scalar results were seriously affected by resolution problems. The chemically-reacting flow results suggested little change in mixed-fluid fraction as the Reynolds number changed. However, they concluded, from changes in the product profiles, that the Reynolds number (as an indicator of the mixing transition) was insufficient to determine when the flow was fully developed. They used a "pairing parameter" (see references in Karasso & Mungal 1996 for earlier use of this parameter) based on initial boundary layer thickness, downstream position, and velocity ratio. This parameter was then related to the onset of fully-developed mixing.

Slessor *et al.* (1998) later reported that high values of this "pairing parameter" do not guarantee the presence of a unique mixing state. They found that boundary

layer tripping has significant effects well past the values of the "pairing parameter" that were suggested as the onset of fully developed mixing.

Subsequent to the work detailed in this thesis, the range of Reynolds numbers investigated was extended by others in collaboration with the author (Slessor 1998). These experiments are discussed in conjunction with the current results in Chapter 4.

1.1.3 Compressibility or Reynolds number?

Hall *et al.* (1991) made measurements of molecular mixing in compressible shear layers. "Flip" experiments were used to measure molecular mixing in two compressible flows. They found that, at moderate compressibility ($M_c = 0.51$), the molecularly-mixed-fluid fraction was 18% lower than in incompressible shear layer flows. At high compressibility ($M_c = 0.96$, with visible travelling waves), the molecularly-mixed-fluid fraction was reduced further. The difference between the two compressible flows was attributed to the increase in compressibility. These compressible flows were more than one decade higher in Reynolds number than previous incompressible results and it was not certain how much of the difference (in mixing) was due to Reynolds number and how much due to compressibility.

Clemens & Paul (1995) made a pair of measurements in the annular mixing layer of a co-flowing jet. These measurements were made in a low-to-moderately-compressible flow ($M_c = 0.36$) and a more compressible flow ($M_c = 0.83$). They found that the molecularly-mixed-fluid fraction in the lower-compressibility case was comparable to the measurements of Hall *et al.* (1991) at moderate compressibility. However, the higher-compressibility case had an increased molecularly-mixed-fluid fraction, which contrasts with the results of Hall *et al.* (1991). The result at the lower compressibility was compatible with a decrease of molecularly-mixed-fluid fraction with increasing Reynolds number, but the higher compressibility case (which also had a higher Reynolds number) showed either a more complicated dependence on Reynolds number, or a mixture of compressibility and Reynolds-number effects.

Island (1997) performed a series of experiments using the "cold-chemistry" method. These experiments varied in compressibility from relatively low ($M_c = 0.25$) to moderate to high compressibility ($M_c = 0.76$). The lowest compressibility case was obtained by accelerating the flow downstream of the splitter-plate. For all but the highest-compressibility flow, measurements were made at three downstream positions, allowing a measurement of Reynolds number effects without altering the overall flow. The three (lower compressibility) cases showed changes of -4%, $+6\%$ and $+10\%$ for factors of increase in Reynolds number of 2.0, 2.0 and 2.1. Taken as a whole, those data show a 25% increase in mixed-fluid fraction for a factor of increase in Reynolds number of 7.7. However, whether these results show an increase of mixing due to Reynolds number changes, or a more complicated combination of Mach number and Reynolds number effects was not resolved.

Slessor (1998) performed a companion experiment to the high-Reynolds number experiment mentioned in the last section. The two flows were matched very closely in density ratio, velocity ratio and Reynolds number, but had $M_c = 0.25$ and 0.47. Although Slessor saw a significant change in the temperature profiles (and thus the distribution of the mixed fluid), there was only a very slight increase in the mixed fluid fraction at the higher compressibility.

1.2 Models of molecular mixing

Some models are available that address Reynolds number (and Schmidt number) effects . The Broadwell-Breidenthal-Mungal model (Broadwell & Breidenthal 1982, Broadwell & Mungal 1991) attempted to estimate the effects of Schmidt and Reynolds numbers on mixing. Dimotakis (1987) derived a model for molecular mixing assuming a Kolmogorov distribution of diffusion-layer scales.

In the Broadwell-Breidenthal-Mungal model, hereafter referred to as the BBM model, the essential idea was that the mixed fluid is comprised of two parts: well-mixed homogeneous fluid in the rollers (large-scale structures) and diffusion layers between the two freestreams in the braid region. The well-mixed homogeneous fluid

is the result of a cascade of the fluid to the smallest scales, and this cascade is assumed to take a fixed Lagrangian time, approximated as independent of Reynolds number. As a result, in the BBM model, the homogeneously-mixed fluid remains a constant fraction of the layer as the Reynolds and Schmidt numbers change. In contrast, the fraction of fluid in the diffusion layer is not fixed but is proportional to $1/\sqrt{Sc\,Re}$. The resulting PDF is a delta function at the uniform composition with an additional diffusion-layer component. The uniform composition is determined by the entrainment ratio (the ratio of high-speed fluid entrained to low speed fluid entrained), while the absolute amount of mixed fluid in each state is determined by a fit to data, since the model only suggests the behavior of the mixed fluid with changing Reynolds and Schmidt numbers.

The BBM model results in a mixed-fluid volume fraction that decreases algebraically with the product of the Reynolds and Schmidt numbers. For fast chemistry at a fixed stoichiometry and entrainment ratio, the product fraction has the dependence:

$$\frac{\delta_{\mathrm{p}}}{\delta_{\mathrm{T}}}(\phi) = C_1 F_1(\phi) + \frac{C_2 F_2(\phi)}{\sqrt{Sc\,Re}}, \tag{1.1}$$

where F_1 and F_2 are functions only of the stoichiometry. The constants C_1 and C_2 are determined by fit to mixing data. The model was used in Broadwell & Mungal (1991) by fitting two product fraction results: one gas phase at $\phi = 1/8$ from Mungal & Dimotakis (1984), and one liquid phase at $\phi = 1/10$ from Koochesfahani & Dimotakis (1986). The product fraction $\delta_{\mathrm{p}}/\delta_{\mathrm{T}}$ is the fraction of the fluid in the layer which has reacted. It should be noted that the product fraction asymptotes to the value $C_1 F_1(\phi)$ as the Reynolds number goes to infinity, which is due only to the homogeneously mixed fluid. Also, $\delta_{\mathrm{p}}/\delta_{\mathrm{T}}$ is a function of $Pe \equiv Sc\,Re = \Delta U\,\delta/\mathcal{D}$, *i.e.*, not a function of viscosity.

The Dimotakis (1987) model, hereafter referred to as the D87 model, represents the mixed fluid as residing over all scales of the flow. The fluid resides in diffusion layers at all scales of the flow which are described assuming Kolmogorov-type distribution of strain rates. Normalizing over all scales produces a logarithmic dependence

of the mixed-fluid volume fraction on Reynolds number. The model also describes Schmidt number effects, but the dependence is more complicated. For fast chemistry at a fixed stoichiometry, the product fraction has the form:

$$\frac{\delta_{\mathrm{P}}}{\delta_{\mathrm{T}}}(\phi) = \frac{A(\phi, Sc)}{B(\phi, Sc) + \log(Re)}, \tag{1.2}$$

where A and B are analytic functions of both Schmidt number, Sc, and stoichiometry. These functions are determined without fits to mixing data. As the Reynolds number increases, the product fractions asymptote to zero at infinite Reynolds number, albeit slowly.

Both of the models require, as an input, a large-scale entrainment ratio, E_{v}. Both were calculated using fluids of equal temperature and diffusivity. Finally, neither model considers mixing between previously mixed fluid and unmixed fluid, but instead each only considers mixing between the two freestreams.

1.3 Overview

Chapter 2 discusses the use of the $(H_2+NO)/F_2$ chemical system as an indicator of molecular mixing. Chapter 3 discusses issues and choices in the design of the experiments performed for this work.

Chapter 4 discusses the high-Reynolds-number, incompressible experiments, their results, and comparison of these results to previous and subsequent work. These experiments extend the upper limit range of Reynolds numbers, Re_δ, covered by chemically-reacting incompressible-flow experiments from 1.5×10^5 to 3.5×10^5.

Chapter 5 presents the conclusions drawn from the current work. Appendix A discusses the Supersonic Shear-Layer facility (S^3L) and recent modifications. Appendix B discusses the acquisition and processing of the data. Appendix C provides a detailed description of the experiments from which the data in Chapter 4 were derived.

Chapter 2 Chemistry

2.1 The $(H_2+NO)/F_2$ chemical system

The facility used in this investigation, the GALCIT Supersonic Shear-Layer Facility (S^3L), is designed to use the $(H_2+NO)/F_2$ chemical system. A discussion of this chemical system is given in Mungal (1983) and Hall (1991). This chemical system was selected for its fast chemical kinetics and hypergolic behavior. The fast chemical kinetics enable the use of dilute concentrations and relatively low heat release tc infer molecular mixing in non-reacting flows. Specifically, dilute quantities of H_2 (1-16%) and NO (0.06-1%) are placed in one stream of the flow, while the other stream holds dilute quantities of F_2 (2-8%). This chemistry has been used in previous experiments by Mungal & Dimotakis (1984), Mungal *et al.* (1985), Frieler & Dimotakis (1988), Hermanson & Dimotakis (1989), Hall *et al.* (1991), and Frieler (1992). Egolfopoulos *et al.* (1996) used this system in a numerical study of strained flames with hypergolic chemistry.

Table 2.1 shows the important chemical reactions of the $(H_2+NO)/F_2$ system. The coefficients A, B, and E_A are fits to the reaction rates, with the forward reaction

#	Reaction	A	B	E_A
R1	$NO + F_2 \leftrightarrow NFO + F$	4.20×10^{11}	0.00	2285.0
R2	$NO + F + M \leftrightarrow NFO + M$	3.00×10^{16}	0.00	0.0
R3	$H + F_2 \leftrightarrow HF + F$	2.90×10^{9}	1.40	1325.0
R4	$F + H_2 \leftrightarrow HF + H$	2.70×10^{12}	0.50	634.0
R5	$F_2 + M \leftrightarrow F + F + M$	2.10×10^{13}	0.00	33700.0
R6	$HF + M \leftrightarrow H + F + M$	1.10×10^{19}	−1.00	134100.0
R7	$H_2 + M \leftrightarrow H + H + M$	8.10×10^{16}	0.00	103240.0
R8	$H + NO + M \leftrightarrow HNO + M$	5.40×10^{15}	0.00	−302.0
R9	$H + HNO \leftrightarrow NO + H_2$	4.80×10^{12}	0.00	0.0

Table 2.1: The $(H_2+NO)/F_2$ chemical system with rate coefficents. E_A is in cal/mole.

rate, k_f given by

$$k_\mathrm{f} = A T^B \exp(-E_A/R_0 T), \tag{2.1}$$

where R_0 is the universal gas constant. The reverse reaction rate is given by

$$k_\mathrm{r} = \frac{k_\mathrm{f}}{K_\mathrm{c}}, \tag{2.2}$$

where K_c is the equilibrium constant, computed by the CHEMKIN-II code (Kee *et al.* 1989) from the pressure, enthalpies, and entropies. These chemical reactions, as used in Egolfopoulos *et al.* (1996), are similar to the set employed in Dimotakis & Hall (1987). The rates for Reactions R6 and R7, however, are from Kontratiev (1972).

For a basic understanding of the chemical mechanism, Reactions R1, R3 and R4 are the most important. Reactions R3 and R4 are the chain-continuing reactions, where, once an H or F radical is produced, H_2 and F_2 are continuously converted into HF. At room temperature, obtaining sufficient H or F radicals is difficult. Nitric oxide (NO), however, reacts hypergolically with F_2 producing NOF and F. Thus, Reaction R1 produces the F radicals required to initiate the R3+R4 chain. R1 allows the entire system to become hypergolic, ensuring ignition on mixing of the reactants. The NO concentration becomes rate-determining by controlling the release of F radicals by reaction R1.

Reactions R8 and R9 were not considered in the earlier (Mungal & Frieler 1988) efforts. These "HNO" reactions are important in H_2-rich cases, where an increasing NO concentration will eventually have a much weaker effect on the chemical-kinetic rate than in a corresponding F_2-rich case (Frieler 1992). Essentially, in the presence of abundant H (as occurs in H_2-rich cases), some NO is removed by the HNO reactions before it can generate F radicals, and thus has a decreased effect on the overall chemical-reaction rate.

The changes in Reactions R6 and R7 from Dimotakis & Hall (1987) were necessitated by a change of the computational environment, which revealed limitations and numerical simulation difficulties of the previous rate expressions. The calculations were transferred to the DEC G-floating representation ($10^{-308} < |\mathrm{number}| < 10^{308}$)

from the standard DEC floating-point representation ($10^{-38} < |\text{number}| < 10^{38}$). After re-hosting the programs, calculations were performed that did not match previous results.

The differences were traced to the cutoff of the HF and H_2 dissociation reactions (R6+R7) below certain temperatures. This would occur when the dissociation rates would drop below the smallest representable number ($\approx 10^{-38}$). The reverse (recombination) rates would then be set to zero (using Eq. 2.2), even though, since both of the reactions have extremely small equilibrium constants, the actual reverse rate would not be negligible. The previous forward rate (for the H+F dissociation) was too high (10^{-60}) at room temperature, resulting in a reverse (recombination) reaction rate of 10^{38} (20 orders of magnitude above the actual room-temperature reaction rate of $\approx 10^{18}$). To fix this problem, rate expressions from Kontratiev (1972) were used. The current rate expressions for these reactions (R6+R7) produce room-temperature rates within one order of magnitude of observed values.

This problem does not appear in the calculations of Dimotakis & Hall (1987), because the original DEC floating-point representation zeroed out the rates for the reactions at about 505 K (R6) and 565 K (R7). Examination of the mechanism with the new reaction rates revealed that those reactions were not important at low temperatures (as might be expected from the high activation energies). Furthermore, calculations performed with the new mechanism matched the old results, indicating that the arbitrary machine-caused cutoff had in fact protected those calculations from the incorrect low-temperature behavior of the previous reaction-rate fits.

2.2 Product formation, fast chemistry, and molecular mixing

As the aim of this work is to investigate molecular mixing, a connection must be made between product formation and molecular mixing in the shear layer. As mentioned in the Introduction, chemical product measures are useful because they distinguish

between molecularly mixed and unmixed fluid. The relation between composition and product can only be made if the chemical kinetics are faster than the processes that change the fluid composition. Such a flow/chemical system combination is known as mixing limited, and is characterized by high Damköhler numbers. The Damköhler number, *Da*, is a ratio of the flow time scale to the chemical time scale, and at high-Damköhler numbers, the flow (and not the chemistry) dominates the overall rate of reaction.

In a mixing-limited case, the mapping of the fluid composition to the (local) product fraction is direct and unique. For a flow with a stoichiometric ratio, ϕ, the product response, $f_{\mathrm{p}}(\xi)$ is given by

$$f_{\mathrm{p}}(\xi) = \min\left(\frac{1-\xi}{1-\xi_\phi}, \frac{\xi-1}{\xi_\phi - 1}\right), \tag{2.3}$$

where ξ is the mole fraction of high-speed fluid, and the stoichiometric high-speed fluid mole fraction, ξ_ϕ, is given by

$$\xi_\phi = \frac{\phi}{\phi+1}. \tag{2.4}$$

A mixed-fluid estimate can be constructed by a pair of experiments with $\phi_1 = 1/\phi_2$. The mixed-fluid estimate, $f_m(\xi)$, can be constructed as a weighted sum of the product responses, $f_{\mathrm{p},1}$ and $f_{\mathrm{p},2}$, of the respective experiments:

$$f_{\mathrm{m}} = (1-\xi_0)\left(f_{\mathrm{p},1} + f_{\mathrm{p},2}\right), \tag{2.5}$$

where $\xi_0 = \min(\xi_{\phi_1}, \xi_{\phi_2})$, see Dimotakis (1991). This estimate of the mixed fluid is correct to the extent that the flow in the pair of experiments is the same. Figure 2.1 shows the response of a "flip" experiment pair, as well as the (upward-shifted) mixed fluid response. As can be seen in the plot, all mixed fluid between $\xi_{\phi,1}$ and $\xi_{\phi,2}$ is measured, while the method has reduced sensitivity at compositions near the pure freestream fluids.

In this work, the average product response profile is the normalized average tem-

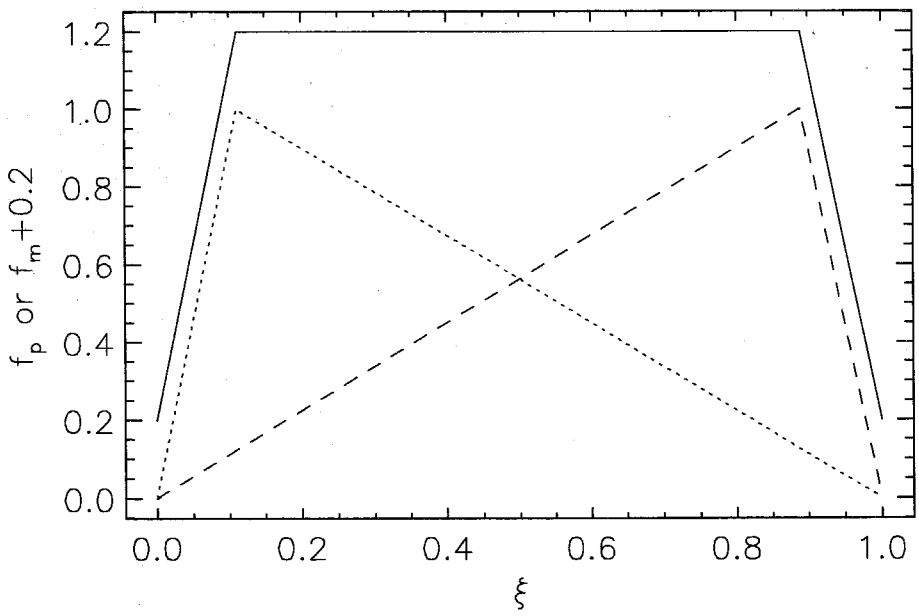

Figure 2.1: Response of an ideal irreversible-chemical-reaction "flip" experiment. Dashed and dotted lines are the product response for $\phi = 1/8$ and $\phi = 8$, from which the "flip" experiment response (solid line, shifted upwards by 0.2) is constructed.

perature rise, $\Theta(y) \equiv \Delta T(y)/\Delta T_{\rm f}$, where $\Delta T(y)$ is the measured average temperature rise profile and $\Delta T_{\rm f}$ is the adiabatic flame-temperature rise. The average response can be related to the fluid composition PDF, $p(\xi)$, by

$$\Theta(y) = \frac{\Delta T(y)}{\Delta T_{\rm f}} = \int_0^1 f_{\rm p}(\xi)\, p(\xi, y)\, d\xi. \tag{2.6}$$

2.3 Modeling the chemical kinetics

Since the accuracy of the product-based mixing measurements depends upon having mixing-limited (high Damköhler number, Da) chemistry, the experiments must be performed in this limit. To meet this requirement, the chemical kinetic rates, as modeled by the coefficients in Table 2.1, are used to model the kinetics of the flow, so the reactant concentrations needed for fast chemistry can be estimated. This

requires the use of some form of model for the chemical environment in the shear layer. Independent validation of fast chemistry is later performed by direct experiment.

The simplest model is a fixed-mass, perfectly-stirred reactor. This can reflect the dominance of the preferred composition as seen by Konrad (1976). This model was used in the study of Mungal & Frieler (1988). Although this is an appropriate first step, the well-stirred part of the turbulent shear layer is constantly entraining additional freestream fluids (new reactants) as it grows.

A first-order model for the well-mixed fluid, including entrainment, was presented by Dimotakis & Hall (1987). This model, dubbed the "balloon" reactor, consists of a well-stirred, constant-pressure reactor, into which reactants are continuously added in a ratio dictated by the entrainment ratio (and thus maintains the mixed-fluid composition at the indicated value). An additional model parameter introduced by this method is the quantity of well-mixed fluid in the reactor at the start of the calculation.

More complicated models can be made, including using the ideas behind the BBM model to create estimates of chemical kinetics (Broadwell & Mungal 1991, Miller *et al.* 1989). The discussion of such models is beyond the scope of this work.

2.3.1 Application to experiment design

To estimate the minimum H_2, F_2 and NO concentrations needed for fast chemistry, a numerical investigation of the conditions was made. The investigation used the CHEMKIN-II (Kee *et al.* 1989) chemical-kinetics code to calculate the reaction rates, and the "balloon" reactor model of Dimotakis & Hall (1987) to describe the environment.

The "balloon" reactor was used for several reasons. First, the applicability of the more complicated models to compressible turbulence, is not clear. Second, Hall (1991) made a comparisons between the Dimotakis & Hall (1987) model and both compressible and incompressible experiments, including the kinetics study of Mungal & Frieler (1988). Finally, the use of the model in this work was to help design

chemically-reacting experiments. Separate experiments were performed to confirm that they were in the fast-chemistry regime.

The "balloon" reactor was intended to provide a first-order model of reacting flow in the turbulent shear layer. In the fully-developed turbulent mixing layer, the mixed fluid is characterized by a dominant mixed-fluid composition in the cores of the large-scale structures. The composition of this fluid is controlled by the large-scale entrainment, and has a preferred value,

$$\xi = \xi_E = \frac{E_n}{E_n + 1}, \tag{2.7}$$

where E_n is the number (molar) entrainment ratio. The "balloon" reactor models this behavior by using a constant-pressure, perfectly-stirred reactor, with a constant inflow of the two free streams, at a ratio required to create the dominant composition. The mixture fraction, $\xi = \xi_E$, used in the model is calculated using the Dimotakis (1986) large-scale entrainment model.

The inferred chemical-reaction completion time, $t_{\rm ch}$, is the intercept of the maximum slope on the ΔT *vs.* $\log(t)$ plot with the temperature at reaction completion, $\Delta T_{\rm final}$ (Hall 1991). Figure 2.2 shows a representative temperature-rise plot with the maximum slope extended to mark $t_{\rm ch}$.

This model simulates the behavior of the mixed fluid in the large-scale structures as they convect downstream. The corresponding fluid-mechanical time scale is the large-scale structure time of flight. This is given by

$$t_{\rm f} = \frac{x}{U_{\rm c}}, \tag{2.8}$$

where x is the downstream measurement location (the distance from the trailing edge of the splitter plate to the thermocouple measurement station), and $U_{\rm c}$ the large-scale convection velocity. A Damköhler number can be defined in terms of the time of flight

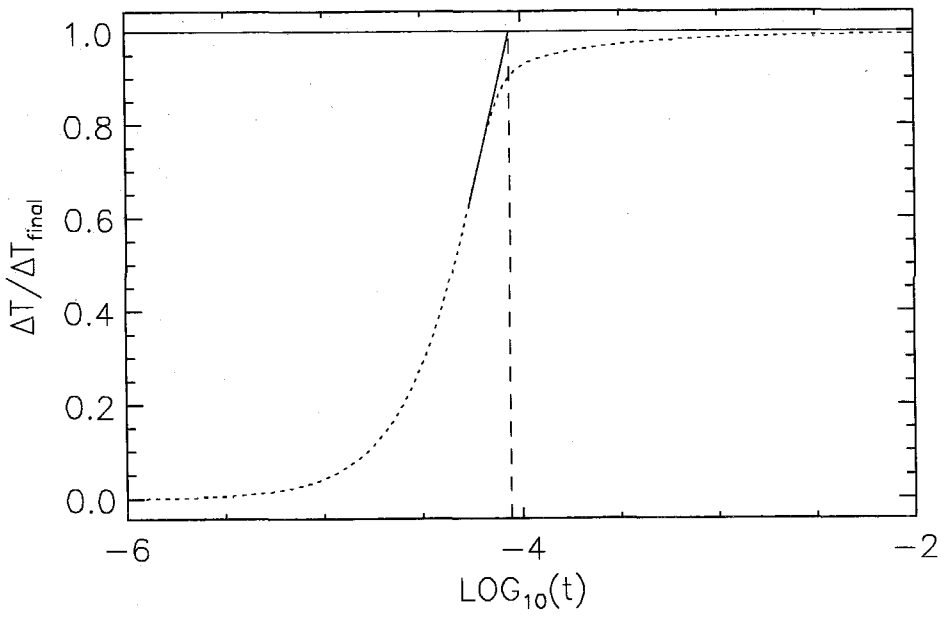

Figure 2.2: Example of chemical-kinetics timescale determination; dotted line is the normalized temperature response *vs.* $\log(t)$, solid line is the extrapolated maximum slope, and the dashed line indicates $t_{\rm ch}$.

and the reaction completion time, *i.e.*,

$$Da = \frac{t_{\rm f}}{t_{\rm ch}}. \tag{2.9}$$

The convection velocity is determined by selecting a frame in which the total pressure of the two freestreams are equal. The lab-frame velocity of that frame is the large-scale-structure convection velocity, $U_{\rm c}$. For the determination of the time of flight, $t_{\rm f}$, $U_{\rm c}$ was calculated from the isentropic pressure-matching relation (Bogdanoff 1983),

$$\left[1+\frac{\gamma_1-1}{2}\left(\frac{U_1-U_c}{a_1}\right)^2\right]^{\frac{\gamma_1}{\gamma_1-1}} = \left[1+\frac{\gamma_2-1}{2}\left(\frac{U_c-U_2}{a_2}\right)^2\right]^{\frac{\gamma_2}{\gamma_2-1}}, \tag{2.10}$$

where U_1 and U_2 are the freestream velocities, a_1 and a_2 are the freestream speeds of sound, and γ_1 and γ_2 are the freestream ratios of specific heats.

Using the reaction mechanism including the HNO reactions, Hall (1991) calculated a value of $Da \approx 5$ for the experimentally-confirmed, fast-chemistry experiment of Mungal & Frieler (1988). This value was used to design these experiments, and later checked by experiment.

2.3.2 The "balloon" reactor and mixing

A possible objection to the use of the Damköhler number as defined above is that the mixing time is much shorter than the time of flight, t_f. While this is true, it is also noted that, this Da effectively measures whether the cores contain reacted fluid, which in the gas-phase will be hot and contain highly-reactive radicals, such as H and F. This model simulates the environment of the well-mixed cores of the shear-layer structures and not the mixing of (unreacted) freestream fluid. However, this model has worked well in estimating the concentrations needed to reach the fast-kinetic regime. The presence of fast chemistry is also independently confirmed by experiment

While mixing times are much shorter than the time of flight, the actual chemical time scales are also much smaller than the time scale calculated by the "balloon" reactor. Much of the mixing will be between previously mixed (and possibly reacted) fluid and one of the two freestreams. In this environment, the chemical time scales will be much shortened by the presence of higher temperatures and highly reactive species (such as H and F) if the previously mixed fluid has already reacted.

The predictive utility of the "balloon" reactor is probably due to the nature of the problem. The "balloon" reactor will indicate if the core has reacted, and such reactions will produce the faster chemical-kinetic rates that outstrip mixing rates. In the absence of reacted fluid in the cores, the chemical-kinetic rates will be insufficient to match the mixing rate.

While the above explanation does not rise to the level of a proof, the model predictions were only used as experiment-design aids. That the measurements were taken in the fast-kinetic regime (high Da limit) was independently confirmed by experiment,

as will be discussed later.

Chapter 3 Experiment design

The objective of this work was to investigate molecular mixing in incompressible flows in the range of Reynolds numbers between the Reynolds numbers of previous incompressible- and compressible-flow experiments. As discussed in the Introduction, Reynolds number is a relatively weak parameter, which can have important effects due to its possible range of many orders of magnitude. As the intention of this work was to extend previous (incompressible-flow) work to higher Reynolds numbers (to span the one-decade difference between the compressible- and incompressible-flow Reynolds numbers), care was taken to minimize changes in the flow unrelated to changes in Reynolds number.

3.1 Issues in shear-layer flow

The shear layer obtained in experimental facilities can differ in many respects from an idealized shear layer for which self-similar, fully-developed flow may be assumed. The initial conditions may have an effect on the structure and/or development of the flow. The acoustic environment may result in additional forcing. Finally, the exit conditions may feed acoustic energy back into the flow.

The initial conditions for the flow are dominated by the wake of the splitter plate. This wake has three components: the high-speed stream boundary layer, the low-speed stream boundary layer, and the separated flow from the blunt end of the splitter plate. Although all these components may be important is some situations, most studies have concentrated of the effect of the high-speed boundary layer.

Specifically, Bradshaw (1966) suggested that the shear layer would achieve a self-similar state a minimum of 1000 high-speed stream boundary layer momentum thicknesses downstream of the splitter plate trailing edge. Dimotakis & Brown (1976) note that this corresponds to between three and four pairings. Karasso & Mungal

(1996) used a "pairing parameter" with which they estimated the minimum distance downstream that provided fully-developed flow. They estimated that the "pairing parameter" needed for fully-developed flow corresponds to roughly three pairings.

Despite this estimate of downstream distance for which fully-developed flow may exist, the state of the boundary layer can have an influence which persists beyond this length. Specifically, the tripping of an initially laminar boundary layer can significantly alter the shear-layer growth rate, as reviewed in Dimotakis (1991). Additionally, the reacting-flow results of Mungal *et al.* (1985), where for two of the Reynolds numbers, both tripped and untripped boundary layers are investigated, show significant evidence of the effects of initial conditions both on the spreading (growth) of the layer and on the distribution of chemical product.

The current work raised a number of questions about the state of the splitter-plate boundary layer in the lower-velocity case. As a result, a subsequent investigation (Slessor *et al.* 1998) considered the effects of initial conditions (specifically, boundary-layer tripping). For the lower-Reynolds number case of the current conditions, tripping the boundary layer significantly changed the distribution of the mixed fluid. Slessor *et al.* (1998) also provides a more complete overview of initial-condition effects in the shear layer.

Forcing the shear layer can also significantly affect the composition of the mixed fluid in the layer (Koochesfahani & MacKinnon 1991). In the absence of intentional forcing, acoustic resonances of the apparatus can result in unintentional forcing. For example, Frieler (1992) reported that some of his lowest Reynolds number cases may have been affected by acoustic resonances. These resonances can occur in the test section, in the freestream supplies, or in the outflow region. Typically, frequencies of the acoustic resonances are set by the speeds of sound and facility dimensions.

Feedback from the flow exiting the test region is also of concern. Acoustic energy may be applied to the flow if the shear layer has a resonant interaction with the facility past the exit of the test area. Additionally, as Dimotakis & Brown (1976) noted, the influence of all structures (even those close to the exit of the test area) can be felt near the splitter-plate trailing edge in elliptical flow. Such influences were visualized

by Hall (1991), who observed upstream-travelling waves in the subsonic stream of a bi-sonic (supersonic/subsonic) shear-layer flow, showing that feedback from the exit of the flow was felt upstream to the near-splitter plate region.

Heat release in the subsonic, incompressible shear layer is known to slightly reduce the growth rate of the shear layer and to have a more complex effect on product formation (Hermanson & Dimotakis 1989). It also changes the speed of sound in the mixed fluid, changing the acoustic environment, thus changing any "natural" forcing present.

3.2 Features of the supersonic shear-layer facility

Experimental design must consider facility limitations. These include the maximum and minimum mass fluxes, restrictions on freestream compositions, and the geometry of the facility.

The lower stream mass flux (and thus the velocity) is limited by two factors: the limited volume of the lower-stream reactant tank limits run duration and the metering valves limit the maximum velocity. The limited volume ($0.57\,\mathrm{m}^3$) of the lower-stream reactant tank limits the run length for almost all experiments performed in this facility. For safety purposes, it is preferred to exhaust the contents of the lower-stream reactant-tank bladder bag in the course of an experiment. The minimum run-length is governed by the needed (steady-state) flow time and the length of the start-up transient.

The flow-control for the lower stream is passive, while the upper stream is controlled with a computer-commanded metering valve. See Appendix A for more details. This results in fixed start-up times for the lower stream. For the upper stream, however, the start-up time can be changed by changing the program in the control computer. Although the upper-stream control is designed to utilize feedback from the plenum pressure, this requires a minimum resolution in the pressure measurements and a reasonable constraint on the test-region pressure, since the Mach number of the flow depends on the ratio of absolute pressures. For low Mach numbers, this may not

be possible, and flow control must then be performed in the command mode, where the supply pressure (upstream of metering valve) is monitored and the metering valve moved (during the run) to maintain a constant mass flow rate.

The upper-stream supply is designed for H_2 and NO as reactants carried in a diluent mixture of N_2, Ar, and He, and cannot be used with mixtures containing F_2. All of the reacting experiments performed in this facility use H_2+NO as reactants in the upper stream, and F_2 as the reactant in the lower stream.

A significant concern with the H_2+NO/F_2 chemical system is the difference between the H_2+NO and F_2 reactants. H_2 has a higher diffusivity than F_2 and NO. A significant concern is that the H_2 can diffuse through the reactant zones before the NO has released F radicals to initiate the reaction chain (Frieler 1992). Since the H_2+NO reactants are always carried in the upper stream, restricting the cases studied to upper-stream fast, as was necessary for the subsequent extension of the current cases with the higher-Reynolds-number Slessor (1998) case to be discussed later, would result in an association of upper-stream reactant rich case with H_2-rich cases. If the behavior of the reactions are significantly influenced by the differential diffusion of H_2, this could then result in a false inference on mixing.

An additional concern is the slower nature of H_2-rich reactions. This was noted in Frieler (1992), where H_2-rich kinetics were shown to have a complicated dependence on NO concentration. Although in F_2-rich cases chemical-kinetic time-scales continuously decreased with increasing NO concentration, H_2-rich cases reached a region where increasing NO concentration barely reduced the chemical-kinetic time-scale. Additionally, as discussed in Section 2.1, H_2-rich cases require higher concentrations than F_2-rich cases and thus release more heat.

The splitter-plate wake is controlled by the splitter-plate and nozzle geometries, the two freestream velocities, and freestream turbulence levels. Specifically, the splitter plate, on which the wake-forming boundary layers grow, is fixed. The upper-stream side of the splitter-plate is flat, with the flow exiting parallel to the start of the guidewalls. The lower-stream surface of the splitter plate has a curved surface with convex curvature upstream of the trailing edge. The lower-stream enters at a

5° angle to the upper-stream and guidewalls. Finally, the splitter-plate tip has an included angle of 5° and a trailing edge height of 0.127 mm (0.005 in). The included angle of the splitter plate serves two purposes: it provides for the entrainment needed by the shear layer and provides structural strength. The geometry of the trailing-edge region is shown in Figure 3.1.

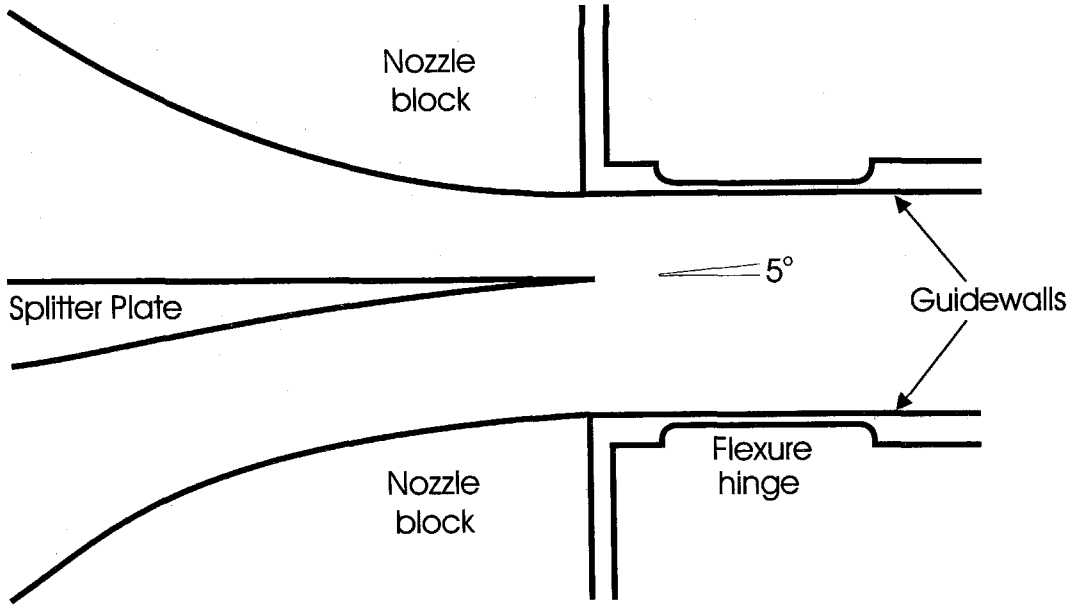

Figure 3.1: The geometry of the near-splitter plate region. Note the 5° angle between the lowere stream and the upper stream. Guidewalls start parallel to the upper-stream.

The 5° angle of the lower-stream to the guidewalls results in curvature in the near-field of the lower-stream fast cases. This may change the near-field instabilities from which the shear layer flow evolves.

Mean-temperature-rise profiles were measured at a single downstream station, at $x = 36.5\,\text{cm}$ (14.38 in) downstream from the splitter-plate trailing edge. The mean-temperature-rise profile measurements were made using thermocouple probes mounted on a fixed rake, inserted slightly upstream of the guidewall ends. With the current guidewalls, this limits the rake position to the single downstream position.

For acoustic resonances in the test cell (the region between the splitter-plate trailing edge and the downstream measurement location), frequencies are set mostly by the

speeds of sound and the dimensions, and only weakly by the flow velocity. Since shear-layer structure frequencies increase with flow velocity, higher velocity flows should be less affected than lower-speed flow if the acoustic frequencies are below the flow frequencies. For the current conditions, the test-cell quarter-wave frequency (based on length from the splitter plate to the measurement rake) is 250 Hz, while the exit structure-passing frequencies for the two cases selected (discussed below) are given by 640 Hz and 1050 Hz for the lower- and higher-Reynolds number cases.

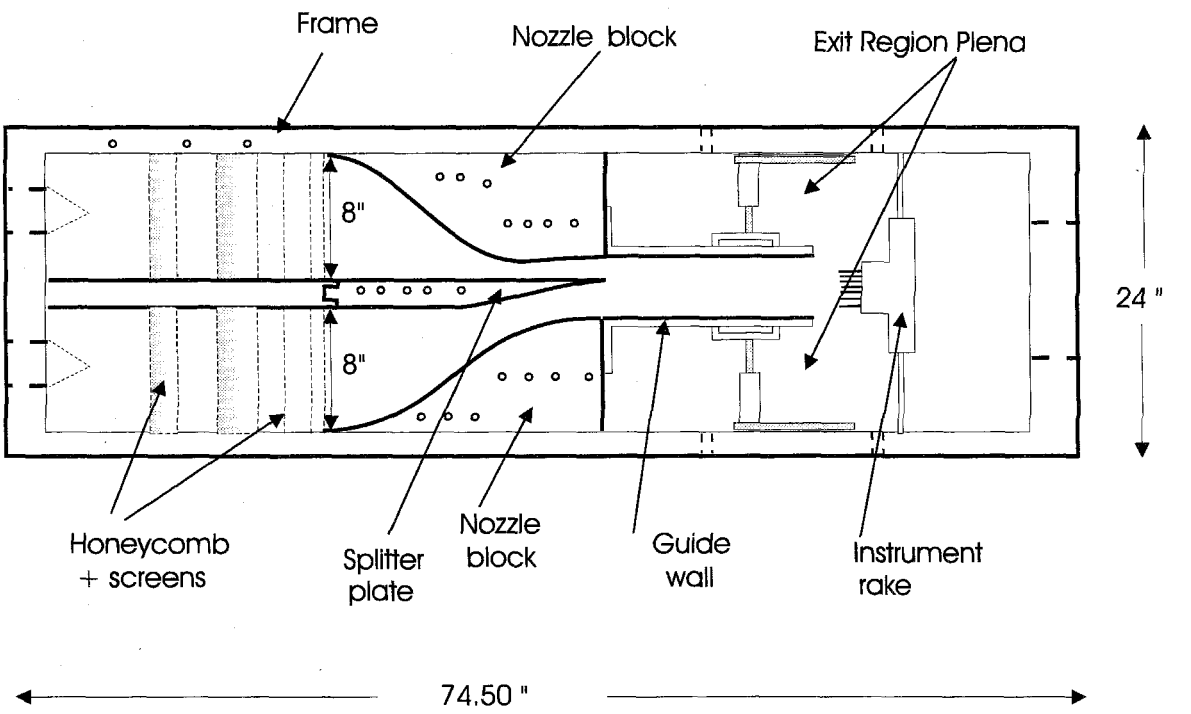

Figure 3.2: Test section without guidewall extensions, showing the plena regions above/below and beyond the guidewalls.

Figure 3.2 shows the test section, including the test cell. The facility guidewalls end well short (about 35 cm) of the test section exit. This creates two plena above and below the guidewalls. The plena are in contact with the exiting flow and may become involved in resonant interactions with the shear layer. As discussed in Appendix A, guidewall extensions (see Figure 3.3) were employed to separate the plena from the exiting flow. These guidewall extensions also effectively increase the test cell length for acoustic resonances, further separating the flow and acoustic frequencies.

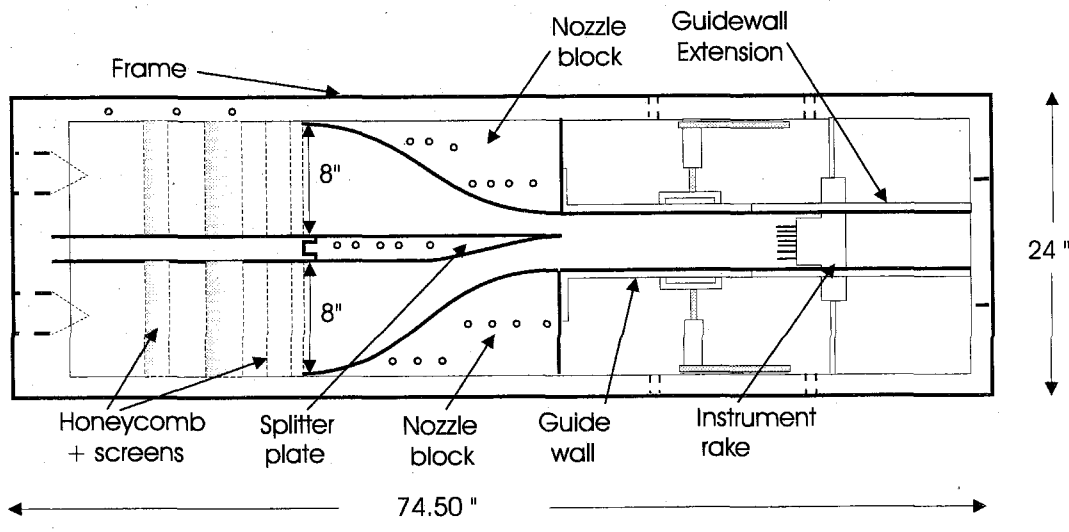

Figure 3.3: Test section, showing facility configuration with guidewall extensions.

3.3 Subsonic, incompressible-flow experiments

These experiments are meant to address the gap between Reynolds numbers in previous subsonic-flow investigations ($10^4 < Re < 10^5$) and Reynolds numbers in the compressible-flow experiments ($10^6 < Re < 10^7$). The upper Reynolds-number limit of the previous subsonic-flow investigations (Mungal *et al.* 1985, and Frieler 1992) was limited by the flow capacity of the previous subsonic-flow shear-layer facility. The current supersonic/subsonic shear-layer facility, however, is capable of much higher flow rates. Additionally, although the lower-stream supply was inherited directly from the previous, subsonic-flow facility, the freestream cross-sectional area is smaller, and thus higher velocities are possible.

The flow does not change significantly as reactant concentrations are changed for the flip experiments. If these flows were to use a N_2 diluent, swapping of H_2 and F_2 for the diluent would change the density significantly, with possible changes in mixing attributable to changes in the flow. The experiments were designed to have the same base (diluent) gas mixture in both freestreams. The mixture is N_2, with the mole fraction of He equal to the maximum mole fraction of H_2 and the mole fraction of Ar equal to the maximum mole fraction of F_2. This mixture allowed the substitution of

reactants for diluent gases with negligible changes in density.

A pair of nominal flow conditions were selected: 165 m/s over 65 m/s and 100 m/s over 40 m/s. The lower-velocity case was selected to be close to the highest Reynolds number cases of Mungal *et al.* (1985) and Frieler (1992). The higher velocity pair was selected so the high-speed side velocity was close to the mass-flux/run-time limitation imposed by the lower-stream supply. This choice allowed experiments with both the upper stream and the lower stream as the high speed stream. To achieve higher velocities (and Reynolds numbers) the subsequent work by M. Slessor in collaboration with the author (Slessor 1998) abandoned the ability to have the lower stream as the high-speed stream.

The low Mach numbers and associated pressure ratios of these flows did not allow active control of the upper stream. Furthermore, the upper-stream start-up time (with the original control algorithm) was close to the total length of the run for the lower-stream highest-mass-flow case. A modified control algorithm, which overshot the valve position during start-up, was introduced. This overshoot allowed more mass-flux during the start-up, charging the plenum and the supply pipe between the plenum and the metering valve. With the overshoot, start-up time in these experiments was 0.6 s to 0.8 s, providing sufficient time for data acquisition.

In designing the reacting experiments, the first decision to be made was what stoichiometric ratios (ϕ's) should be used in the flip experiments. For best comparison with previous gas-phase, incompressible work, the choice was made to use $\phi_1 = 1/\phi_2 = 1/8$. This allows direct comparison with results from Mungal & Dimotakis (1984), Mungal *et al.* (1985), and Frieler (1992).

With that decision, the remaining choice was the concentrations of the reactants. For F_2-rich cases, the kinetics are very fast and a 8% F_2/0.97% H_2/0.06% NO case was well beyond what was required to attain the fast-chemistry limit. A lower concentration (of F_2) was not used, as the 8%/1% mixture has nearly the same adiabatic flame-temperature rise as the mixtures used in the previous studies. For the H_2-rich cases, a 2.06% F_2/16% H_2/1% NO case would give a $Da \approx 9$ (above the $Da \approx 5$ limit suggested by Hall 1991) with $U_1 = 165$ m/s. This was selected as the H_2-rich case.

	USS					LSS				
	X_{N_2}	X_{He}	X_{Ar}	X_{H_2}	X_{NO}	X_{N_2}	X_{He}	X_{Ar}	X_{F_2}	ΔT_f
cold run	0.76	0.16	0.08	—	—	0.76	0.16	0.08	—	—
H_2-rich	0.75	—	0.08	0.16	0.01	0.76	0.16	0.059	0.021	354.6
F_2-rich	0.76	0.15	0.08	0.0097	0.0006	0.76	0.16	—	0.08	171.3

Table 3.1: Design chemistry of the subsonic Reynolds number experiments

To address the issues raised by the association of specific reactants with each freestream, it was decided to also perform experiments with the same velocities, but with the lower-stream fast. These experiments involve pushing the lower stream to the upper limits on velocity and operating the upper stream at low stagnation pressures, where feedback control is not possible.

These experiments were designed to measure the effects of Reynolds number in low-freestream turbulence, with natural splitter-plate boundary layers, and no active measures were taken to modify the initial conditions for these experiments. Such an investigation was performed subsequently (Slessor *et al.* 1998) to, in part, answer questions raised by the current results. Indeed, at the lowest Reynolds number, tripping the boundary layer was shown to change the flow far downstream of the splitter plate.

Preparatory experiments suggested that acoustic feedback between the shear layer and the plena above and below the test region (see Figure 3.2) could force the flow. Guidewall extensions were then installed to isolate the test region from the plena, and the flow stability was substantially improved. The guidewall extensions were left parallel to the upper guidewall (not converged or diverged) for all conditions. The subsequent experiments (Slessor *et al.* 1998) that clearly demonstrated the initial conditions' effect on the flow used the guidewall extensions converged or diverged with the same angle as the guidewalls.

Table 3.1 summarizes the freestream compositions for these experiments (USS is upper-stream side, LSS is lower-stream side). Table 3.2 summarizes flow velocities, Mach numbers, and velocity and density ratios. The total convective Mach number,

U_1	M_1	U_2	M_2	r	s	M_c
165	0.45	65	0.15	0.39	0.96	0.14
100	0.27	40	0.11	0.40	0.99	0.09

Table 3.2: Design flow conditions of the subsonic Reynolds number experiments

M_c, is defined as (Papamoschou 1989):

$$M_c \equiv \frac{U_1 - U_2}{a_1 + a_2}, \tag{3.1}$$

and provides a measure of the compressibility for the shear-layer flow. It should be noted that the density ratio for the two cases are not unity, which is caused by the slight compressibility of the high-speed freestream flow.

Chapter 4 Subsonic, incompressible flow experiments

These experiments extended the local Reynolds-number range of incompressible-flow, chemically reacting measurements from a previous $Re_\delta = 1.5 \times 10^5$, to 3.5×10^5. Subsequent work by M. Slessor in collaboration with the author and others (Slessor 1998) further increased this upper local Reynolds number to $Re_\delta = 9 \times 10^5$. These investigations were meant to help resolve the ambiguity between compressibility and Reynolds-number effects, caused by the relatively large gap in local Reynolds number between the previous incompressible- and compressible-flow experiments, as discussed in the Introduction.

The measurements used the chemical-reaction method to infer mixing in the shear-layer. Such measurements of the mixed-fluid, as discussed in Chapter 2, require two temperature-rise-profile measurements (a "flip" experiment). Since the freestream flows are slightly compressible, resulting in static-temperature drops of up to 12 K, a non-reacting, temperature-reference run is also required. The accuracy of the "flip" experiment results depend on two conditions: the flow, and thus mixing, should not differ significantly between the two reacting experiments, and the chemical reactions must be kinetically-fast compared to the fluid-mixing times (high-Da).

Table 4.1 gives the nominal flow conditions and Reynolds numbers for the four flow cases. HSS stands for High-Speed Stream, and indicates which stream of the facility

Condition	HSS	U_1	U_2	Re_x	$Re_\delta\,(\delta/x = 0.15)$
1	upper	100	40	1.2×10^6	1.5×10^5
2	lower				
3	upper	165	65	2.1×10^6	3.2×10^5
4	lower				

Table 4.1: Table of Subsonic Flow conditions (HSS =High Speed Side)

is the higher-speed stream. The high-speed and low-speed freestream velocities are U_1 and U_2 respectively, x is the distance from the splitter plate to the rake, δ is the shear layer thickness and the Reynolds number, Re_L is defined as:

$$Re_L \equiv \frac{\rho\,(U_1 - U_2)\,L}{\mu}, \tag{4.1}$$

where L is the appropriate length scale: in this study either x, the downstream distance, or δ, the shear-layer thickness. For Table 4.1, the values for Re_δ were calculated using a nominal value of $\delta/x = 0.15$. The higher Re_δ quoted at the start of this chapter was due to changes in U_1 and U_2 from the nominal conditions. At each flow condition (1, 2, 3, and 4), there are three cases: one non-reacting reference case, denoted by 1c, 2c, *etc.*; one H_2-rich reacting case, denoted by 1h, 2h, *etc.*; and one F_2-rich reacting case, denoted by 1f, 2f, *etc.*

4.1 Experiments

Figure 4.1 is a schlieren image of a non-reacting experiment. The flow exhibits the large-scale, two-dimensional (high spanwise-coherence) structure typical of incompressible shear layers (Brown & Roshko 1974). To the right end of the photograph, the Pitot and thermocouple probes can be seen. The solid black edges at the top and bottom of the image are the guidewalls. The lower guidewall is converged, providing the entrainment requirements for the flow, which, with no heat release, has a negative displacement thickness (Hermanson & Dimotakis 1989). The upper guidewall was held fixed (parallel to the upper freestream) for these experiments. On the left edge of image, the curved border is due to vignetting by the edge of the imaging mirror, while at the top and bottom of the left side the border indents into the image with the shadows of the tabs holding the mirror. The features, above the mixed-fluid region in the center of the image, are damage to the sacrificial (inner) pyrex windows.

Cold run experiments, as the one shown in Figure 4.1, are used to derive temperature-rise data from the raw, average-temperature profiles obtained during the reacting

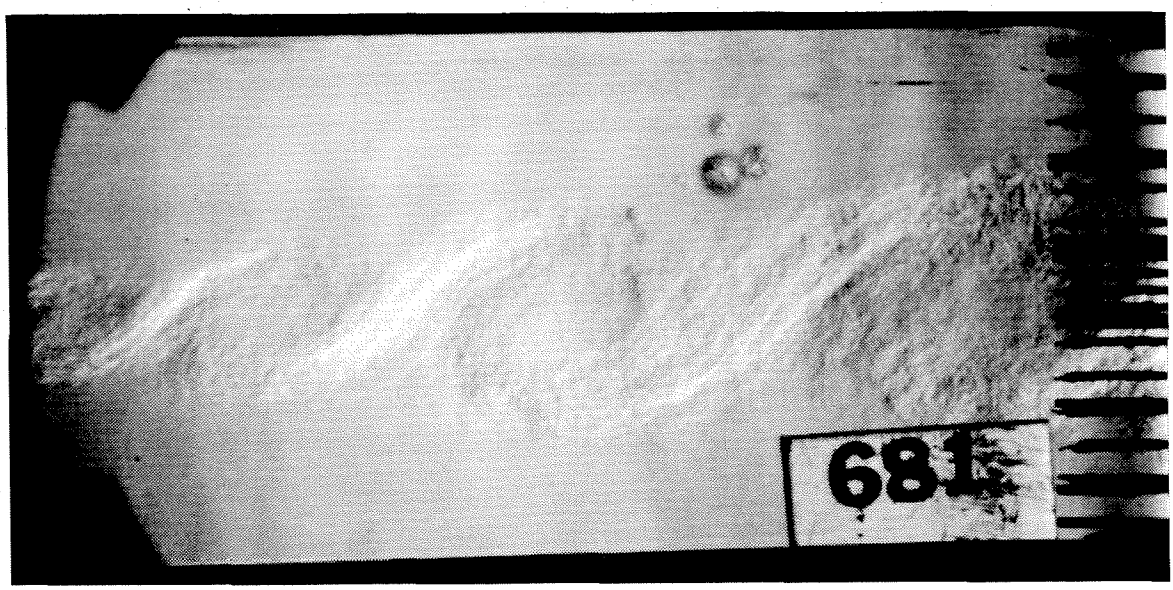

Figure 4.1: Schlieren image of Case 3c flow. Nominal velocities: upper-stream: 100 m/s, lower-stream: 40 m/s. Nitrogen in upper stream replaced by density matched mixture of C_2H_4, Ar and He for better flow visualization.

runs. Figure 4.2 shows a schlieren image of a Case 1f flow. This is a $\phi = 8$, F_2-rich reacting flow, corresponding to the non-reacting flow in Figure 4.1. Several differences are worth noting: the guidewalls are now diverged, since the heat release now results in a positive displacement thickness; flow structures are more visible, as would be expected with heat release, and are discernibly different from the non-reacting flow structures. Also, in the lower and upper right of the image, protrusions from the guidewall into the flow are visible. These are support tabs for the guidewall extensions, located next to the sidewalls (on the guidewall extensions, overlapping the guidewalls), which span only 6.4 mm (0.25 in) of a total 152 mm (6 in) width (into the page in the photographs).

For contrast, Figure 4.3 shows a schlieren image from a Case 4f reacting flow. In this image, the high-speed stream is on the bottom. The reversal of the sense of rotation of the flow in the structures is evident, with braid regions running from the upper left to the lower right.

From reacting experiments, the average temperature-rise profile measurements

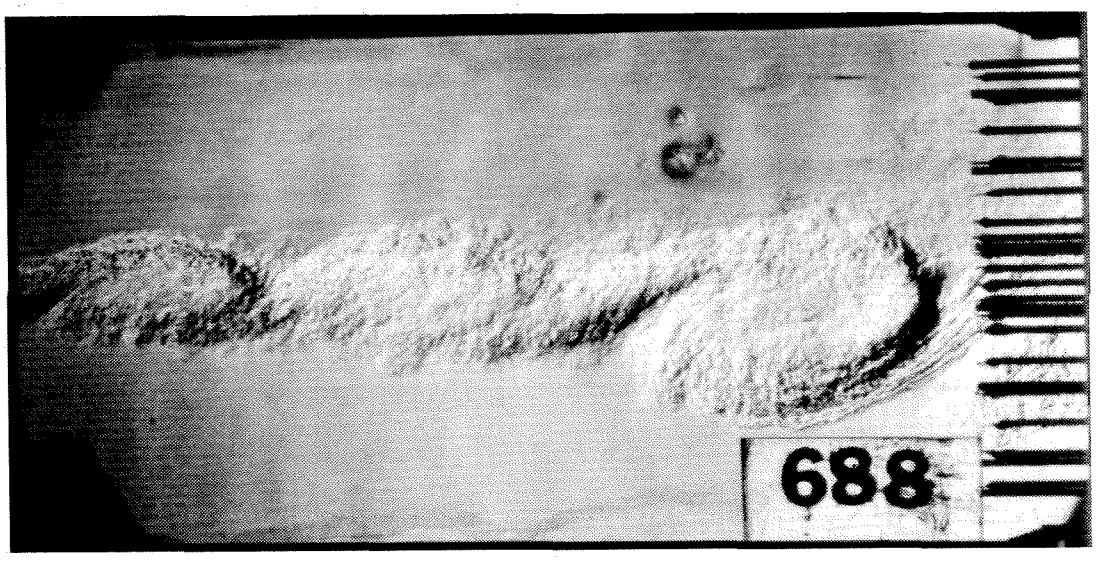

Figure 4.2: Schlieren image of reacting Case 1f flow. F_2-rich reacting flow corresponding to the Case 1c non-reacting flow.

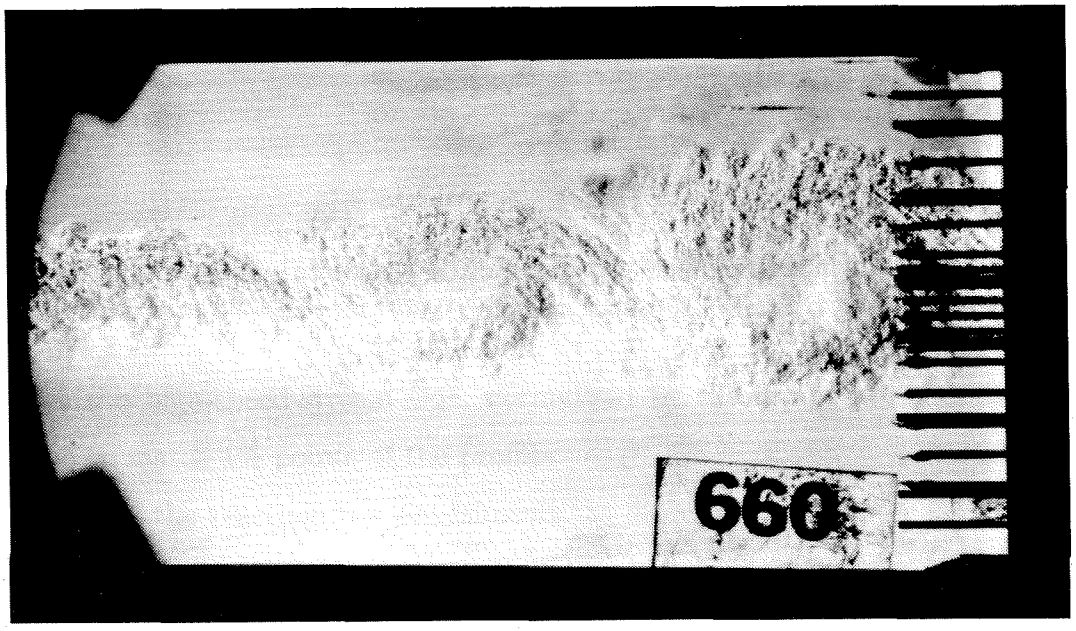

Figure 4.3: Schlieren image of Case 4f reacting flow. The high speed stream is at the bottom of the image.

were obtained and processed, as discussed in Appendix B. Three measures derive from these profiles: the 1% temperature thickness, δ_T (Equations B.3 and B.4); the product thickness, δ_p, which is the integral of the product response (Equation B.6); and the product fraction, δ_p/δ_T, which is the fraction of the fluid in the shear layer that has reacted. An example of the normalized average temperature-rise profiles is shown in Figure 4.4. Profiles are plotted with the transverse coordinate, y, which increases

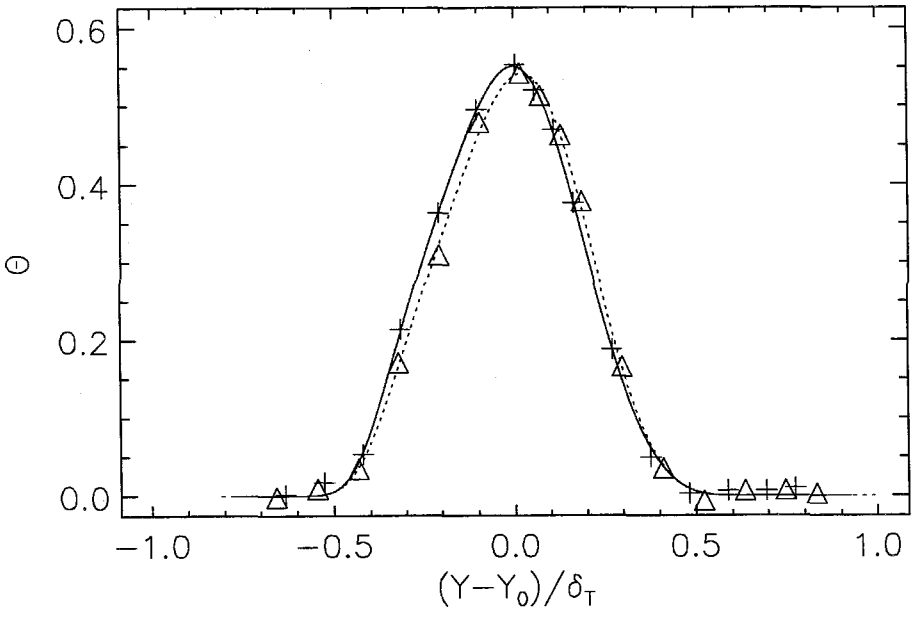

Figure 4.4: Average normalized-temperature-rise profiles for the Case 1f flows. Solid line/crosses: Run 688, dotted line/triangles: Run 691.

towards the high-speed-stream side, normalized by the temperature thickness and offset so to match 1% points of the profiles.

A pair of the reacting-flow experiments, as discussed in Chapter 2, can be used to infer mixing. This mixing was calculated as an average-mixed-fluid profile, $f_m(y)$ (Equation 2.5). The integral of this profile, δ_m/δ_T, can also be expressed as a normalized sum of the separate product thicknesses, δ_p (Equation B.7). An example of a "flip" experiment is shown in Figure 4.5.

The peaks of the normalized-temperature-rise profiles, $\Theta(y) = \Delta T/\Delta T_f$, of Figure

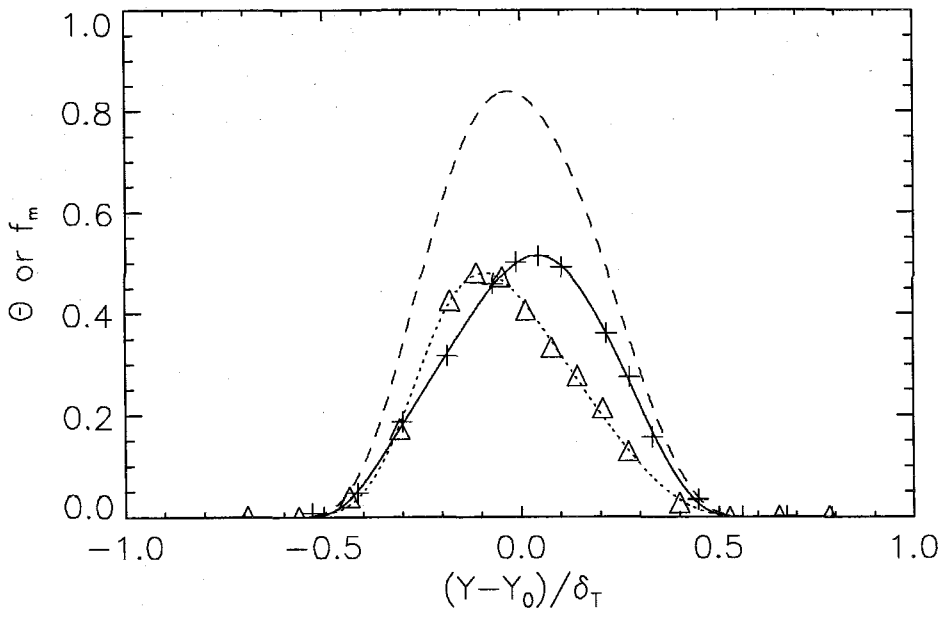

Figure 4.5: "Flip" experiment profiles from Case 3f and 3h flows. Solid line/crosses: Case 3f (Run 648), dotted lines/triangles: Case 3h (run 647), dashed line: calculated mixed fluid (see text).

4.5 are tilted towards the reactant-lean freestreams. This is similar to the results of Mungal & Dimotakis (1984), but differs from the high Sc-number results of Koochesfahani & Dimotakis (1985), where the peak of both profiles were close. However, not all of the flip experiments in the current investigation behave this way, as Figure 4.6 shows. The peaks of these profiles, while tilted towards the reactant-lean freestreams, are only slightly separated. Notably, the maximum mixed-fluid response is between 80 and 90% for all of the flip experiments.

This difference between the separated peak temperatures and the coincident peaks was also seen by Slessor *et al.* (1998) who studied flows at the same nominal conditions as the Case 1 flows. The experiments were performed with and without tripping the high-speed freestream splitter-plate boundary layer. The untripped flows had similar behavior to the Case 1 flows shown in Figure 4.6, while the tripped flows showed a separation to the peak temperature locations, as in the higher-Reynolds number Case

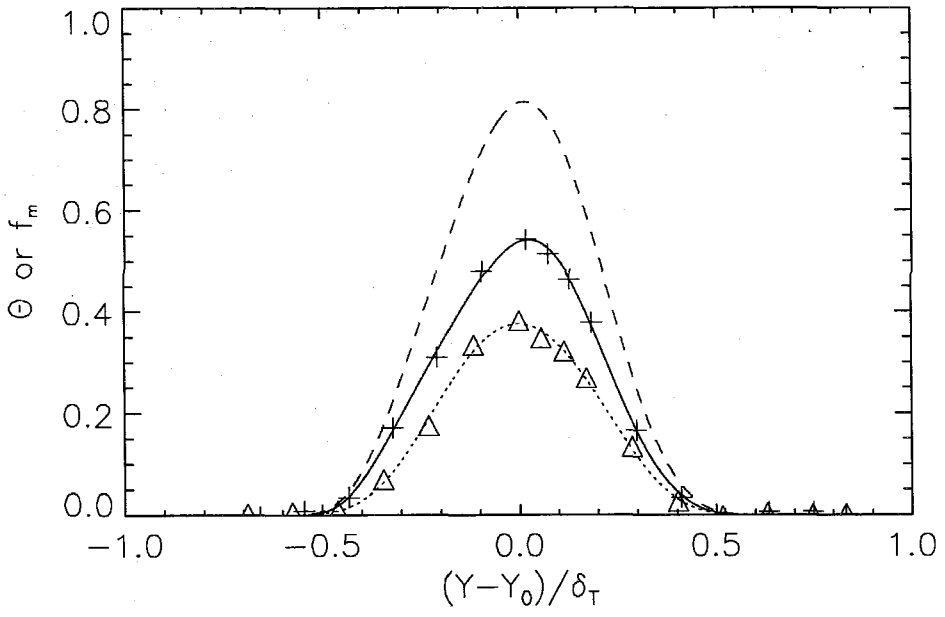

Figure 4.6: "Flip" experiment profiles from Cases 1f-1h. Solid lines/crosses: Case 1f (Run 691), dotted line/triangles: Case 1h (Run 693), dashed line: calculated mixed fluid (see text).

3 flows shown in Figure 4.5. This suggests that some of the differences in these flows are due to changes in the high-speed freestream splitter-plate boundary layer.

For mixed-fluid measurements to register mixing accurately, they must be chemical-kinetically fast. As discussed in Chapter 3, these experiments were designed so the minimum Da was 9. Hall (1991) established that, for the fast-chemistry experiment of Mungal & Frieler (1988), the fast chemistry limit was achieved with $Da = 5$, as determined by the "balloon" reactor. With a design $Da = 9$, the experiments were expected to be chemically fast. As an experimental vvalidation, a separate kinetics test was performed with slightly reduced NO and F_2 concentrations. The Da of the modified case was 7, roughly 25% lower than the $Da = 9$ case. Figure 4.7 shows the normalized-temperature-rise profiles, which match well.

Although this experiment suggests fast chemistry, the 25% variation in Da may be questioned as inadequate for a true kinetics test. Slessor (1998), in an extension

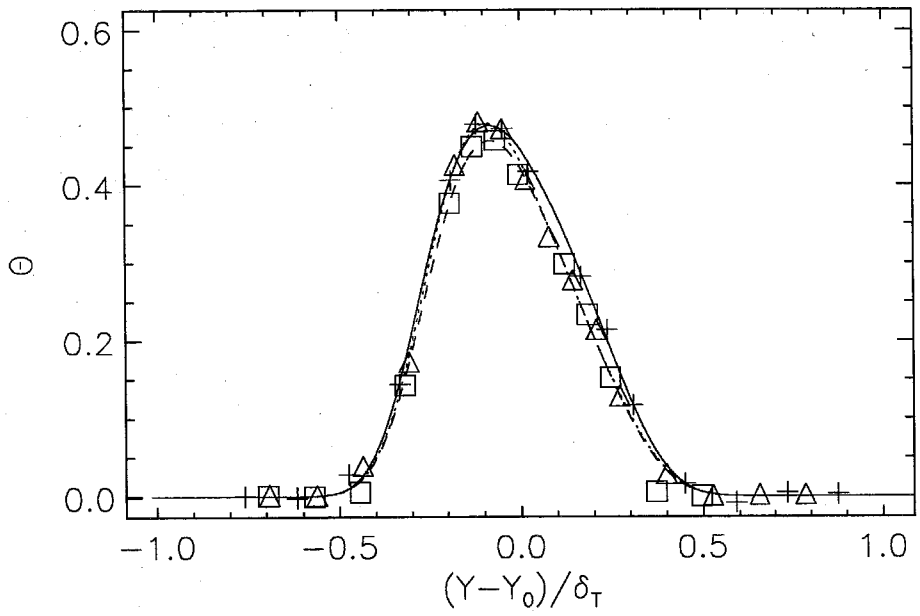

Figure 4.7: Kinetics experiment normalized-temperature-rise profiles. Solid line/ crosses and dotted line/triangles: $Da = 9$, dashed line/squares: $Da = 7$.

to the current work, performed experiments at the same nominal density and velocity ratios, but at a higher overall velocity ($U_1 = 280\,\mathrm{m/s}$, *vs.* $U_1 = 165$ m/s here). He performed a series of three experiments with varying reactant concentrations that provided a larger range of Da. Specifically, the three experiments, which had negligible change in product, had $Da = 3.2$, 2.2 and 1.4, as estimated by the methods used in this investigation. The lower Da and the factor of two range, in Da of the latter kinetics experiment, confirm that the current, higher-Da experiments are in the kinetically-fast regime. Regardless of the estimated Da, the Slessor (1998) kinetics experiments used lower reactant concentrations and higher velocities than the current effort. Since Slessor (1998) found fast chemistry with slower chemistry (lower reactant concentrations) and faster fluid mixing (higher velocities) in a similiar flow, the current experiments must be considered to be in the fast-kinetic regime.

The other concern in mixed-fluid measurements are changes in the flow. Since the current conditions were run with very low pressure heads, flow control was difficult,

and flow velocities sometimes varied. Despite this, most cases repeated well, with little variation in measured temperatures. However, Case 2h flows produced three different profiles in four runs. For this reason, Case 2h flows were deemed unstable and not used for estimates of mixed-fluid or mixed-fluid composition.

While the results of the two Case 4h flows agreed, the temperature profile was much wider. An examination of the schlieren images reveals the reason (Figure 4.8). The shear layer is flagellating, projecting high-temperature fluid over a greater trans-

Figure 4.8: Schlieren image of case 4h flow. Flagellation of the layer is clearly visible. The lower stream is the high-speed stream.

verse extent. As with Case 2h, these measurements were not relied upon to provide mixed-fluid or mixed-fluid composition estimates. Since both of these cases are lower-stream fast, some of this instability may be related to near-splitter-plate difficulties mentioned in Chapter 3. Specifically, the forced curvature of the near-field of the shear layer, as shown in Figure 4.9 may introduce changes in the flow, and thus mixing. The two F_2-rich cases, lower-stream fast cases were repeatable, and are included in the mixing and entrainment estimates, although the shapes of the profiles were different from the typical tilted bell-curve shape. See Appendix C for more details on all of the experimental runs.

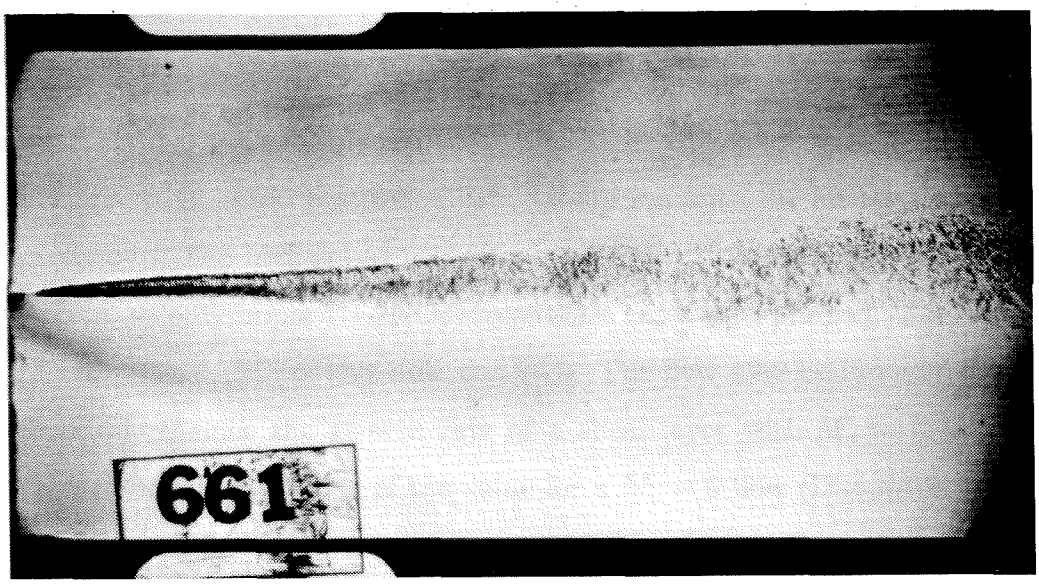

Figure 4.9: Schlieren image of the upstream portion of the Case 3f (Run 661) flow. Note the downward curvature of the layer near the splitter plate.

4.2 Results

The results will be presented and compared to those of previous chemical-reaction method studies. The results from the "cold-chemistry" method (Paul & Clemens 1993, Clemens & Paul 1995, Island 1997) are discussed later. Other data presented (in this section) will be from:

- Mungal & Dimotakis (1984): Although not performed as "flip" experiments, same results were obtained for both $\phi = 8$ and $1/8$. A slightly different measure of product fraction was used, that was easily converted to the current measure (Dimotakis 1991).

- Mungal *et al.* (1985): They performed a series of experiments investigating the effects of Reynolds number on chemical-product formation at $\phi = 1/8$. Again, the earlier measure of product fraction was converted to the current measure.

- Frieler (1992): The mixed-fluid results were normalized for dilatation effects, by a method which required temporal resolution. For presentation here, the average

temperature-rise data were reprocessed by the methods detailed in Appendix B used in the current study.

- Slessor (1998): A subsonic experiment at higher Reynolds number (an extension of the current work, performed in collaboration with the author and others) is presented. The high-speed velocities are beyond the capabilities of the lower-stream, so only upper (H_2/NO)-stream-fast cases were studied. The convective Mach number, M_c, of this flow was 0.25. The flow may be influenced by compressibility, since the growth rate of a shear-layer with $M_c = 0.25$ typically reaches only 0.80 to 0.85 of the value for a $M_c = 0$ flow (Dimotakis 1991). All inferences using this data must be tempered by the knowledge that results from this case may not show the effects of Reynolds number alone.

- Slessor *et al.* (1998): An investigation of the effects of initial conditions (boundary layer tripping) at the same nominal conditions as the lower Reynolds number case presented here. One of the differences between those experiments and the cases presented here was that the guidewall extensions were converged or diverged to the same degree as the guidewalls, unlike the current cases, where guidewall extensions were kept parallel to the upper guidewall.

The plots of product fraction, mixed-fluid fraction and mixed-fluid composition ratio will include model predictions. The models can be used to calculate the product fraction as the convolution of the PDF with response functions $f_p(\xi)$ (Eq. 2.3). The mixed fluid fraction and composition ratio can then be calculated from the product fractions using Equations B.7, B.8 and B.9. The models are only plotted for Reynolds numbers greater than 2×10^4, since the range $5 \times 10^3 < Re < 2 \times 10^4$ is transitional, and the models are intended for fully developed turbulence. The models plotted are:

- Broadwell-Breidenthal-Mungal (BBM) model (Broadwell & Breidenthal 1982, Broadwell & Mungal 1991). Fit to two data points, Mungal & Dimotakis (1984) at $\phi = 1/8$ and Koochesfahani & Dimotakis (1986) at $\phi = 1/10$. Also requires

a input entrainment ratio. For this work the Dimotakis (1986) large scale entrainment model is used.

- Dimotakis (D87) mixing model (Dimotakis 1989). All parameters derived, no fitting performed. Requires an input entrainment ratio. For this work the Dimotakis 1986 large scale entrainment ratio model is used.

- Dimotakis (1986) large scale entrainment model . Only plotted for the mixed fluid composition ratio. This model is Reynolds number independent, and plotted as a reference, since it is used as an input for the other two models.

In this work, the models are presented using the Dimotakis (1986) volumetric entrainment ratio, and are calculated for mixing between two fluids of equal densities, temperatures and diffusivities. Finally, both models represent mixing as occuring solely between the two unmixed freestreams. These assumptions may not be appropriate for all of the experiments discussed here. Specifically, the experiments documented in Slessor (1998), while having a unity density ratio, have a temperature ratio roughly 10% higher, and thus a number-density ratio roughly 10% lower.

The temperature thicknesses (normalized by the downstream distance), versus Re_x are plotted in Figure 4.10, for $\phi = 1/8$. Re_x was chosen as the appropriate ordinate here since Re_δ would introduce an artificial correlation based on growth rate. The current results are in the range between the upper and lower values from earlier experiments. The diamonds (from Mungal *et al.* 1985) on these limits can be characterized by laminar (upper three diamonds), or turbulent boundary layers (lower three diamonds). The range of the current results suggests that the state of the high-speed stream boundary layer in the current experiments may be changing between cases. When compared to the results of Slessor *et al.* (1998), the current results (at the same Reynolds number) are bounded by the tripped and untripped cases.

Although there appears to be significant scatter in the current data at each Reynolds number, there are two (nominally identical) cases at each of the two Reynolds numbers. A closer examination of the current data shows two pairs of points at the

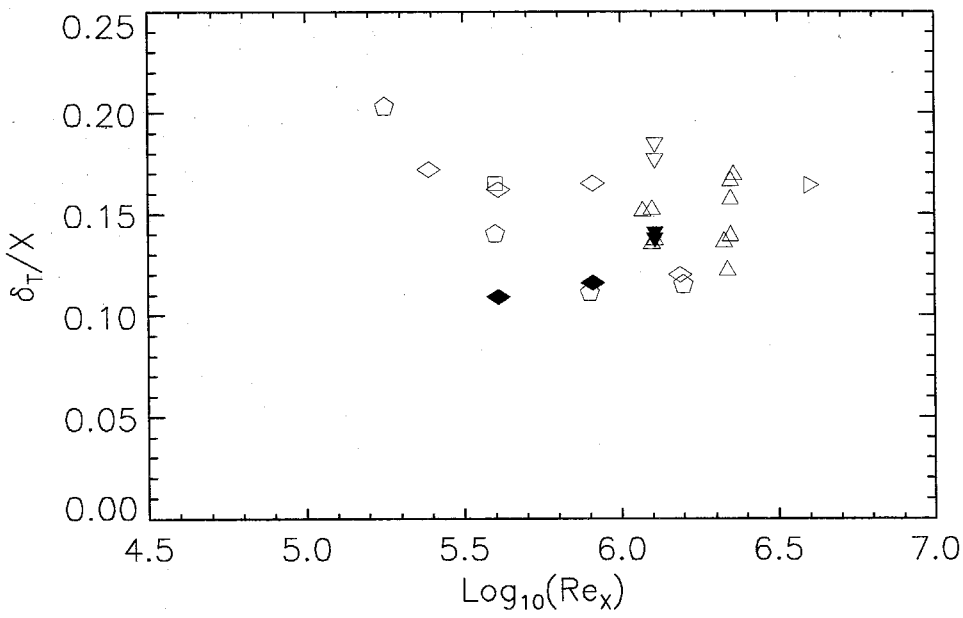

Figure 4.10: Temperature thickness, δ_T, *vs.* $\log(Re)$, $\phi = 1/8$. Square: Mungal & Dimotakis (1984), diamonds: Mungal *et al.* (1985), pentagons: Frieler (1992), upward pointing triangles: current work, downward pointing triangles: Slessor *et al.* (1998), rightward-pointing triangle: Slessor (1998). Filled symbols have tripped high-speed-stream splitter-plate boundary layers.

lower Reynolds number, while the higher Reynolds number has two triplets. These groupings are more than coincidental, since each corresponds to a single case, with the groupings within each Reynolds number corresponding to a change in which stream (upper or lower) was the high-speed stream. In assessing the data in the remainder of this chapter, the possibility that the scatter in the data is a result of an incomplete parameterization of the problem must be considered. Although the current study has concentrated on Reynolds number effects with constant velocity and density ratios, other parameters, such as the state of the high-speed-stream boundary layer, even at these high-Re conditions, far downstream, are also known to be important (Slessor *et al.* 1998).

The high-speed-stream boundary-layer momentum thicknesses, θ, are estimated at 0.11 mm (0.004 in) for $U_1 = 100$ m/s and 0.08 mm (0.003 in) for $U_1 = 165$ m/s,

using Thwaite's method for laminar boundary layers. The resultant Re_θ's of 635 and 815 suggest that the lower-speed cases should still have laminar boundary layers, while in the higher-speed cases the boundary layer may be transitioning to turbulent flow close to (within 5 cm of) the splitter tip. The state of the high-speed boundary layer may not be identical for lower-stream fast and upper-stream fast cases with the same velocities. The lower-stream side of the splitter plate has concave curvature in a region upstream of the splitter plate tip (see Figure A.5). Although this curvature is located in a region of favorable pressure gradient, it may affect the transition of these boundary layers, resulting in earlier transition of the lower-stream-fast flows.

These boundary layer thicknesses also give $x/\theta = 4500$ and 3300 for the higher and lower Reynolds number cases, well in excess of the $1000\,\theta$ suggested by Bradshaw (1996) as necessary for full development of the shear layer. These thicknesses also result in values of 64 and 47 for the "pairing parameter" used by Karasso & Mungal (1996), well in excess of the value of 22 suggested as required for fully developed flow.

The normalized temperature thicknesses for $\phi = 8$ are plotted in Figure 4.11 versus Re_x. Tilted squares represent the unstable-flow conditions: at the lower of the two Reynolds numbers investigated in the current work, the three lowest and the highest value are from Case 2h flows; at the higher Reynolds number, the two upper points are from the Case 4h flow, where the shear layer was flapping. For the remaining four points, $\delta_T/x \approx 0.15$, which is comparable to the higher growth rates from the $\phi = 1/8$ cases, and bracketed by the tripped and untripped cases of Slessor *et al.* (1998). This growth rate was higher than those from the high Reynolds-number, Frieler (1992), experiments, but comparable to the Mungal & Dimotakis (1984) point. The points also have lower growth rates than the Slessor (1998) point, which is somewhere between the Mungal & Dimotakis point and the low-Reynolds-number Frieler cases.

The highest-Reynolds number point of Frieler (1992) has a much lower growth rate than all other points. This is in part due to a narrow, high profile, but also due to the raw average-temperature data. On one of the freestreams, a data point has a negative value, causing any fit to tightly define that edge and possibly resulting in

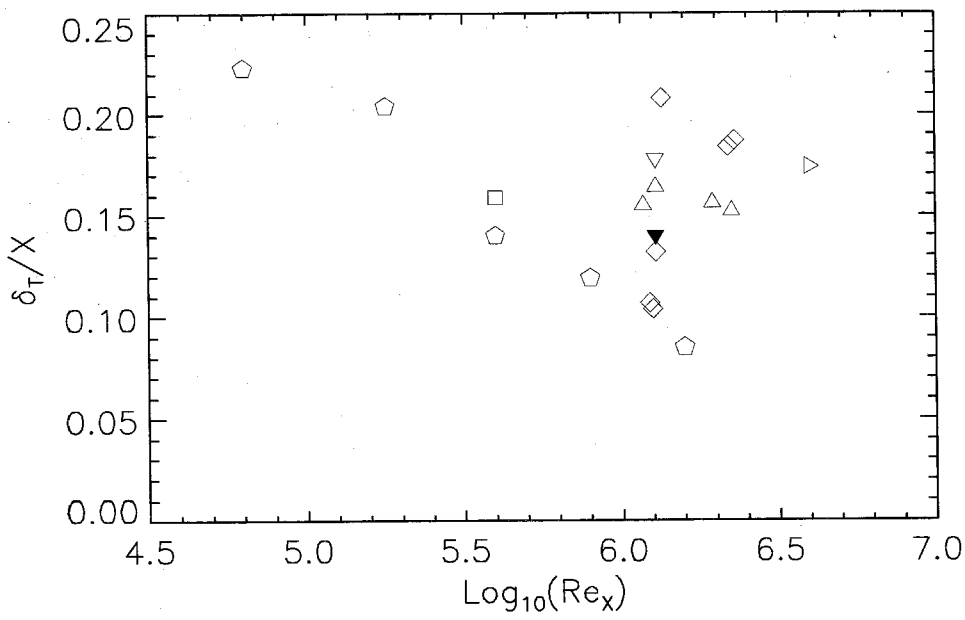

Figure 4.11: Temperature thickness, δ_T, *vs.* log(Re) for $\phi = 8$. Square: Mungal & Dimotakis (1984), pentagons: Frieler (1992), upward pointing triangles: current work, tilted squares: unstable flows, downward pointing traingles: Slessor *et al.* (1998), rightward pointing triangle: Slessor (1998). Filled symbols indicate tripped high-speed-stream boundary layers.

a fit narrower than the actual temperature-rise profile. This may have been caused by a lack of non-reacting temperature references, which are not needed for the lower-Reynolds number cases.

The product thickness (normalized by the downstream distance) for $\phi = 1/8$ is shown in Figure 4.12. The current results, like the temperature thickness, δ_T (Figure 4.10), are found to be in the range between the laminar and turbulent boundary-layer data of Mungal *et al.* (1985). At the lower Reynolds number, these results are near the lower limit, while for δ_T they were in the center of the range. The Slessor (1998) point is towards the upper end of this range.

The normalized product thickness for $\phi = 8$ is shown in Figure 4.13. Again, tilted squares mark unstable flows. At the higher Reynolds number, the results for the flapping (Case 4h) flow are similar to the other results, indicating that flagellation

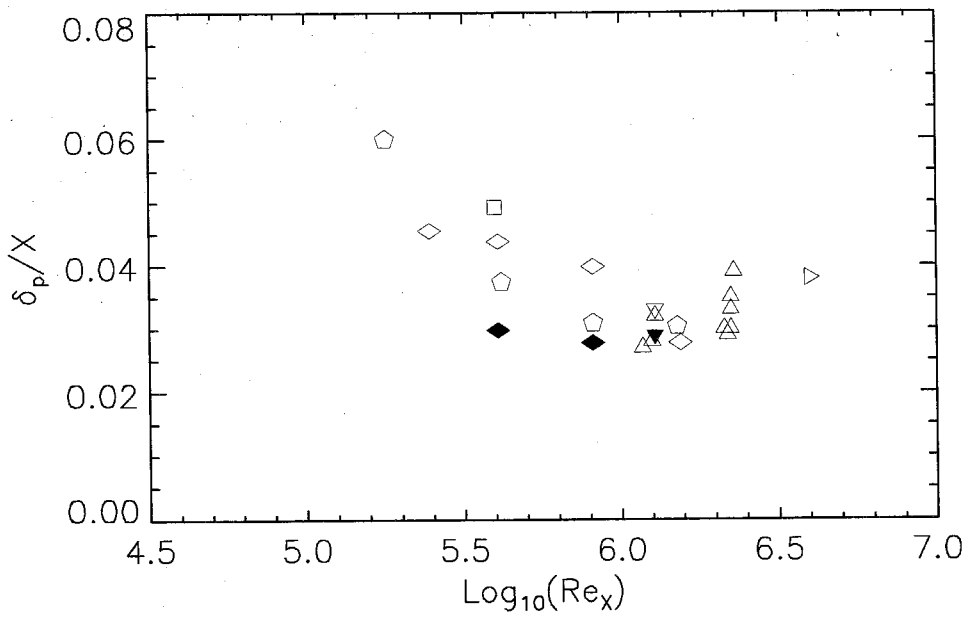

Figure 4.12: Product thickness, δ_p, at $\phi = 1/8$ *vs.* $\log_{10}(\mathrm{Re}_x)$. Square: Mungal & Dimotakis (1984), diamonds: Mungal *et al.* (1985), pentagons: Frieler (1992), upward pointing triangles: current work, downward pointing triangles: Slessor *et al.* (1998), rightward-pointing triangle: Slessor (1998). Filled symbols have tripped high-speed-stream splitter-plate boundary layers.

of the layer did not affect (molecular) mixing. The remaining cases have product thicknesses similar to the values of two of the Frieler (1992) high-Reynolds number cases. These values are higher than the product thicknesses at $\phi = 1/8$, as would be expected, since the shear layer preferentially entrains fluid from the high-speed stream. The highest Reynolds number case of Frieler (which had the anomalously low temperature thickness) is lower than the majority of the data, while the Slessor (1998) case, while higher than much of the data, is roughly the same as the Mungal & Dimotakis (1984) result. At the lower Reynolds number, the stable-flow results are bracketed by the Slessor *et al.* (1998) tripped and untripped cases.

Product fraction values at $\phi = 1/8$ are shown in Figure 4.14, along with predictions of the BBM (dotted line) and D87 (dashed line) models. At the lowest Reynolds number, two points (Case 1h) are significantly lower than the previous data (or ex-

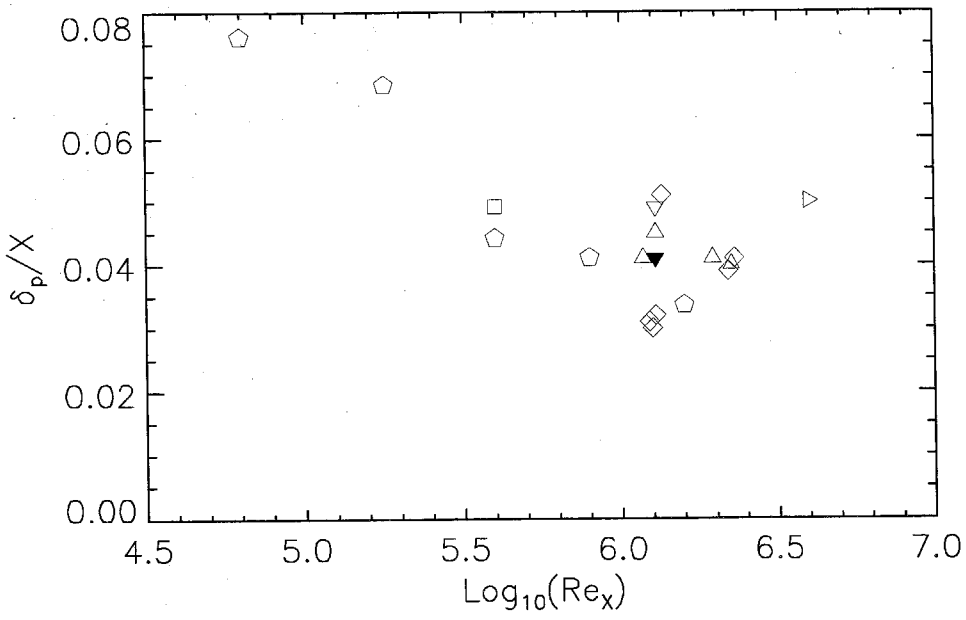

Figure 4.13: Product thickness, δ_p, *vs.* $\log(Re)$ for $\phi = 8$. Square: Mungal & Dimotakis (1984), pentagons: Frieler (1992), upward pointing triangles: current work, diamonds: unstable flows, downward pointing traingles: Slessor *et al.* (1998), rightward pointing triangle: Slessor (1998). Filled symbols indicate tripped high-speed-stream boundary layers.

trapolation thereof) would predict. The untripped cases from Slessor *et al.* (1998) have nearly the same (low) product fraction. The remaining points are consistent with an extension of the Mungal *et al.* (1985) trend. The data of Slessor (1998), suggest that this decreasing trend may not continue.

Product fraction values at $\phi = 8$ is shown in Figure 4.15, along with both model predictions. Again, the tilted squares represent unstable-flow cases. Otherwise, the current results are roughly 15% lower than the previous results The results from Slessor *et al.* (1998) and Slessor (1998) lie between the current results and the Mungal & Dimotakis (1984) point. The fractional decrease to the lower values at the higher Reynolds numbers is similar to the fractional decrease in product fraction at $\phi = 1/8$. The high-Reynolds-number case of Slessor (1998) may indicate that the observed decrease has stopped. The two highest Reynolds number cases from Frieler appear to

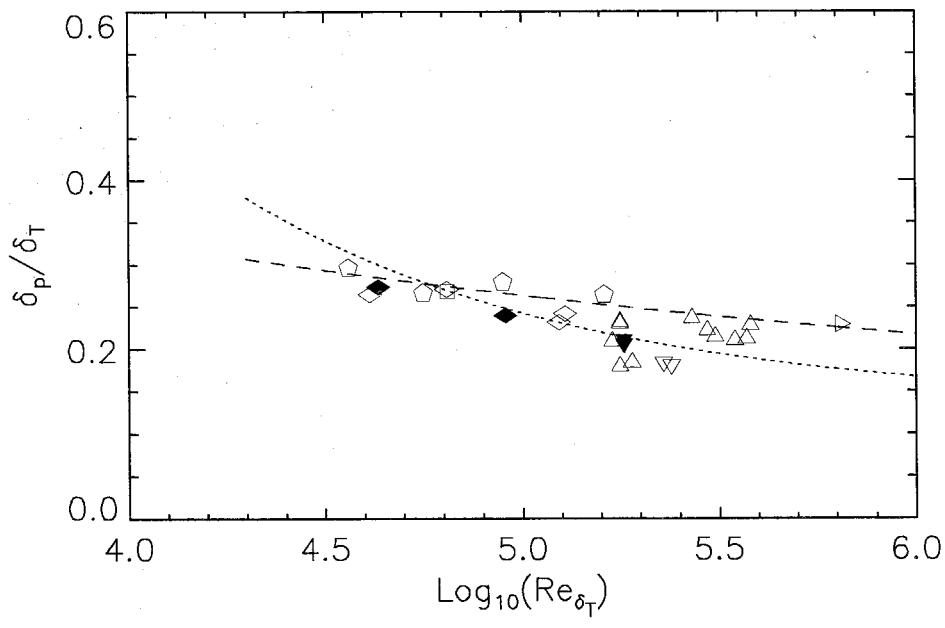

Figure 4.14: Product fraction, δ_p/δ_T, *vs.* $\log_{10}(Re)$ at $\phi = 1/8$. Square: Mungal & Dimotakis (1984), diamonds: Mungal *et al.* (1985), pentagons: Frieler (1992), upward pointing triangles: current work, downward pointing triangles: Slessor *et al.* (1998), rightward-pointing triangle: Slessor (1998). Filled symbols have tripped high-speed-stream splitter-plate boundary layers. Mixing model predictions: dotted line: BBM, dashed line: D87.

be diverging upwards. Of the two cases, the highest-Reynolds-number case was the one with the narrow, high profile that was noticeably different in both the δ_T and δ_p plots.

The mixed-fluid fraction is plotted in Figure 4.16, along with previous results and model predictions. No mixed-fluid points were derived from the unstable flows. Model predictions for this plot were created using Equation B.7 and the predictions for the individual product fractions. The current data have a significantly lower ($\approx 15\%$) value than the previous, lower-Reynolds-number flow data from Mungal & Dimotakis (1984) and Frieler (1992). However, the highest Reynolds number case from Frieler (1992) has a 40% difference in temperature thickness between the two halves of that flip experiment, and the results for mixed-fluid fraction and entrainment

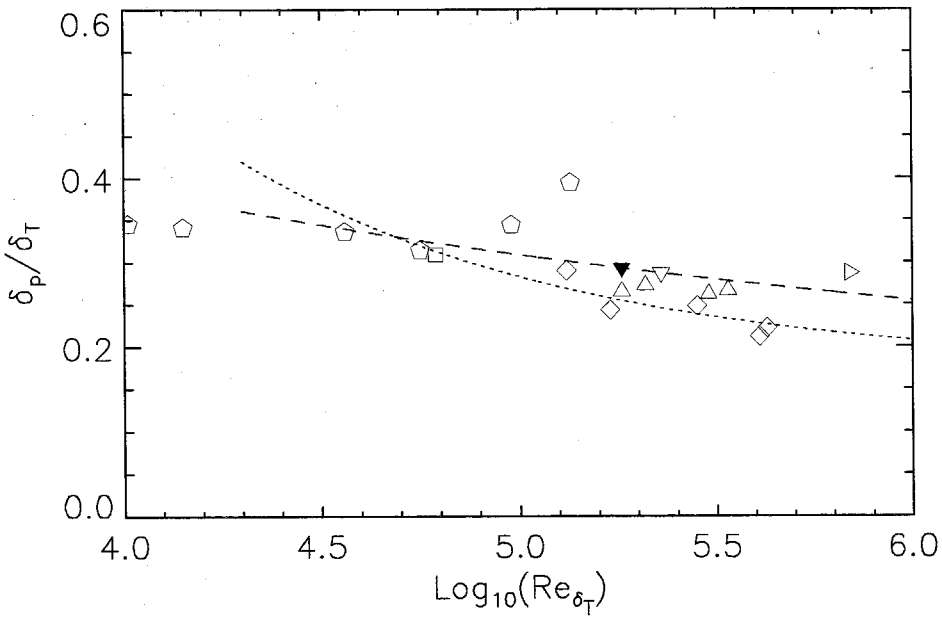

Figure 4.15: Product fraction, δ_p/δ_T, *vs.* $\log_{10}(Re)$ at $\phi = 8$. Square: Mungal & Dimotakis (1984), pentagons: Frieler (1992), upward pointing triangles: current work, tilted squares: unstable flows, downward pointing traingles: Slessor *et al.* (1998), rightward pointing triangle: Slessor (1998). Filled symbols indicate tripped high-speed-stream boundary layers. Mixing model predictions: dotted line: BBM, dashed line: D87.

ratio may not reflect the actual behavior of the individual flows. The current results were synthesized from all stable flow pairs, and have differences of $\lesssim 15\%$ in the temperature thicknesses. At the lower Reynolds number, the range of results is close to the range bracketed by the tripped and untripped results of Slessor *et al.* (1998). The results at the higher Reynolds number have less variation.

The current results, with the results of Slessor (1998), show a roughly 15% decrease of molecular mixing from the result of Mungal & Dimotakis (1984). This is consistent with the decrease observed by Mungal *et al.* (1985) continuing to the lower of the Reynolds numbers studied.

The calculated overall volumetric mixed-fluid composition ratio, $\mathcal{E}_v$, is plotted in Figure 4.17 along with model predictions. $\mathcal{E}_v$ is the volumetric ratio of high-speed

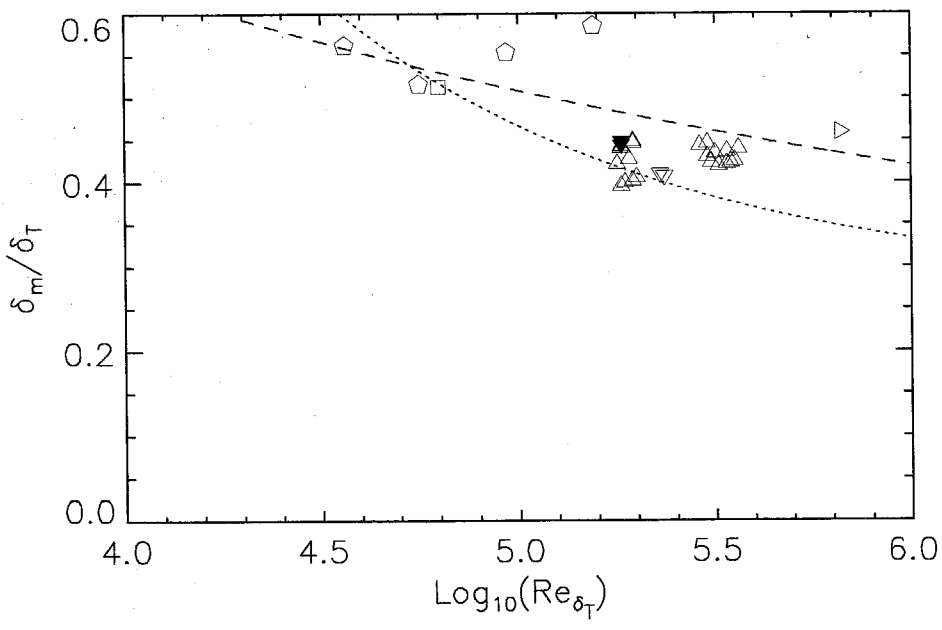

Figure 4.16: Mixed fluid fraction, δ_m/δ_T, *vs.* $\log_{10}(Re_{\delta_T})$. Square: Mungal & Dimotakis (1984), pentagons: Frieler (1992), upward pointing triangles: current work, downward pointing triangles: Slessor *et al.* (1998), rightward pointing triangle: Slessor (1998). Filled symbols indicate tripped high-speed-stream boundary layers. Mixing model predictions: dotted line: BBM, dashed line: D87.

fluid to low-speed fluid that, when homogeneously mixed, would result in the same ratio of product fraction at $\phi = 1/8$ to product fraction at $\phi = 8$ as observed in experiment. The data points are calculated using equation B.8 to generate a number (molar) mixed-fluid composition ratio, $\mathcal{E}_n$ (similiar to $\mathcal{E}_v$, but is the molar ratio, not the volumetric ratio), and Equation B.9 to convert the molar mixed-fluid composition ratio into a volumetric mixed-fluid composition ratio.

The volumetric mixed-fluid composition ratio was used to try to minimize the effects of the differences between the Slessor (1998) point and the model assumptions. For the remainder of the points the values of $\mathcal{E}_n$ and $\mathcal{E}_v$ are within 4%. However, for the Slessor (1998) point, there is roughly a 10% change between the two. The Dimotakis (1986) value of E_v (which is the volumetric ratio of high-speed fluid to low-speed fluid entrained into the shear layer) should remain constant for all these flows, where

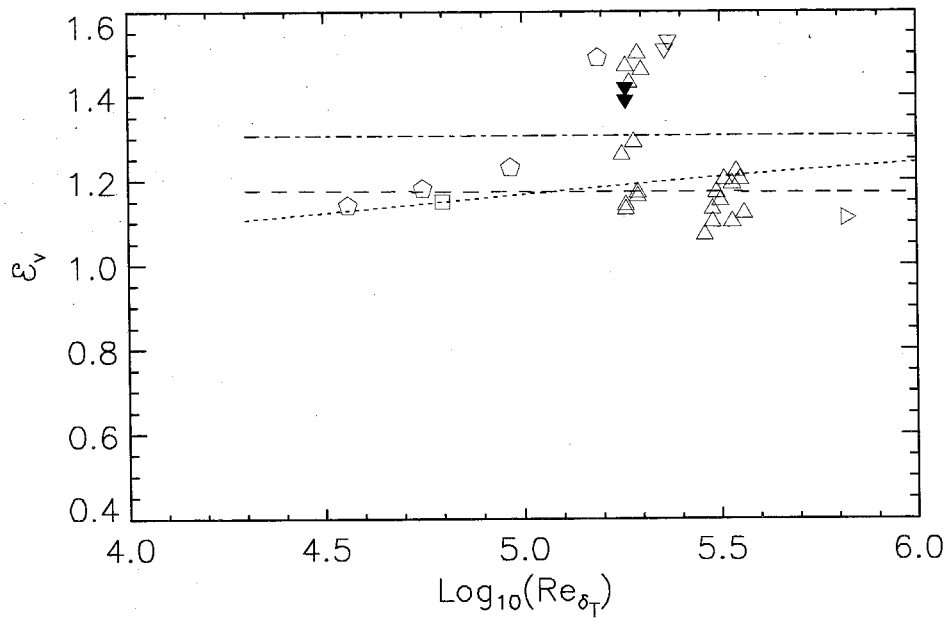

Figure 4.17: The measured volumetric mixed-fluid composition ratio, $\mathcal{E}_v$. Square: Mungal and Dimotakis (1984), pentagons: Frieler (1992), upward pointing triangles: current work, downward pointing triangles: Slessor *et al.* (1998), rightward pointing triangle: Slessor (1998). Filled symbols indicate tripped high-speed-stream boundary layers. Mixing model predictions: dotted line: BBM, dashed line: D87, dot-dashed line: Dimotakis (1986) large scale entrainment prediction.

the corresponding large-scale number entrainment ratio E_n (similiar to E_v, but is the molar ratio, not the volumetric ratio) would be roughly 10% higher for the Slessor (1998) case. Since the models are calculated using the Dimotakis (1986) E_v, and an assumption of unity number-density ratio, it is more appropriate to scale using volumetric measures, to avoid having to correct all three models for the Slessor (1998) point. (Note that the value of $\mathcal{E}_n$ for the Slessor 1998 point is 1.25.)

The predictions from the BBM and D87 mixing models are calculated from the predicted product fractions using equation B.8, assuming unity number density ratio. The dot-dashed line shows the predicted value of the overall entrainment ratio as predicted by the Dimotakis (1986) large-scale entrainment model, *i.e.*, no diffusion layers. Notice that both the BBM and D87 mixing models predict measured

mixed-fluid composition ratios significantly lower than that of the Dimotakis (1986) entrainment model, although both models use that entrainment ratio as an input.

At lower Reynolds numbers, some of the current results (and the highest Reynolds-number Frieler case) are significantly higher than the rest of the measurements, and are in fact higher than the highest model predictions. Additionally, both the tripped and untripped flows from Slessor *et al.* (1998) yield this same high value of the mixed fluid composition ratio. At the higher Reynolds number, the current results are close to the measured value from Mungal & Dimotakis (1984). For the highest Reynolds number case (Slessor 1998) is closer to unity.

4.3 Comparison with "cold chemistry" results

The "cold chemistry" response is different than the chemically reacting mixed-fluid response. Based on the integral of the response function, Island (1997) estimates the response as corresponding to a $\phi = 1/16, 16$ flip experiment. Based on the mixture fraction where the response reaches a value of 0.5, the "cold chemistry" equivalent would be closer to $\phi = 1/160, 160$. The important point is that the response functions are different, with the "cold-chemistry" response rising very quickly, but approaching unity slowly. In contrast, the chemical-reaction response rises linearly to unity, with a large portion of the response *at* unity. For fluid composition PDFs with significant composition probabilities near pure-freestream values, such differences in response will produce significant differences in inferred mixing.

The "cold-chemistry" results have been compiled as averages of instantaneous spatial fields (images). The chemical-reaction method measurements have been of temporally-averaged, single-x-location measurements. These measurements should agree if there is no correlation between velocity and the mixed-fluid state. A correlation between these quantities could result in systematic differences between the data. It should be noted that this is not an inherent difference in the methods, but a difference in the implementations.

Comparison of the current results with the "cold chemistry" measurements (Clemens

& Paul 1995, Island 1997) are complicated by the superposition of compressibility and Reynolds-number effects. Figure 4.18 shows the convective Mach number, M_c, as a

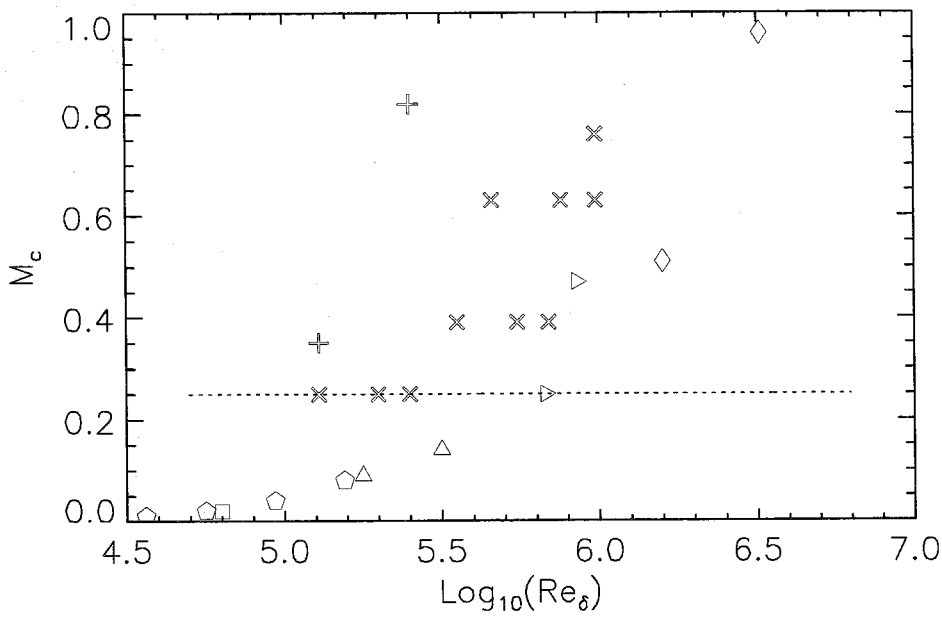

Figure 4.18: Convective Mach number, M_c, *vs.* $\log_{10}(Re_\delta)$. Square: Mungal & Dimotakis (1984), pentagon: Frieler (1992), upward pointing triangles: current, rightward pointing triangle: Slessor (1998), crosses: Clemens & Paul (1995), xs: Island (1997), vertical diamonds: Hall *et al.* (1991). The dotted line marks the upper limit for which comparisons have been made for the purpose of investigating Reynolds number effects in incompressible flows.

function of Reynolds number. The chemically-reacting, compressible-flow ($M_c > 0.5$) data of Hall *et al.* (1991) are included for reference. The convective Mach numbers of the "cold-chemistry" results of Clemens & Paul (1995) and Island (1997) are all from flows with $M_c \geq 0.25$. For the purposes of this incompressible flow study, comparison of the current results with the "cold-chemistry" results has been limited to $M_c \leq 0.25$. As discussed above in context of the Slessor *et al.* (1998) case, even such a low-compressibility flow may be subject to compressibility effects that may mask the weak effects of Reynolds number. Any comparison of the "cold-chemistry" data to the chemical-reaction data must acknowledge the higher compressibility of

the "cold-chemistry" cases.

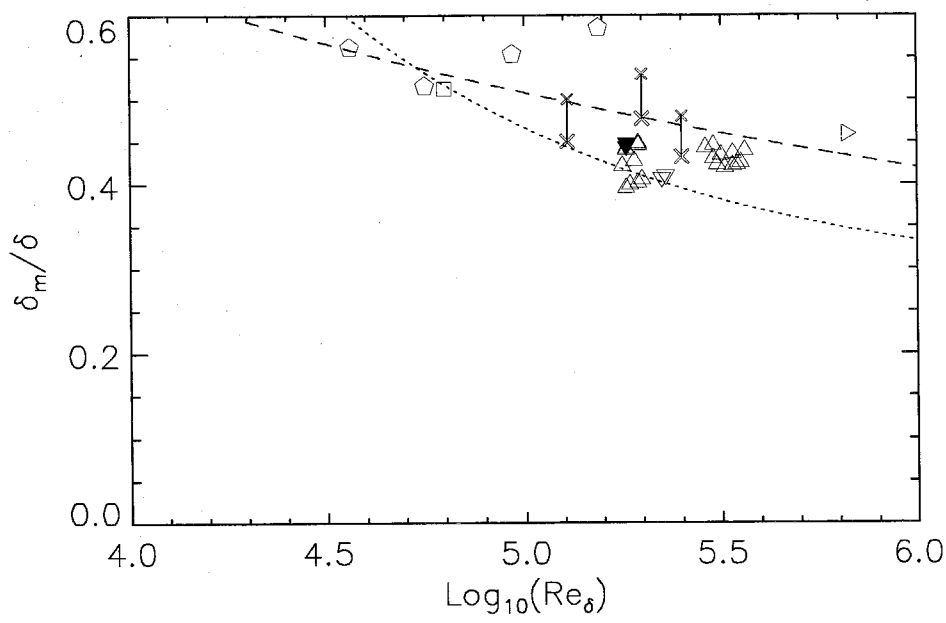

Figure 4.19: Mixed fluid fraction, δ_m/δ_T, *vs.* $\log_{10}(Re_\delta)$ for $M_c \leq 0.25$. Square: Mungal & Dimotakis (1984), pentagons: Frieler (1992), upward pointing triangles: current work, downward pointing triangles: Slessor *et al.* (1998), rightward pointing triangle: Slessor (1998), Xs: Island (1997) small Xs are reported values, large Xs (connected by lines) are best estimate values (see text). Filled symbols indicate tripped high-speed-stream boundary layers. Mixing model predictions: dotted line: BBM, dashed line: D87.

Figure 4.19 shows the chemically-reacting-flow and "cold-chemistry" results for $M_c \leq 0.25$. In comparing the Island (1997) $M_c = 0.25$ data, two points must be considered. First, Island used the 5% scalar thickness, δ_5, to normalize his data, while all other data were normalized by the 1% thickness, δ_1. The 5% thicknesses of the current results were typically 8-12% lower than the 1% thicknesses. If similar scaling holds for the Island data, his values should be decreased by 8-12% to permit a direct comparison with the other results. In Figure 4.19, a best estimate for a 1% based thickness was made by decreasing the values by 10%. This is indicated in Figure 4.19 by small Xs for the reported values, connected by lines to the best estimates marked

M_c	Re_{δ_1}	δ_m/δ_1
0.35	1.3×10^5	0.45
0.82	2.5×10^5	0.48

Table 4.2: Mixed-fluid fraction from the "cold-chemistry" experiments of Clemens & Paul (1995).

M_c	Re_{δ_1}	δ_m/δ_5	$0.85 \times \delta_m/\delta_5$
0.39	3.51×10^5	0.53	0.46
	5.46×10^5	0.54	0.47
	6.97×10^5	0.56	0.47
0.63	4.62×10^5	0.57	0.48
	7.51×10^5	0.60	0.51
	9.72×10^5	0.63	0.54
0.76	9.80×10^5	0.62	0.53

Table 4.3: "Cold-chemistry" results of Island(1997) for $M_c > 0.25$. The final column shows the effect of reducing the reported values by 10%.

by the large Xs. The second point to consider is that the $M_c = 0.25$ case of Island (1997) was produced by accelerating the flow downstream of the splitter tip, and this must be considered when comparing the flow with self-similar (non-accelerating) shear layers, in view of the sensitivity of the shear layer to inflow conditions, as seen in Slessor *et al.* (1998).

The three values from the lowest compressibility case of Island (1997), when adjusted downwards 10% (for the difference between δ_5 and δ_1) from the reported, plotted value, is relatively close to the values from the current work. The values compare closely with the data of Slessor (1998), which is at the same compressibility, M_c, but at a significantly higher Reynolds number. Figure 4.19 includes bars on the Island (1997) data that show the effect of such a 10% decrease in the mixed fluid fraction.

The "cold-chemistry" results at higher M_c were not shown in Figure 4.19. Both Clemens & Paul (1995), and Island (1997) found increases in mixing with increasing M_c and Reynolds number, but the two were intimately linked. The Clemens & Paul (1995) results, shown in Table 4.2are close to the values from the current study, with the higher-Reynolds number, more-compressible case showing a small increase

in mixed-fluid fraction. Due to a facility problem with the Island (1997) experiments, air leaked into one of the freestreams, and Island estimated that measurements at his highest three convective Mach numbers may have been 5-10% too high. Additionally, this effect may increase in magnitude (within this range) with increasing M_c. The data at the higher compressibility, shown in Table 4.3, even if reduced by 15% to account for both air leakage and the δ_5-δ_1 difference, would be higher than the chemically-reacting data. However, these values of M_c already correspond to significantly compressible flows, and the effects of compressibility have not been separated. In general, applying the "cold-chemistry" data to an understanding of the effects of Reynolds number is complicated by the mixture of Mach-number and Reynolds-number effects.

Chapter 5 Conclusions

Experiments have been performed in chemically-reacting, incompressible, subsonic, shear-layer flows to measure molecular mixing. The results addressed a range of Reynolds numbers previously unexplored and in-between those in previous investigations of incompressible shear layers and supersonic (compressible) shear layers. The difference in both Reynolds number and Mach number in these two sets prevented conclusions from being drawn about whether differences in behavior were attributable to viscosity or compressibility effects, or some combination of the two. Combined with results from previous incompressible-shear-layer flows, the present results span this gap, providing information on the behavior of mixing in this Reynolds number range.

The present, subsonic-flow experiments focused on two basic conditions, for which both velocity and chemistry "flip" experiments were performed. These permitted both outer-flow attributes to be measured, such as the local shear-layer transverse extent, δ, as well as molecular mixing, such as the molecularly-mixed fluid fraction, δ_m/δ, within the layer as well as the volumetric mixed-fluid composition ratio, $\mathcal{E}_v$.

In the course of these investigations, it was appreciated that this particular Reynolds number range corresponded to a flow regime for which the state of the high-speed stream inflow boundary layer in the splitter-plate trailing-edge region was particularly sensitive to disturbance levels and, for the lower Reynolds number values, could be tripped, or not, to substantially alter its state, as well as of the flow far downstream. Investigations on the sensitivity of the flow to inflow/initial conditions were documented separately (cf. Slessor *et al.* 1998).

The experiments described above, collectively with previous and other data, lead to the following conclusions.

1. The flow is sensitive to a host of influences, such as inflow/initial conditions,

initial flow curvature, test-section geometry (outflow conditions), effects of compressibility at the highest Reynolds numbers, acoustic disturbances, etc. In view of this sensitivity, a separation of the weak effects of viscosity, i.e., Reynolds number, from other effects presents a challenge, to say the least.

2. The decrease in product fraction with increasing Reynolds number, documented previously by Mungal *et al.* (1985) at a stoichiometric-mixture ratio of $\phi = 1/8$, persists to the lower Reynolds numbers studied here ($Re = 1.5 \times 10^5$). The product fraction at $\phi = 8$ and the mixed-fluid fraction both show similar fractional decreases from the values of Mungal & Dimotakis (1984) at the lower Reynolds number, which, however, differs from the results of Frieler (1992).

3. Within the uncertainties and reproducibility of these measurements, the product fraction and mixed-fluid fraction are found not to decrease further at higher Reynolds numbers, including the recent data of Slessor (1998), at a higher Reynolds number yet, with the exception of one case, for which the product fraction is lower. This may indicate the attainment of an asymptotic (Reynolds-number-independent) mixing state. On the other hand, and as noted above, changes in the inflow boundary layer state, other influences, as well as encroaching compressibility effects, the latter as discussed by Slessor (1998), render a firm conclusion on this matter infeasible at this time.

4. The measured volumetric mixed-fluid composition ratio, $\mathcal{E}_v$, indicates a transitional regime spanned by the present and previous data, within which the behavior is different from that at both lower and higher Reynolds numbers. Present estimates of $\mathcal{E}_v$ at the highest Reynolds number are close to previously-estimated values by Mungal & Dimotakis (1984), and Slessor (1998), as well as those derived from the Dimotakis (1987) mixing model. At the lower Reynolds number, estimates of $\mathcal{E}_v$ exceed previous estimates, as well as those derived from the Dimotakis (1986), large-scale entrainment model. However, this agrees with the results of Frieler (1992) at nearly the same Reynolds number, as well as with the results of Slessor *et al.* (1998) at the same nominal conditions. The remain-

der of the values at the lower Reynolds number are close and slightly above the values from Mungal & Dimotakis (1984), Slessor (1998), and the remainder of the Frieler (1992) points. The current results and the data of Slessor (1998) suggest that the volumetric mixed-fluid composition ratio may slowly be decreasing towards unity with increasing Reynolds number.

5. The current results are in accord with the mixed-fluid fraction results of the "cold-chemistry" investigations of Island (1997) at $M_c = 0.25$, when best-estimate corrections are made for the different definitions of shear-layer width employed in the analysis of the two experiments. At the higher compressibility cases, corrections also need to include the effects of air-leakage in the Island (1997) experiments, which are only roughly estimated for most of the cases. Even after these corrections, it is likely that mixed fluid fraction values from the higher-compressibility cases will remain above the levels measured in the present study.

6. The current results are also in accord with the mixed-fluid fraction results from the "cold-chemistry" investigations of Clemens & Paul (1995) at $M_c = 0.35$.

7. The lower-Reynolds-number results involving Case 1h, the cases from Slessor *et al.* (1998), and the Frieler (1992) highest-Reynolds-number results appear to have a significantly different behavior from the rest of the results. Whether this is due to the similar Reynolds numbers or to some other effect could not been determined.

Bibliography

Batt, R. (1977). Turbulent mixing of passive and chemically reacting species in a low-speed shear layer. *Journal of Fluid Mechanics*, 82(pt 1):53–95.

Bogdanoff, D. (1983). Compressibility effects in turbulent shear layers. *AIAA Journal*, 21(6):926–927. (TN).

Bradshaw, P. (1966). The effect of initial conditions on the development of a free shear layer. *Journal of Fluid Mechanics*, 26(2):225–236.

Breidenthal, R. (1981). Structure in turbulent mixing layers and wakes using a chemical reaction. *Journal of Fluid Mechanics*, 109:1–24.

Broadwell, J. and Breidenthal, R. (1982). A simple model of mixing and chemical reaction in a turbulent mixing layer. *Journal of Fluid Mechanics*, 125:397–410.

Broadwell, J. E. and Mungal, M. G. (1991). Large-scale structures and molecular mixing. *Physics of Fluids A*, 3(5):1193–1206.

Brown, G. and Roshko, A. (1974). On density effects and large structure in turbulent mixing layers. *Journal of Fluid Mechanics*, 64(4):775–816.

Clemens, N. and Paul, P. (1995). Scalar measurements in compressible axisymmetric mixing layers. *Physics of Fluids*, 7(5):1071–1081.

Dimotakis, P. (1986). Two-dimensional shear-layer entrainment. *AIAA Journal*, 24(11):1791–1796.

Dimotakis, P. (1987). Turbulent shear layer mixing with fast chemical reactions. In *US-France Workshop on Turbulent Reactive Flows*. Published in 1989 in Turbulent Reactive Flows (Lecture Notes in Engineering 40).

Dimotakis, P. (1989). *Turbulent Shear Layer Mixing with Fast Chemical Reactions*, volume 40 of *Lecture Notes in Engineering*, pages 417–485. Springer-Verlag.

Dimotakis, P. (1991). *Turbulent Free Shear Layer Mixing and Combustion*, volume 137 of *Progress in Astronautics and Aeronautics*, chapter 5, pages 265–340. AIAA.

Dimotakis, P. and Hall, J. (1987). A simple model for finite chemicalkinetics analysis of supersonic turbulent shear layer combustion. In *AIAA/SAE/ASME/ASEE 23rd Joint Propulsion Meeting.* Paper 87-1879.

Dimotakis, P. E. and Brown, G. L. (1976). The mixing layer at high Reynolds number: Large-scale dynamics and entrainment. *Journal of Fluid Mechanics*, 78(3):535–560.

Egolfopoulos, F., Dimotakis, P., and Bond, C. (1996). On strained flames with hypergolic reactants: The $H_2/NO/F_2$ system in high-speed, supersonic and subsonic mixing-layer combustion. In *Twenty-Sixth Symposium (International) on Combustion.* The Combustion Institute, Pittsburgh. Paper 310.

Fiedler, H. E. (1974). Transport of heat across a plane turbulent mixing layer. *Advances in Geophysics*, 18A:93–109.

Frieler, C. and Dimotakis, P. (1988). Mixing and reaction at low heat release in the non-homogeneous shear layer. In *First National Fluid Dynamics Congress*, pages Paper 88–3623.

Frieler, C. E. (1992). *Mixing and Reaction in the Subsonic 2-D Turbulent Free Shear Layer.* Ph.D. thesis, California Institute of Technology.

Hall, J. (1991). *An Experimental Investigation of Structure, Mixing and Combustion in Compressible Turbulent Shear Layers.* Ph.D. thesis, California Institute of Technology.

Hall, J. and Dimotakis, P. (1989). Design overview of the supersonic hydrogen-fluorine facility (V4.0). Technical report, GALCIT.

Hall, J., Dimotakis, P., and Rosemann, H. (1991). Some measurements of molecular mixing in compressible turbulent shear layers. *AIAA 22nd Fluid Dynamics, Plasma Dynamics and Lasers Conference*, AIAA paper 91-1719.

Hermanson, J. and Dimotakis, P. (1989). Effects of heat release in a turbulent, reacting shear layer. *Journal of Fluid Mechanics*, 199:333–375.

Island, T. C. (1997). *Quantitative Scalar Measurements and Mixing Enhancement in Compressible Shear Layers.* Ph.D. thesis, Stanford University.

Karasso, P. and Mungal, M. (1996). Scalar mixing and reaction in plane liquid shear layers. *Journal of Fluid Mechanics*, 323:23–63.

Kee, R., Rupley, F., and Miller, J. (1989). Chemkin-II: A fortran chemical kinetics package for the analysis of gas-phase chemical kinetics. Technical Report SAND89-8009, Sandia National Laboratories.

Kee, R., Warnatz, J., and Miller, J. (1990). A FORTRAN computer code package for the evaluation of gas-phase viscosities, conductivities, and diffusion coefficients. Technical Report SAND83-8209, Sandia National Laboratories.

Konrad, J. H. (1976). *An Experimental Investigation of Mixing in Two-Dimensional Turbulent Shear Flows with Applications to Diffusion Limited Chemical Reactions.* Ph.D. thesis, California Institute of Technology.

Kontratiev, V. (1972). *Rate Constants of Gas-Phase Reactions.* Office of Standard Reference Data, NBS.

Koochesfahani, M. and Dimotakis, P. (1986). Mixing and chemical reactions in a turbulent liquid mixing layer. *Journal of Fluid Mechanics*, 170:83–112.

Koochesfahani, M., Dimotakis, P., and Broadwell, J. (1985). A "flip" experiment in a chemically reacting turbulent mixing layer. *AIAA Journal*, 23(8):1191–1194.

Koochesfahani, M. and MacKinnon, C. (1991). Influence of forcing on the compositions of mixed fluid in a two-stream shear layer. *Physics of Fluids A*, 3(5):1135–1142.

Masutani, S. and Bowman, C. (1986). The structure of a chemically-reacting plane mixing layer. *Journal of Fluid Mechanics*, 172:93–126.

Miller, M., Bowman, C., J.A., M., and R.J., K. (1989). "a model for chemical reaction in a compressible mixing layer". Western States Section/The Combustion Institute Fall Meeting Paper 89-110.

Mungal, M. and Dimotakis, P. (1984). Mixing and combustion with low heat release in a turbulent shear layer. *Journal of Fluid Mechanics*, 148:349–382.

Mungal, M. and Frieler, C. (1988). The effects of Damköhler number in a turbulent shear layer. *Combustion and Flame*, 71:23–34.

Mungal, M., Hermanson, J., and Dimotakis, P. (1985). Reynolds number effects on mixing and combustion in a reacting shear layer. *AIAA Journal*, 23(9):1418–1423.

Mungal, M. G. (1983). *Experiments on Mixing and Combustion with Low Heat Release in a Turbulent Shear Flow.* Ph.D. thesis, California Institute of Technology.

Papamoschou, D. (1989). Structure of the compressible turbulent shear layer. AIAA 27th Aerosace Sciences Meeting, Paper 89-0126.

Paul, P. and Clemens, N. (1993). Subresolution measurements of unmixed fluid using electronic quenching of NO $A^2\,\Sigma^+$. *Optics Letters*, 18(2):161–163.

Rajagopalan, S. and Antonia, R. (1981). Properties of the large scale structure in a slightly heated turbulent mixing layer of a plane jet. *Journal of Fluid Mechanics*, 105:261–281.

Slessor, M. D. (1998). *Aspects of turbulent-shear-layer dynamica and mixing.* Ph.D. thesis, California Institute of Technology.

Slessor, M. D., Bond, C. L., and Dimotakis, P. E. (1998). Turbulent shear-layer mixing at high reynolds numbers: effects of inflow conditions. *Journal of Fluid Mechanics*, 376:115–138.

Appendix A Supersonic shear layer facility

A.1 Overview

The supersonic shear-layer facility (S^3L) is documented in Hall (1991) and Hall & Dimotakis (1989) in its original supersonic configuration. The S^3L is a two-stream blow-down wind tunnel. The two streams (the upper stream and the lower stream, named by position in the test section) are supplied from independent pressure vessels. The gas delivery systems are shown in figure A.1. Gases used are inert gases (He, Ar,

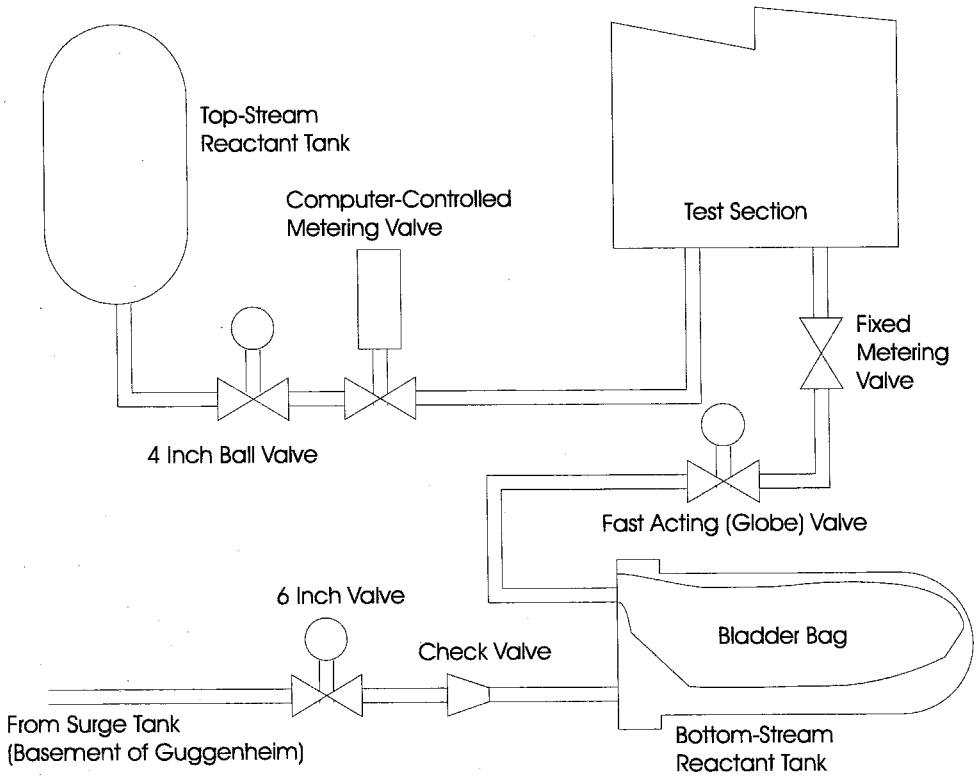

Figure A.1: Gas delivery systems.

N_2), H_2 (upper stream), NO (upper stream), F_2 (lower stream) and C_2H_4. H_2, NO and F_2 are used in dilute quantities (no greater than 16, 1, and 8% respectively) in chemically reacting experiments. C_2H_4 is used in non-reacting experiments to provide a higher index of refraction, resulting in increased optical signal.

The lower stream is supplied from the lower-stream reactant tank, a 0.57 m^3 (20 ft^3) pressure vessel rated for 1 MPa (150 psig). The inside is partitioned by a teflon bladder bag: one side contains the gas supplied to the lower-stream flow, the other side is connected to a much larger (12.7 m^3, 450 ft^3) pressure vessel. This pressure vessel (the surge tank) is rated for 0.7 MPa (100 psi). The surge tank limits the pressure drop in the lower-stream reactant tank to less than 5% over a run. With the supply pressure almost constant during a run, the lower-stream flow rate is set using a passive, fixed metering valve. The flow is controlled using a 7.6 cm (3 in) globe valve (the fast-acting valve) as a shut-off.

The gas mixture in the lower-stream reactant tank is loaded by a two-step process. The gases are first loaded into the lower-stream mixing vessel comprised of a length of monel pipe, volume 0.04 m^3 (1.4 ft^3). Mixture ratios are measured by recording the loaded partial pressures of each component. After loading the mixing vessel, the contents are transferred to the lower-stream reactant tank. Typical experiments require four to five of these load/transfer cycles. The gas remaining in the mixing vessel at the end of this procedure is subtracted from the loaded gas to determine mixture fractions.

The upper stream is supplied from the upper-stream reactant tank, a 1.2 m^3 (42 ft^3) pressure vessel rated for 10.3 MPa (1500 psi) at a temperature of 600 K (620° F). The tank pressure rating was chosen to accommodate a supply of $M = 3.2$ stream at atmospheric pressure. Since the pressure in this tank can drop as low as 50% of its initial value, a fixed metering valve would not provide steady flow. Instead, a computer-controlled metering valve is used. As the metering valve is not gas tight in the fully closed position, a 10 cm (4 in) ball valve (the four-inch valve) is used as a shut-off.

The mixture in the upper-stream reactant tank is determined by recording the

partial pressures loaded of each component. However, unlike the lower-stream reactants, the gases are loaded directly into the reactant tank.

Figure A.2 shows the test section. Each stream enters at the left and passes

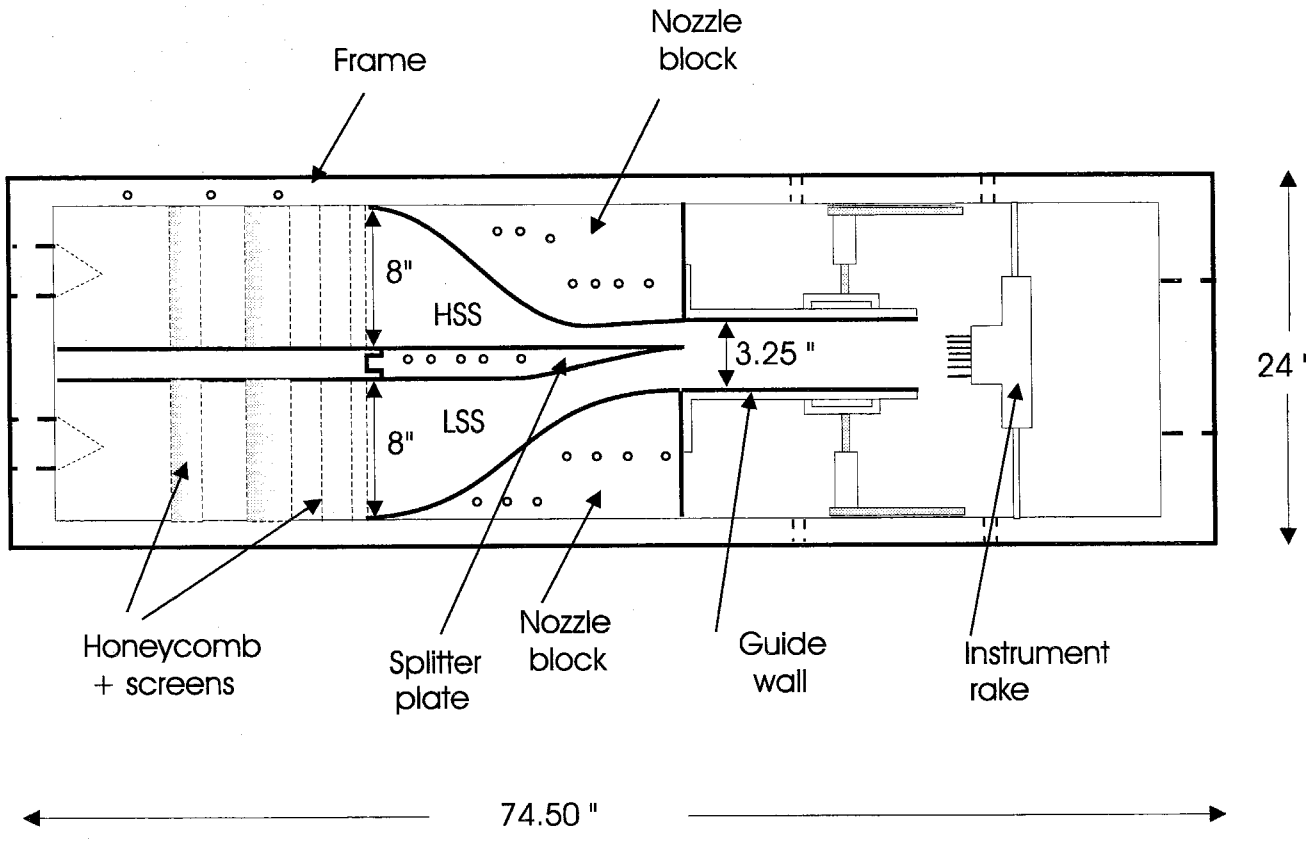

Figure A.2: Test section, showing the inlets, plena, test cell and exit region.

through a perforated-plate diffuser, a series of screens and honeycomb, and a nozzle. The nozzles are formed by the splitter plate and a removable aluminium nozzle block. By using fixed (but replaceable) nozzle blocks, very accurate nozzle contours can be used for each flow condition. At the end of the splitter plate, the two streams meet and form a planar free shear layer at or near atmospheric pressure. The flow is contained between two adjustable guide walls, which converge or diverge, as necessary, to maintain the esired pressure gradient (zero for these experiments). An instrument rake is located downstream of the guide-walls with probes extending upstream past the end of the guide-walls. The flow passes the rake and exits the test section, at a

location 35 cm (14 in) past the end of the guide-walls, into the shower duct.

The gas handling system (A.3) collects, cools, neutralizes and dilutes the exhaust

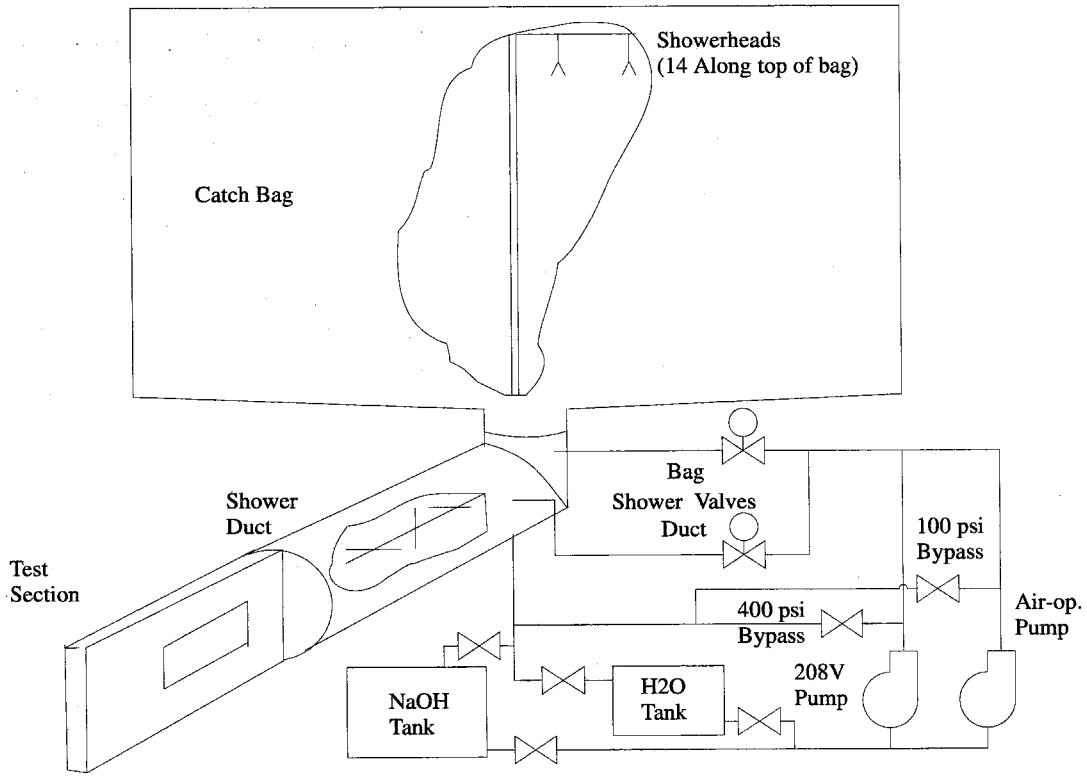

Figure A.3: The exhaust-gas handling system.

gases produced by the facility. In reacting runs, the exhaust consists of a hot mixture of inert gases, reactant gases, HF, and NOF. As the gas travels through the shower duct, it is sprayed with a NaOH/water solution which starts to neutralize F_2, HF, and NOF, while providing evaporative cooling. The exhaust is collected in the catch bag, where an additional set of showers complete the neutralization. At this point, the only hazardous gas left is H_2. The H_2 is diluted in two stages: N_2 is added to the catch bag, and then the catch bag contents are mixed with air as they are vented to the atmosphere. Non-reacting runs using C_2H_4 require the two dilution steps, but do not require the use of the showers. The H_2O tank contents are used to flush NaOH solution out of the shower system to prevent corrosion.

The experiments are controlled by a DEC LSI-11/73 CPU based, RT-11 computer.

The computer opens (and, at the end of the run, closes) the two shutoff valves (the four-inch valve on the upper-stream side, the fast-acting valve on the lower-stream side), triggers data acquisition and schlieren photography, and controls the position of the upper-stream metering valve.

The S^3L is located in and around a one-story building to the south of the Guggenheim Laboratory on the campus of the California Institute of Technology. The laboratory layout is shown in A.4. The two reactant tanks and the test section are located

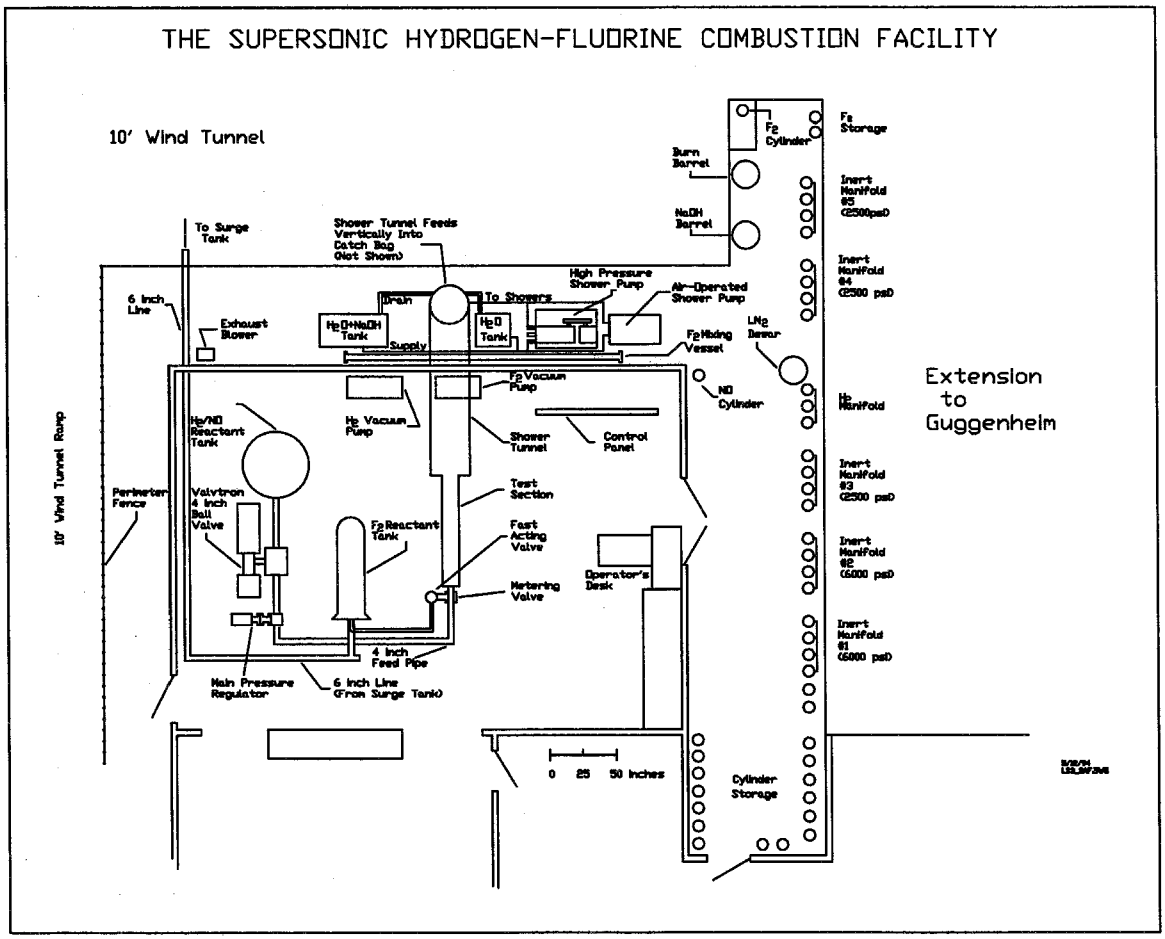

Figure A.4: Layout of the Supersonic Shear Layer Facility.

inside the building and all gas supplies (reactant and inert gases) are located in the courtyard to the east of the building. The surge tank is located in the basement and

subbasement of Guggenheim[1]. The exit of the shower duct and the plumbing of the exhaust neutralization system are located between the laboratory and Guggenheim; the catch bag is hung in an enclosure mounted on the south wall of Guggenheim.

A.2 Test-section modifications

The splitter plate had originally been supported by the test-section frame (at the upstream end) and a pair of 0.95 cm (0.375 in) alignment pins near the downstream end. During initial tests at an upper-stream Mach number of 2.5, the alignment pins sheared (the upper-stream plenum pressure was approximately 1.8 MPa (18 atm), for a total force of approximately 44 kN (10,000 lbs) on each pin). For further experiments, the splitter plate was supported by a 2.0 cm (0.78 in) diameter pin of hardened 17-4PH stainless steel located in the bolt hole farthest downstream 28 cm (11 in) from the tip). This (temporary) solution was sufficient for relatively low upper-stream plenum pressures (such as the 400 kPa (4 atm) for $M_1 = 1.5$), but the tip deflection would be unacceptable for the highest design Mach number of 3.2 (where the pressure would be approximately 5 Mpa (50 atm).

A new splitter plate (figure A.5), which keys into (and is supported by) keyways (figure A.6) fitted into the side-walls, reduces the displacement of the splitter plate. With the keys providing support to within 7.6 cm (3 in) of the splitter tip, the deflection of the tip should be less than 25 μm (0.001 in) for pressures as high as 5 MPa (50 atm) in the upper-stream plenum. The new splitter plate and keyways were manufactured by Tri-Models of Huntington Beach, California. The assembly drawing, Figure A.7, shows how the how the splitter plate, keyways and sidewall fit together.

As part of the test-section modification, windows (11.4 cm (4.5 in) by 14.0 cm (5.5 in)) were installed in the top and bottom plates of the test section. The windows are designed for spanwise schlieren. The improved optical access (Figure A.8) also simplifies the optical setup for laser diagnostics. The window openings were machined by Caltech's Central Engineering Services.

[1]It has since been replaced by a larger-volume higher-pressure vessel (Slessor 1998).

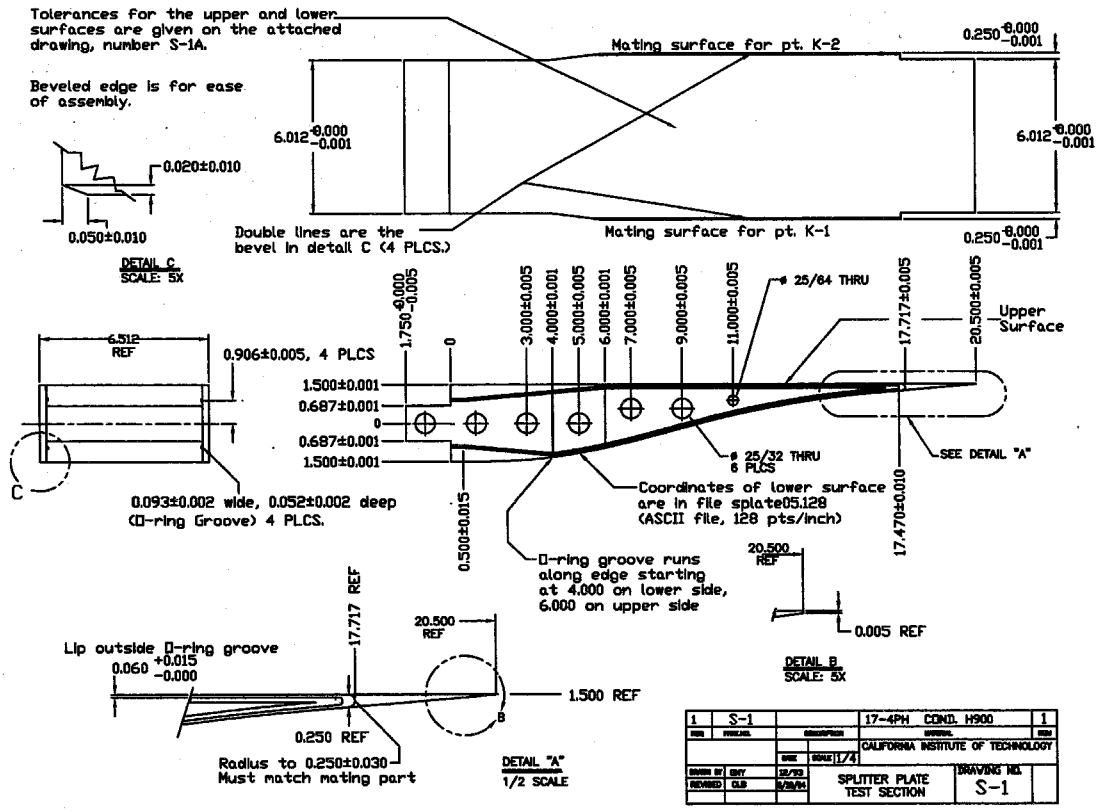

Figure A.5: Working drawing for the new splitter plate. Notice the keyed sides for structural support.

Although the instrument rakes could be translated, probe spacings were fixed. A new rake was constructed to allow variable probe spacing. The new rake carries both pressure (Pitot) and temperature (thermocouple) probes and is mounted at the centerline of the flow. The rake was constructed by the GALCIT machine shop.

While the guide-walls extend to 38 cm (15 in) downstream of the splitter plate and nozzle blocks, they end roughly 36 cm (14 in) short of the test section exit. To provide a continuous wall to the exit, a pair of guidewall extensions was employed. The extensions begin at the end of the guide-walls, wrap around the rake, and extend to the exit of the test section.

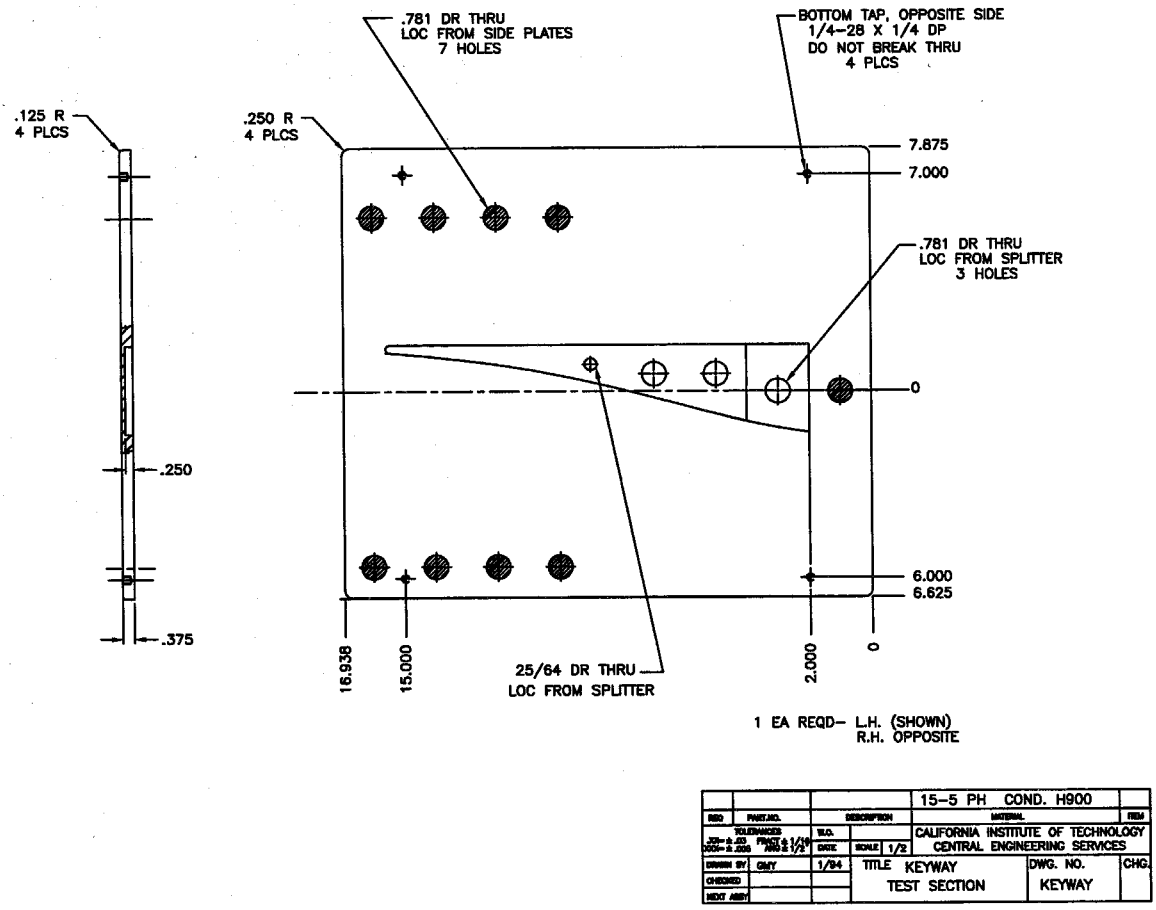

Figure A.6: Working drawing of keyway for new splitter plate.

A.3 Upper-stream gas-delivery modifications

A new burst diaphragm was installed in series with a relief valve on the reactant tank. The upper-stream reactant-tank pressure gauges have been replaced with digital pressure indicator/transducer pairs. Ports for aerosol injection/temperature measurements have been added.

The original supersonic configuration used a 10 cm (4 in) burst diaphragm. The diaphragm was replaced to remove the potential hazards of the strong shock and very high flow rates that it could have generated. An analysis of the maximum (possible) loading rate for the upper-stream reactant tank indicated that a combination of a small (1.2 cm, 0.5 in) burst diaphragm, set for 11.5 MPa (1662 psi), followed by a

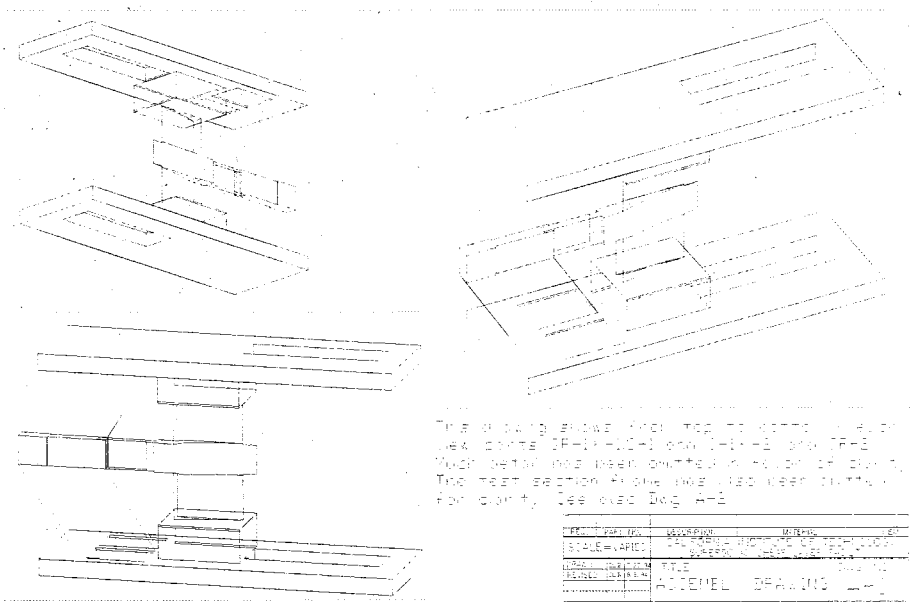

Figure A.7: Assembly drawing, showing the relation between the sidewalls, keyways, and the splitter plate.

1.9 cm (0.75 in) relief valve was sufficient. The new burst diaphragm isolates the relief valve, eliminating leaks, while the valve controls the exhaust rate and prevents the tank from completely discharging.

The original facility had two Heise pressure gauges that were used to load gases into the upper-stream reactant tank (using partial pressures to determine composition). The two gauges were attached to the upper-stream reactant tank and a vent line with a four-way valve, so that one gauge reads tank pressure and the other reads the pressure in the vent line (which, at one end, is open to the atmosphere).

The low-pressure gauge was replaced with a digital pressure indicator/transducer pair (Druck DPI 260, PDCR 920), which has a range of 0 to 1.38 MPa (0 to 200 psia), accuracy of 0.06% full scale and resolution of 69 pa (0.01 psi). The transducer is rated to 5.5 MPa (800 psia) without losing calibration, and at least 20.7 MPa (3000 psig) without bursting.

The high-pressure Heise gauge was replaced by a digital pressure indicator/ transducer pair (Druck DPI 260, PDCR 920), which has a range of 0 to 13.8 MPa (0 to

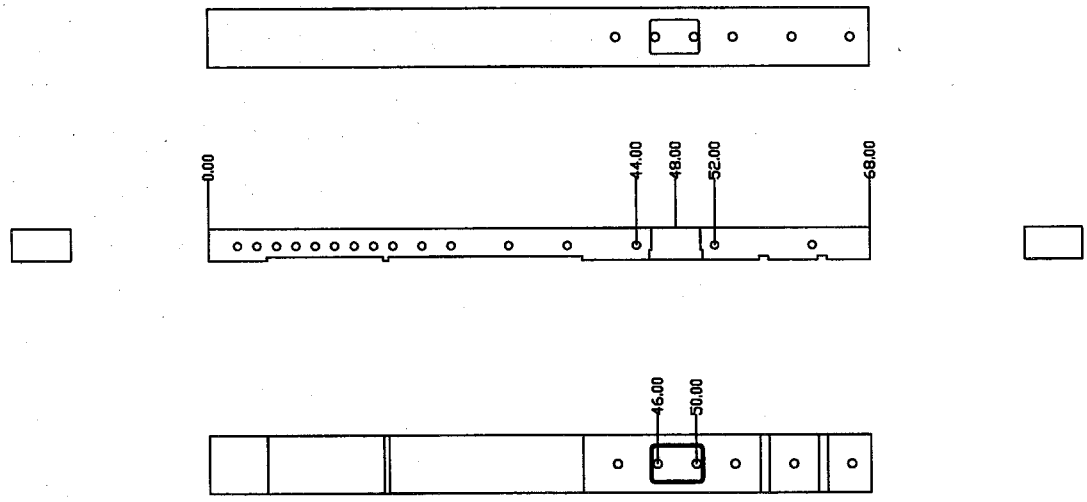

Figure A.8: Location of new windows on the top and bottom plates of the test section.

2000 psia), accuracy of 0.06% full scale, and resolution of 690 Pa (0.1 psi). The high pressure Heise gauge has been retained (now permanently connected to the tank) as a non-electronic indicator of the tank pressure.

Two 1.2 cm (0.5 in) tube fittings were welded to the upper-stream supply line immediately upstream of the test section. This section of the upper-stream supply line was hydrotested to 15.5 MPa (2250 psig) after attaching the new ports. The ports can be used to inject trace gases or to insert a thermocouple probe to measure the upper-stream stagnation pressure.

A.4 Lower-stream gas-delivery modification

A digital pressure indicator has replaced the low- and high-pressure gauges on the mixing vessel. A new metering valve insert has been made, allowing higher mass flow rates. A port has been added to the test-section inlet.

A pair of pressure gauges attached (in a manner similar to the pair on the upper-stream reactant tank) to the lower-stream mixing vessel were replaced by a single

digital pressure indicator/transducer pair (Druck DPI 261, PDCR 920). The system has a range of 0 to 500 psia, accuracy of 0.04% full scale, and resolution of 0.1 psi. This matches the absolute accuracy for the old low-pressure gauge, improves the resolution, and spans the full range of the old high-pressure gauge. The high pressure gauge has been retained as a non-electronic indicator of the mixing-vessel pressure, while the low-pressure gauge has been retained to monitor the vent-line pressure.

The lower-stream metering valve consists of a perforated cylindrical insert containing a sliding piston and a stack of perforated plates and screens on the outlet. The flow enters the valve on the outside of the insert, passes through the insert and exits through the screen stack. The sliding piston can be adjusted to set the open area of the insert. The original insert could not provide mass flow rates high enough to supply a supersonic lower stream. A new insert was designed by M. Slessor, and fabricated by the GALCIT machine shop personnel. This insert was used to generate the 170 m/s lower-stream flows.

A small 1.2 cm (1/2 in) port has been added to the lower stream at the entrance to the test section. This can be used to inject trace gases.

A.5 Exhaust-system modification

The original catch bag reached the end of its four-year (based on UV exposure) life and was replaced by a new bag. An enclosure was built to surround the catch bag. Plumbing and tanks in the shower system were replaced and a backup pump was added.

As part of the design for the new catch bag, the largest volume of gas the facility could generate (including the effects of heat release) was calculated. The volume of the catch bag (153 m^3, 5400 ft^3) is larger, ensuring that no event can overfill the bag. With the old catch bag, which had a volume of 113 m^3 (4000 ft^3), the facility had been limited to an upper-stream Mach number of 2.5 for non-reacting runs, and to an upper-stream Mach number of 1.5 for reacting runs. The new catch bag was fabricated by Kepner Plastics of Torrance, California.

As an added safety precaution, an enclosure was constructed to surround the catch bag. This enclosure is a large (5.5 m (18 ft) high, 9.9 m (32.5 ft) wide, 2.3 m (7.5 ft) deep), steel-frame, stucco-exterior structure. At the top of the enclosure, a pair of high-capacity explosion-proof axial fans draw a continuous flow of air past the catch bag and through an exhaust stack that exits ten feet above the adjacent roof. A pair of explosion-proof combustible-gas monitors (Sierra Monitor model number 201) are mounted at the top of the enclosure to alert the operator to any leak in the catch bag. The enclosure walls include fireproof fiberglass insulation, which isolates the bag from solar heating and provides acoustic attenuation.

When the enclosure was constructed, the area underneath was paved (where the shower system plumbing and tanks are), raising the ground level. This required new tanks and plumbing. The facility had PVC plumbing (rated to 60°C) and polyethylene (rated to 60°C, up to 80°C for intermittent use) tanks. Since the facility is designed to operated with a upper-stream stagnation temperature of 600°C, the sodium hydroxide/water solution could return to the tanks at a temperature close to the boiling point of water. For this reason, the new plumbing is CPVC and the new tanks are polypropylene (both rated for intermittent use to 110°C).

An air-powered pump was installed to provide a method of neutralizing the exhaust gases in the event of electrical (or pump) failure. The pump is supplied with air from either the house air system or from a cylinder of compressed air and is capable of output pressures as high as 690 kPa (100 psig) and flow rates as high as 3.8 l/s (60 gpm).

A.6 General operating modifications

A kill switch was installed to allow the operator to close both stream-shutoff valves. A compressed-air cylinder is used to actuate valves previously operated using inert-gas supplies and to provide a backup for all of the valves operated using house air. An uninterruptible power supply was added to provide power to the control panel in the event of a power failure. A warning siren alerts the occupants of the surrounding

buildings before the experiments.

After the control computer opened the shutoff valves, the only way the operator could shut the valves was to shut off the control panel. However, this would close all other open valves and shut off the shower pumps. A kill switch was added to allow the operator to close the shutoff valves (and the six-inch valve) without turning off the control panel. The valve-enable button on the control panel activates a self-energizing relay. The relay connects the panel switches and the computer control outputs to the valve actuators, allowing operation of the shutoff valves (and the six-inch valve). The operator can close the valves by pushing the kill switch which opens the circuit.

The upper-stream shutoff valve is operated pneumatically using gas stored at 1.0 MPa (150 psig) in a 0.11 m^3 (30 gallon) receiver. The receiver previously had been filled using gas from the upper-stream inert manifold since the house-air pressure was too low. With the compressed-air cylinder available for the air-powered pump, it was possible to decouple the receiver from the inert-gas supply and instead fill it with compressed air. A number of other pneumatically-actuated valves that required pressures greater than 690 kPa (100 psig) had been actuated using compressed gas from the lower-stream inert-gas regulator. By using the compressed-air cylinder to operate these valves, these valves operated independently from the lower-stream inert-gas supply. Finally, the compressed-air cylinder was used to provide a backup air source for all of the house-air actuated valves.

Although the air-powered pump provides an alternative method for neutralizing the exhaust, a failure of power to the control panel would shut the shower system valves, stopping flow of the NaOH/water solution to the shower heads and the flow of compressed air to the pump. By providing a uninterruptible power supply for the control panel, all of these valves will still operate.

Before the construction of the catch-bag enclosure, the sound level outside of the lab had been measured (for some flows with a upper-stream Mach number of 2.5) at over 100 dB. As the experiments are very short, the sudden loud disturbance was unacceptable. To warn people that an experiment was imminent, a warning siren was installed and is now sounded shortly before each experiment.

Appendix B Data processing and analysis

The results presented in this thesis consist mostly of temperature-rise data with pressure measurements and schlieren photography as supporting measurements.

B.1 Temperature measurements and mixing measures

The time-series from each experiment is examined to find where the flow was steady (to eliminate the start-up transients), and the temperatures over this steady-flow period were averaged. The non-reacting flow temperatures are used to construct a mean temperature profile for each flow condition, and this mean temperature profile is subtracted from the reacting-flow mean temperatures. The resulting temperature rise measurements are then divided by the adiabatic flame temperature rise, ΔT_{f}, providing the normalized mean temperature rise measurements. These measurements are then fit with

$$\Theta(y) = \frac{\Delta T_y}{\Delta T_f} = \exp\left[-P(y)\right], \tag{B.1}$$

where $P(y)$ is a sixth-order polynomial

$$P(y) = P_0 + P_1 y + P_2 y^2 + P_3 y^3 + P_4 y^4 + P_5 y^5 + P_6 y^6. \tag{B.2}$$

The temperature thickness of the shear-layer is determined by locating the two 1% points y_+ and y_-,

$$\Theta(y_+) = \Theta(y_-) = 0.01\Theta_{\max} \text{ and } y_+ > y_- , \tag{B.3}$$

where $\Theta_{max} = \max[\Theta(y)]$ and the temperature thickness, δ_T, is

$$\delta_T = y_+ - y_- . \tag{B.4}$$

The temperature thicknesses are normalized by the distance x downstream from the trailing edge of the splitter plate. The reference position, y_0 is defined as,

$$y_0 \equiv (y_+ + y_-)/2 . \tag{B.5}$$

All of the temperature and velocity measurements will be plotted versus $(y - y_0)/\delta_T$ where δ_T is the 1% temperature thickness. This choice was made, as y-positions fixed relative to the facility do not reflect the changes in guidewall angle, shear-layer displacement thickness, and shear layer entrainment.

The product thickness is defined as,

$$\delta_p = \int_{-\infty}^{+\infty} \Theta(y) dy, \tag{B.6}$$

(Dimotakis 1987). The product thickness is the thickness of the equivalent layer that contains only reacted fluid. Product thicknesses are normalized using the downstream distance x as is the temperature thickness.

The product fraction is obtained by calculating the product thickness and dividing by the 1% temperature-rise thickness, δ_T. The product fraction is the ratio of reacted fluid to all fluid in the shear layer. This measure is insensitive to the overall growth rate.

Given the product fraction at two ϕ's, ϕ_1 and $\phi_2 = 1/\phi_1$, the mixed-fluid fraction can be calculated as (Dimotakis 1991)

$$\frac{\delta_m}{\delta_T} = \frac{1}{1+\phi_0} \left(\left.\frac{\delta_p}{\delta_T}\right|_{\phi_0} + \left.\frac{\delta_p}{\delta_T}\right|_{1/\phi_0} \right) , \tag{B.7}$$

where ϕ_0 is the smaller of ϕ_1 and ϕ_2. The mixed fluid fraction is the volume fraction of the fluid in the layer that is mixed on the molecular scale.

A number mixed-fluid composition ratio can be calculated as

$$\mathcal{E}_{\mathrm{n}} = \frac{(\delta_p/\delta_t)_{\phi=8}}{(\delta_p/\delta_t)_{\phi=1/8}} . \tag{B.8}$$

This is the number of moles of high-speed fluid needed for each mole of low-speed fluid mixture to create a single-composition mixture that would have the same ratio of product formation as observed in the shear layer. To the extent that the shear-layer mimics the "balloon reactor" model, this would be the number entrainment ratio needed to produce the observed results.

Given a number mixed-fluid composition ratio, the corresponding volumetric ratio can be calculated. For equal temperature free-streams, the volumetric mixed-fluid composition ratio is identical to the number mixed-fluid composition ratio. For differing free-stream temperatures, a correction must be made for the differing free-stream number density, giving

$$\mathcal{E}_{\mathrm{v}} = s_{\mathrm{n}}\mathcal{E}_{\mathrm{n}} , \tag{B.9}$$

where $s_{\mathrm{n}} = n_2/n_1$ is the free-stream number density ratio, and n_i is the number density of the ith free-stream.

The results of the current investigation are compared with the previous results from Mungal & Dimotakis (1984), Mungal *et al.* (1985) and Frieler (1992). Results from the Mungal & Dimotakis (1984) and Mungal *et al.* (1985) studies were converted to the above measures (which are based on both stream compositions) from the original product measures (which were based on only one free-stream composition).

B.2 Schlieren visualization

Schlieren images provide a time-resolved view of the large scale organization and a view of the near-splitter plate flow. The schlieren images (with a 20 ns exposure) provide the only time-resolved data in these investigations. These images can be used to check for flow distortion caused by forcing. The upstream photographs are used to look at the near splitter-plate flow.

B.3 Velocity profiles (subsonic experiments)

Velocity calculations were performed for two purposes, to provide free-stream velocities to measure the actual velocity ratio, and to provide an additional measure of the shear-layer width and center. The velocity was calculated from the Pitot pressure measurements as,

$$U = \sqrt{2\left(\frac{P_p - P_g}{\rho}\right)}, \tag{B.10}$$

where P_p is the Pitot probe pressure measurement, P_g is the guidewall pressure measurement and ρ is the density. The density is estimated

$$\frac{\rho}{\rho_0} = \frac{T_0}{T_0 + \Delta T} \tag{B.11}$$

using the average temperature rise for the y-location of the Pitot probe, the ambient temperature T_0, and the density ρ_0 at the ambient conditions. The free-stream velocities, U_1 and U_2, are derived from Pitot measurements in the freestreams.

The resultant profile is fitted with a modified hyperbolic tangent profile,

$$U(y) = \frac{(U_1 + U_2)}{2} + \frac{(U_1 - U_2)}{2}\tanh[Q(y - y_c)]\,. \tag{B.12}$$

U_1 and U_2 are, respectively, the high-speed and low-speed free-stream velocities and y_c is the center (half-height) of the velocity profile. $Q(y)$ is given by

$$Q(y) = \frac{2}{\delta_\omega}(y + \beta y^3)\,, \tag{B.13}$$

where δ_ω is the vorticity thickness, and β is the deviation of the profile from the simple hyperbolic tangent. The values of U_1 and U_2 are fit to the freestream measurements, while the values of y_c, δ_ω, and β are fit to the full set of velocity measurements, subject to the additional constraint

$$\beta \leq \frac{4}{3\delta_\omega^2}\,. \tag{B.14}$$

For values of β greater than this, the parameter δ_ω in Eq. B.13 would not be the vorticity thickness of the fit profile, but merely the layer thickness based on the slope at the half-height point. This constraint only affected four of the 28 velocity profile fits.

B.4 Reynolds number

The object of the present study is an investigation of Reynolds number effects. The Reynolds number, defined here as,

$$Re = \frac{\rho \, \Delta U L}{\mu} , \tag{B.15}$$

as the parameter of whose effects are being investigated, must be carefully determined. The length scale, L, and the free-stream velocity difference,

$$\Delta U = U_1 - U_2 , \tag{B.16}$$

are subject to direct measurement. The determination of the appropriate density, ρ, and viscosity, μ, is more complicated.

In presenting the results, two estimates of L are used: the distance, x, from the splitter-plate trailing edge to the rake position is used in presentation of shear-layer temperature thicknesses (δ_{T} and δ_{P}), the 1% temperature thickness, δ_{T}, is used in presentation of the product and mixed-fluid fractions. Although the Reynolds number based on the local shear-layer thickness (here represented by the 1% temperature thickness, δ_{T}), $Re_{\delta_{\mathrm{T}}}$, is the appropriate measure of the local shear and viscous effects, the Reynolds number based on x is used where the use of $Re_{\delta_{\mathrm{T}}}$ would effectively include δ_{T} on both axes of a plot.

The velocity difference, ΔU is computed from the free-stream Pitot measurements, as described above.

The viscosity and density were calculated from a mixture composition and temperature. For the current cases, temperature and composition were computed by

recovering the free-stream kinetic energy in the isentropic convection frame, with the number entrainment ratio determined by the our measured values of the number entrainment ratio. The composition is given by

$$X_{i,\mathrm{m}} = \frac{E_n X_{i,1} + X_{i,2}}{E_n + 1}, \tag{B.17}$$

where $X_{i,\mathrm{m}}$ is the mixture mole fraction of the ith species, $X_{i,1}$ is the upper-stream mole fraction ith species, $X_{i,2}$ is the lower-stream mole fraction of the ith species, and E_n is the assumed number entrainment ratio. The number (molar) entrainment ratio is the number of moles entrained from the high-speed stream for each mole entrained from the low-speed stream. The mixture enthalpy, which determines the temperature, is given by

$$\tilde{h}_\mathrm{m} = \frac{E_n(\tilde{h}_1 + \mathcal{M}_1(U_1 - U_\mathrm{c})^2/2) + \tilde{h}_2 + \mathcal{M}_2(U_\mathrm{c} - U_2)^2/2}{E_n + 1}, \tag{B.18}$$

where $\tilde{h}_\mathrm{m}$ is the molar enthalpy of the mixture, $\tilde{h}_1$ and $\tilde{h}_2$ are the free-stream molar enthalpies, and $\mathcal{M}_1$ and $\mathcal{M}_2$ are the molecular masses (weights) of the two free-stream mixtures. The enthalpies are calculated using the CHEMKIN-II package (Kee *et al.* 1989) which uses fourth-order polynomial fits to the species specific heats at constant pressure. Integration of this polynomial with the addition of the species heat of formation gives the enthalpy as a function of temperature. Once the mixture enthalpy and composition are calculated using equations B.18 and B.17, the mixture temperature is found by determining the temperature required to give the mixture the appropriate enthalpy.

The non-reacted mixture properties were chosen (as the basis for the Reynolds number calculation) because of evidence that strained flame reactions are much less important at the high local strain rates present in these flows (Egolfopoulos *et al.* 1996). This assumption of a two-stage process of mixing, with turbulent mixing feeding the chemical reaction, is implicit in the "Balloon" reactor model.

The calculation of the viscosity, μ, is dependent upon temperature, pressure and

composition. For these calculations, gas-mixture viscosities were calculated using a FORTRAN code for evaluation of gas-phase viscosities (Kee *et al.* 1990). The specific routine used calculates the mixture viscosity from the mixture composition and temperature using

$$\mu = \sum_{k=1}^{K} \frac{X_k \mu_k}{\sum_{j=1}^{K} X_j \Phi_{kj}} , \tag{B.19}$$

where K is the number of species, X_i are the species mole fractions, μ_i are the pure-species viscosities, and Φ_{jk} are given by,

$$\Phi_{jk} = \frac{1}{\sqrt{8}} \left(1 + \frac{\mathcal{M}_k}{\mathcal{M}_j}\right)^{-\frac{1}{2}} \left[1 + \sqrt{\frac{\mu_k}{\mu_j}} \left(\frac{\mathcal{M}_j}{\mathcal{M}_k}\right)^{\frac{1}{4}}\right]^2 , \tag{B.20}$$

where $\mathcal{M}_i$ is the species molecular mass (weight).

The density is calculated using the ideal-gas law, with the mixture pressure, molecular mass, and temperature. The mixture pressure is determined from the guidewall pressure measurements.

Since changes in both density and viscosity change the Reynolds number, the effects of composition and temperature on kinematic viscosity,

$$\nu = \frac{\mu}{\rho} , \tag{B.21}$$

are calculated to determine the sensitivity of the results on the model assumptions made above.

The mixture composition has weak leverage on the Reynolds number. For the lowest two Reynolds numbers, where the two free-stream base compositions are identical, the only change with composition is due to the introduction of reactants. Even then, replacing 16% of upper free-stream He with 16% H_2 raises the *free-stream* kinematic viscosity, ν, by less than 2%. Replacing lower free-stream Ar with F_2 lowers the *free-stream* kinematic viscosity, ν, less than 1%. In both cases, more than two-thirds of that change is because of the resulting change in density.

However, temperature effects on ν are quite strong (although, again, nearly two-

thirds are due to density change). For any of the mixtures used in the current experiments, a 1% change in ν could be caused by a change in temperature of less than 1.5 K. Since, at the higher Reynolds number, the free-stream temperatures differ by 18 K, some model must be used to determine which is the appropriate temperature.

The number entrainment ratio becomes important (in these cases) because this ratio can affect the temperature of the resulting mixture. For the higher Reynolds number case, changing E_n from 0.9 to 1.5 changes the resultant temperature by 3 K, which would be a greater than 2% change in ν. For the lower Reynolds number, this effect is significantly smaller.

The estimates of the Reynolds number used in the current study are insensitive to the mixture composition assumed, with the major uncertainty due to the temperature of the mixture. Even with this possible variation, for a reasonable range of assumed entrainment ratios, the variation is less than 10%.

In comparison, the Reynolds numbers for the previous subsonic reacting-flow experiments were based on the ambient temperature N_2 properties. This was the appropriate temperature, as the lower velocities did not much alter the static temperatures.

Appendix C Detailed experimental results

The experiments documented here were conducted at two nominal flow conditions, with a total of four non-reacting and nine reacting conditions.

Condition	HSS	U_1	U_2	X_{H_2}	X_{NO}	X_{F_2}	ϕ	comments
1c	upper	100	40	—	—	—	—	cold run (T ref.)
1h				0.16	0.01	0.0206	1/8	
1f				0.0097	0.0006	0.08	8	
2c	lower			—	—	—	—	cold run
2h				0.16	0.01	0.0206	8	poor repeat
2f				0.0097	0.0006	0.08	1/8	
3c	upper	165	65	—	—	—	—	cold run
3h				0.16	0.01	0.0206	1/8	
3hk				0.16	0.008	0.0205	1/8	kinetics test
3f				0.0097	0.0006	0.08	8	
4c	lower			—	—	—	—	cold run
4h				0.16	0.01	0.0206	8	flapping flow
4f				0.0097	0.0006	0.08	1/8	

Table C.1: Table of Subsonic Flow conditions (HSS = High Speed Side)

This appendix presents measurements using certain conventions. For all of the temperature and velocity profiles, the high-speed stream will be to the right of the figure. The reacting-run profiles will be scaled by the 1% temperature thickness, δ_T, and centered so the 1% (of maximum temperature rise) points line up. The non-reacting runs are centered at the half-height point of the fitted velocity profile. The measures used and their derivation are explained in Appendix B.

It should be noted that the value of the velocity profile fits are limited. An examination of the data suggests that the current fit to the data is too simple, but the number of data points in the velocity profiles is too low for more complex fits. In fact, the current fits have enough free parameters to cause difficulties with some of the

runs. For completeness, the velocity profiles and the resultant vorticity thicknesses, δ_ω, are included.

C.1 Lower Reynolds number: Cases 1 and 2

The lower Reynolds number case is a flow of nominal density ratio, $s = 1.0$, nominal velocity ratio, $r = 0.4$, and with a nominal high-speed stream velocity of 100 m/s.

C.1.1 Upper (H_2) stream fast: Case 1

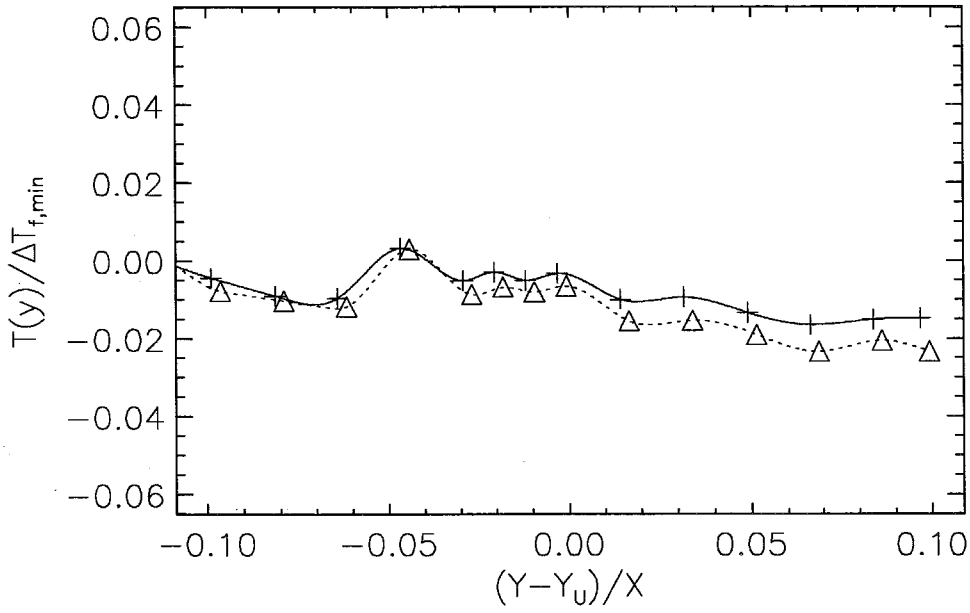

Figure C.1: Measured temperature profile, Case 1c (non-reacting flow). Temperature is normalized by the minimum adiabatic flame temperature rise usedin the current study. Upper stream is high-speed. Solid line/crosses: Run 685, Dotted line/triangles: Run 686. Lines are spline fits to data.

This condition comes closest to the highest Reynolds number cases performed by Mungal *et al.* (1985) and Frieler (1992). The velocities are somewhat higher (100 m/s *vs.* 83 m/s), but the test cell of the current facility is somewhat smaller. These flows,

Figure C.2: Schlieren photograph of Case 1c flow. For contrast, a mixture of C_2H_4, He and Ar was used on the upper stream to replace N_2.

with the lower-stream velocity of 40 m/s, had run times of approximately 4 s, resulting in the largest collections of photographs and the longest averaging times in this study.

Figure C.2 is a schlieren photograph of a Case 1c flow. For this photograph, a "synthetic N_2" mixture replaced the N_2 in the flow. The "synthetic N_2" is a mixture of C_2H_4, He and Ar ($X_{He} = 0.238$, $X_{Ar} = 0.476$, $X_{C_2H_4} = 0.286$) with the same molecular weight and ratio of specific heats (γ) as N_2. By using this mixture, schlieren images can be acquired where the contrast would otherwise be too low. Notice that the two guidewalls (the black straight edges at the top and bottom of the picture) are converged. This convergence supplies the entrainment requirements (negative displacement thickness) of the shear layer.

The temperature profiles for this case are shown in Figure C.1, along with the spline fits. Spline fits were used to provide a reference temperature for y-positions not occupied by data points, since no simple fit to the curve could be made. The profiles are normalized by the lower of the two adiabatic flame temperature rises used in this study to provide a reference to the reader.

The velocity profiles (Figure C.3) match very well; both the fits and the data points indicate little change between runs. However, the fit does not quite capture

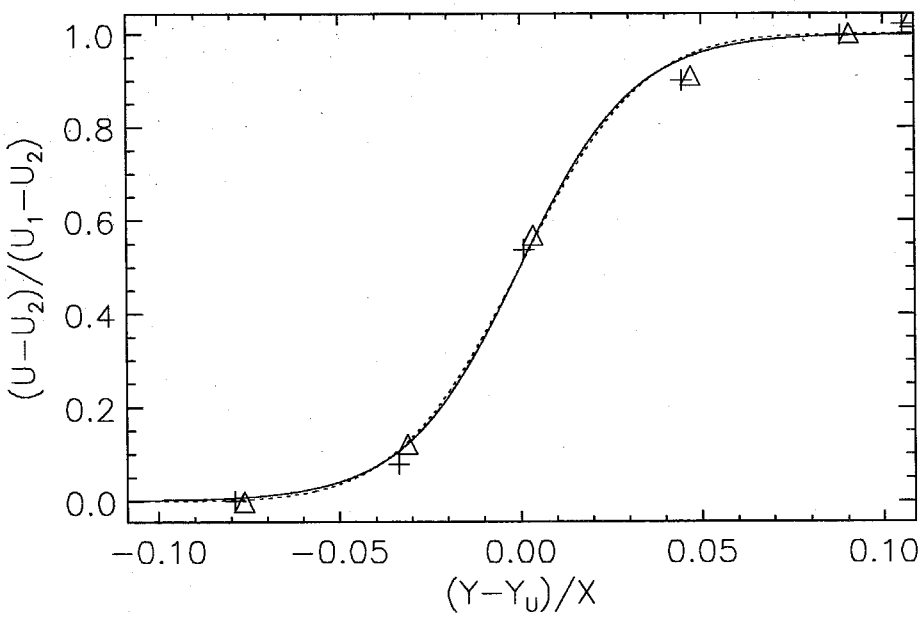

Figure C.3: The normalized velocity profiles for the Case 1c (non-reacting) flows. Solid line/crosses: Run 685, dotted line/triangles: Run 686.

the velocity profile, as evidenced by the points under the curve as it approaches the high-speed stream ($+y$). The number of points available for the fit does not allow for more complexity in the fitting function.

The Case 1h experiments differ from the previous work by having an adiabatic flame temperature, $\Delta T_{\mathrm{f}} = 354.6\,\mathrm{K}$, which is nearly twice that used in the Mungal *et al.* (1985) and Frieler (1992) experiments. Based on the results of Hermanson & Dimotakis (1989), the overall growth rate, as represented by the temperature thickness, δ_{T}, would be expected to decrease slightly, but the actual effect on product fraction is weak.

Figures C.4 and C.6 are schlieren photographs of two Case 1h flows. Notice that the guidewalls are diverged, since with the increased heat release (dilatation), the shear layer now has a positive displacement thickness. Throughout the subsonic experiments in this thesis, the guidewalls were adjusted by using the fit (for displacement thickness versus heat release) of Hermanson & Dimotakis (1989).

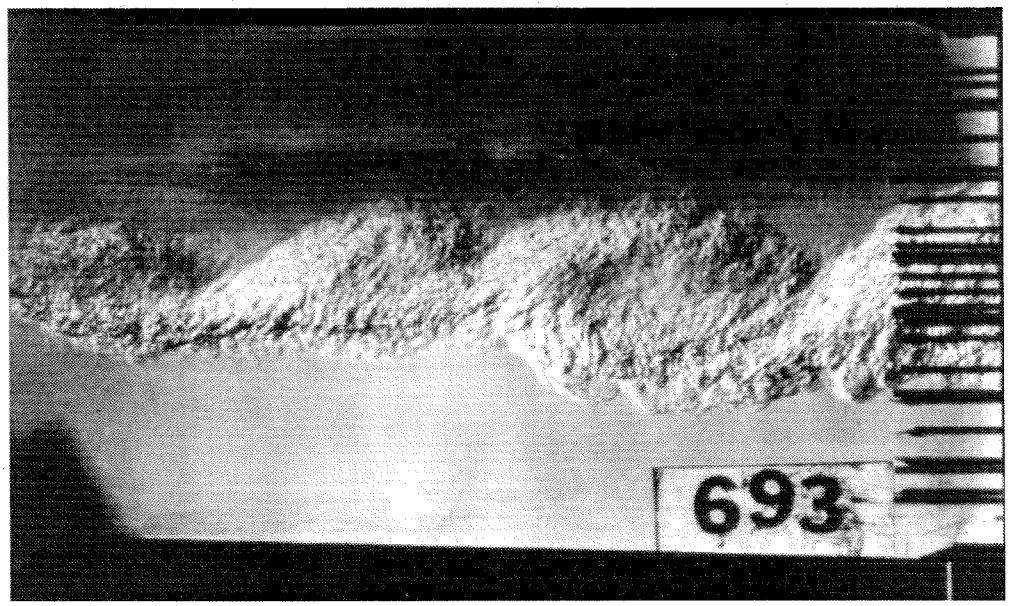

Figure C.4: Schlieren photograph of Case 1h flow (Run 693). Upper stream is high-speed reactant-rich ($\phi = 1/8$).

The temperature profiles, shown in Figure C.5, match reasonably well, suggesting that the flow is stable and the results repeatable. Despite this, the third run, 697, has a significantly thinner (10%) temperature thickness, although this appears to be a function of the fit, as the data points show no obvious difference. Notably, the product thickness, δ_{p}, which is an integral thickness (and not so sensitive to the edge behavior of the fits) is nearly constant across the three experiments. Still, the thinner temperature thickness results in a correspondingly higher product fraction, $\delta_{\mathrm{p}}/\delta_{\mathrm{T}}$, for Run 697.

Unlike previous gas-phase results, these temperature profiles do not lean towards the reactant-rich freestream. In the current case, the high-speed stream (towards $+y$) is the reactant rich stream, but the profiles seem almost symmetric.

The velocity profiles, shown in Figure C.7, vary somewhat, although the data suggest that the large span in vorticity thicknesses could be a result of the limited sampling across the layer (8 pressures, at least 2 in each freestream) of the rake Pitot pressures.

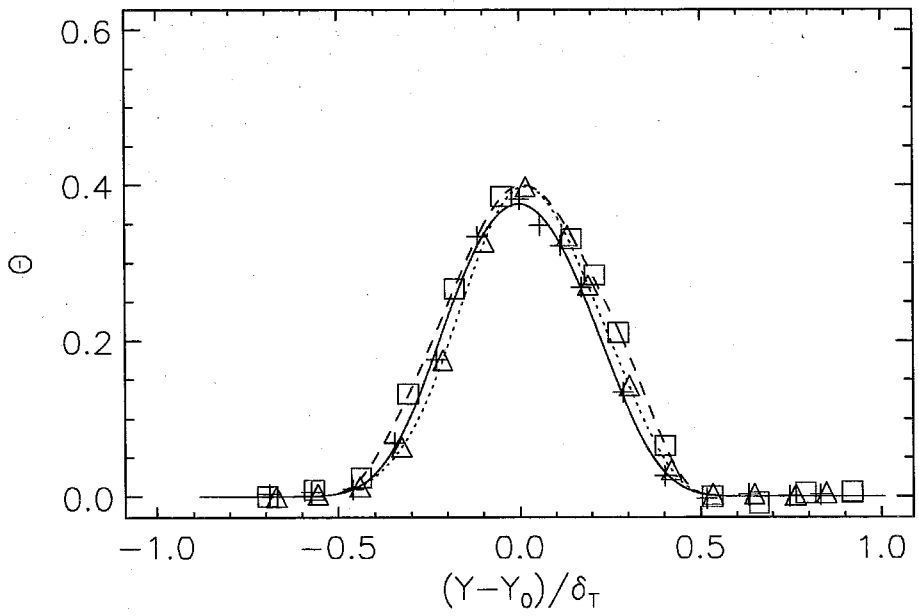

Figure C.5: Normalized temperature rise profiles for Case 1h flow. Solid line/crosses: Run 693, dotted line/triangles: Run 695, dashed lines/boxes: Run 697.

These measured run conditions, the derived shear-layer thicknesses and the product fraction are shown in the two tables at the end of the appendix, Table C.6 and Table C.7.

The Case 1f experiments, with 8% F_2 in the lower stream, and 0.97% H_2 and 0.06% NO in the upper stream, have an adiabatic flame temperature, ΔT of 171.3 K. This is very close to the values of adiabatic flame temperature from previous chemical-reacting investigations (Mungal *et al.* 1985, Frieler 1992).As such, the temperature thickness and product thickness can be directly compared to these previous results.

Figures C.8 and C.10 show schlieren photographs of the two runs at this condition. The guidewalls for these experiments are diverged, but less than for the Case 1h flows. For the flows documented in this appendix, there are three guidewall positions, one for non-reacting flow, one for $\Delta T_f = 173$ K, and one for $\Delta T_f = 354$ K.

As can be seen by the temperature profiles (Figure C.9) and velocity profiles (Figure C.11), the results repeat closely, despite the slight changes in velocity ratio, and

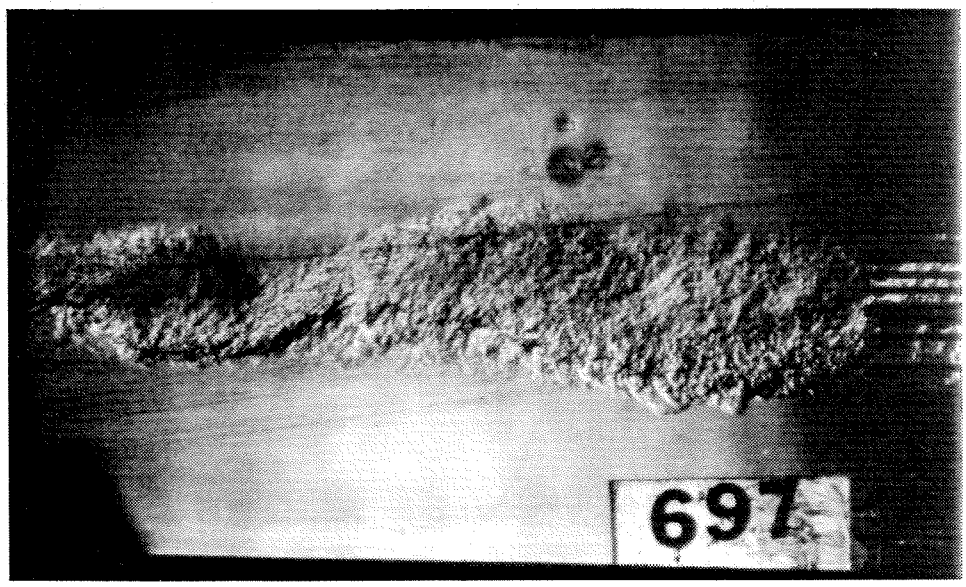

Figure C.6: Schlieren photograph of Case 1h flow (Run 697). Upper stream is high-speed, reactant-rich ($\phi = 1/8$).

the changes in overall velocity. In fact, since both profiles velocity and temperature profiles are shifted in the same direction, the shift may be an effect of a slight difference in the temperature fits at the edges of the shear layer (since the profiles are centered on the 1% points of the $\Theta(y)$ profiles..

These measured run conditions, the derived shear-layer thicknesses and the product fraction are shown in the two tables at the end of the appendix, Table C.6 and Table C.7. Overall the results of the two runs are quite similar, with both the temperature and product thicknesses changing less than 10%.

C.1.2 Lower (F_2) stream fast: Case 2

As discussed in Chapter 3, the facility is designed for the upper stream as the high-speed stream. Operating the facility with the upper stream at a velocity of 40 m/s is the most difficult of the conditions, because of the control system characteristics. Additionally, the lower stream enters the test cell at a 5° angle to the upper guidewall, which is held fixed (and parallel) for all conditions. This results in a prompt change

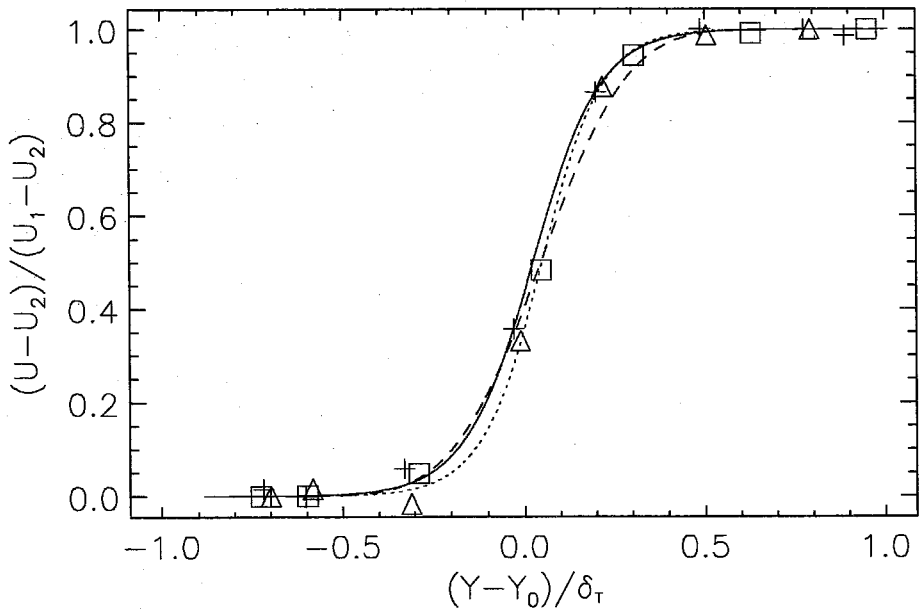

Figure C.7: Normalized velocity profiles for Case 1h flows. Solid line/crosses: Run 693, dotted line/triangles: Run 695, dashed lines/boxes: Run 697.

in the direction of the lower stream, and a curvature of the shear layer in the vicinity of the splitter plate. Since the reacting flows have positive displacement thicknesses, requiring the lower guidewall to be diverged, this turning angle can exceed the 5° needed to turn the flow parallel to the upper guidewall.

The temperature profile is shown in Figure C.12. The temperature is normalized by the lowest adiabatic flame temperature rise used in this study. The velocity profile is shown in Figure C.14. Figure C.13 shows a schlieren photograph of the cold run. As with the Case 1c flow, "synthetic N_2" was used to enhance the contrast.

Case 2h flow was variable and not completely repeatable. Figures C.15 and C.16 show two schlieren photographs from the same run, one of which has captured obvious large scale structures, and the other which has captured little large scale structure organization. Additional photographs from two other runs are shown in Figures C.17 and C.19.Note that the temperature profiles (Figure C.18) of these three runs (692, 696, and 699) are all different. Only the pair of Runs 699 and 701 come close to

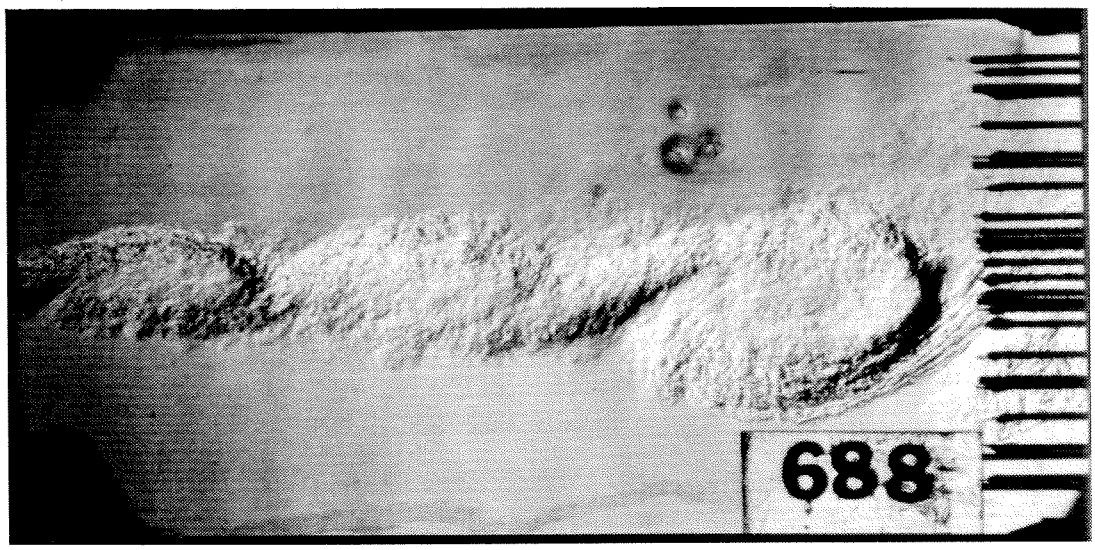

Figure C.8: Schlieren photograph of Case 1f flow (Run 688). Upper stream is high-speed, reactant-lean ($\phi = 8$).

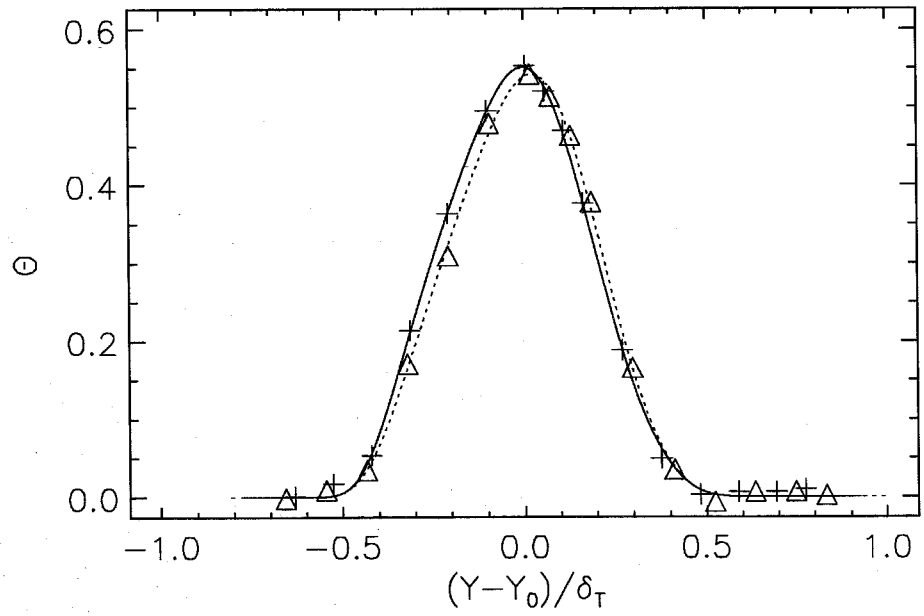

Figure C.9: Normalized temperature-rise profiles for Case 1f flows. Solid line/crosses: Run 688, dotted line/triangles: Run 691.

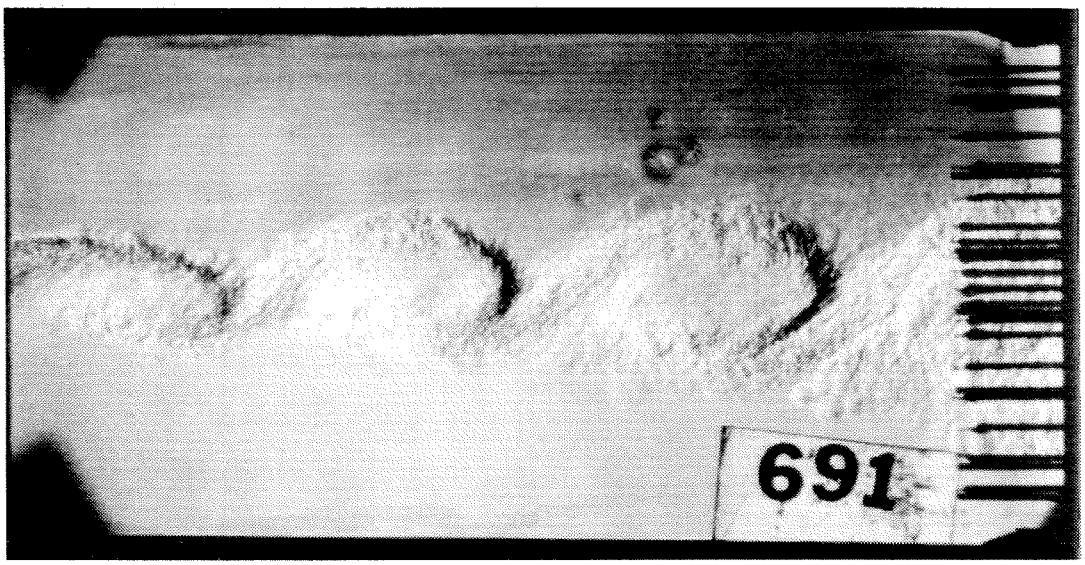

Figure C.10: Schlieren photograph of Case 1f flow (Run 691). Upper stream is high-speed, reactant lean ($\phi = 8$).

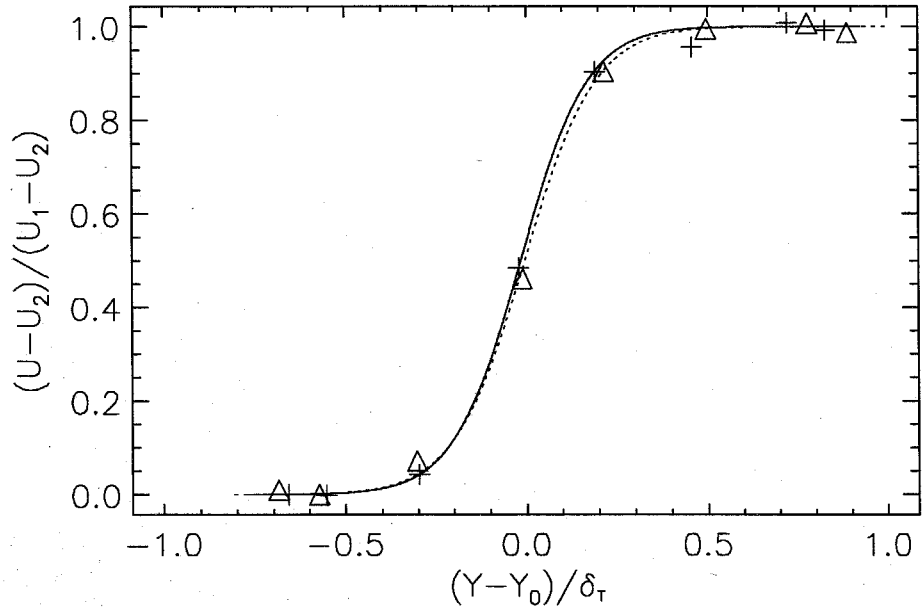

Figure C.11: Normalized velocity profiles for Case 1f flows. Solid line/crosses: Run 688, dotted line/triangles: Run 691.

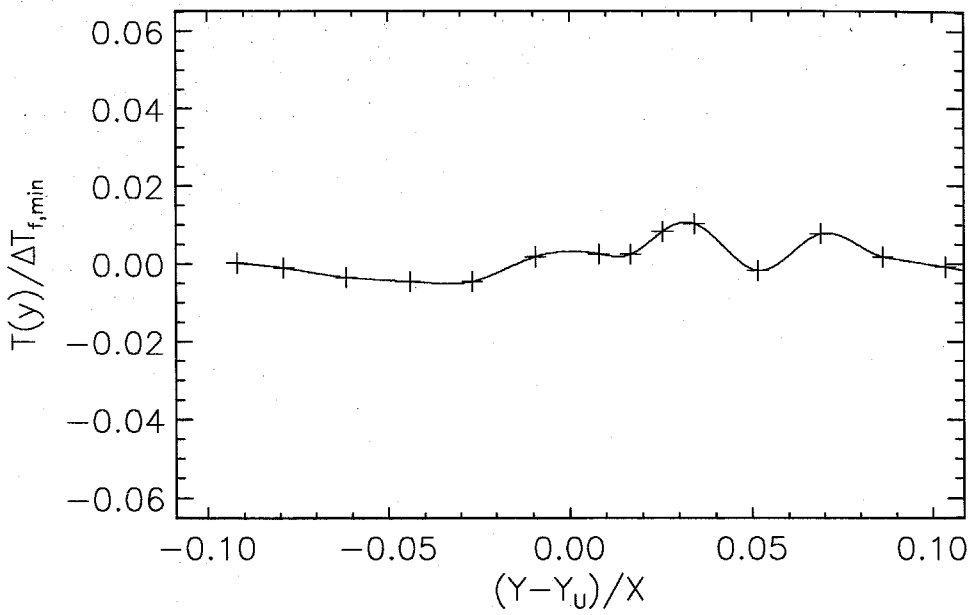

Figure C.12: Temperature profile, case 2c (Run 684). Temperature is normalized by the minimum adiabatic flame temperature rise used in the current study.

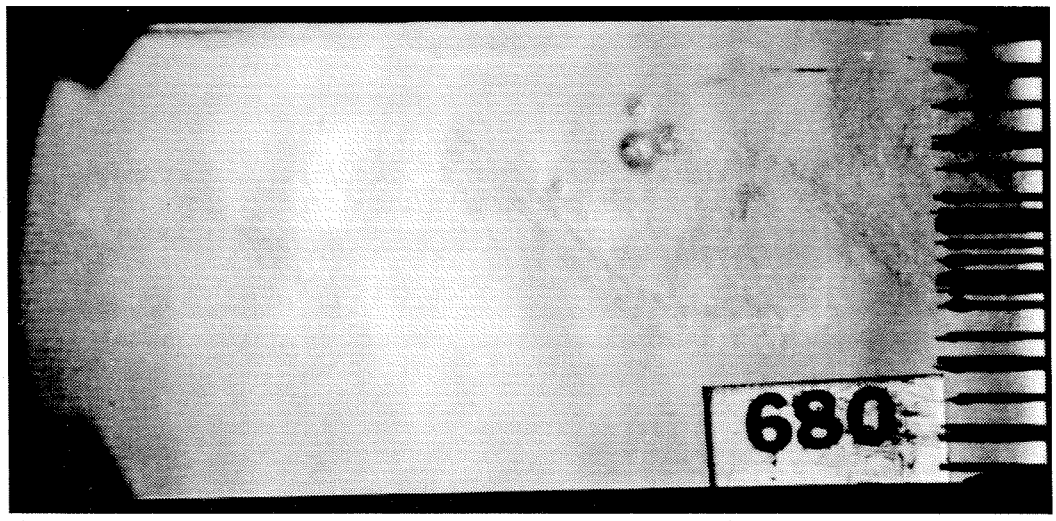

Figure C.13: Schlieren photograph of Case 2c flow. As with Figure C.13, this case used "synthetic N_2" to enhance the contrast. Upper stream is low-speed stream.

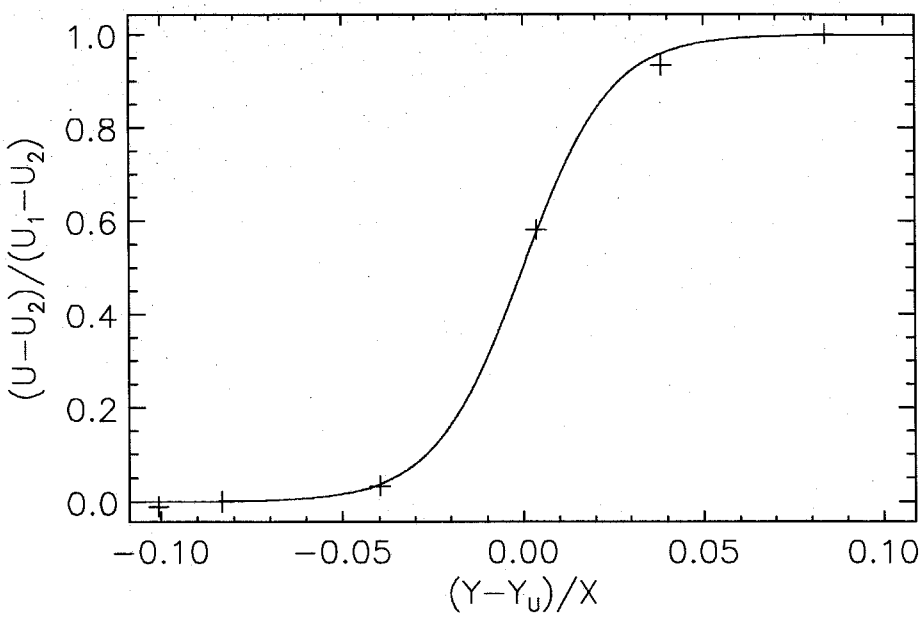

Figure C.14: Normalized velocity profile of Case 2c (Run 684) non-reacting flow.

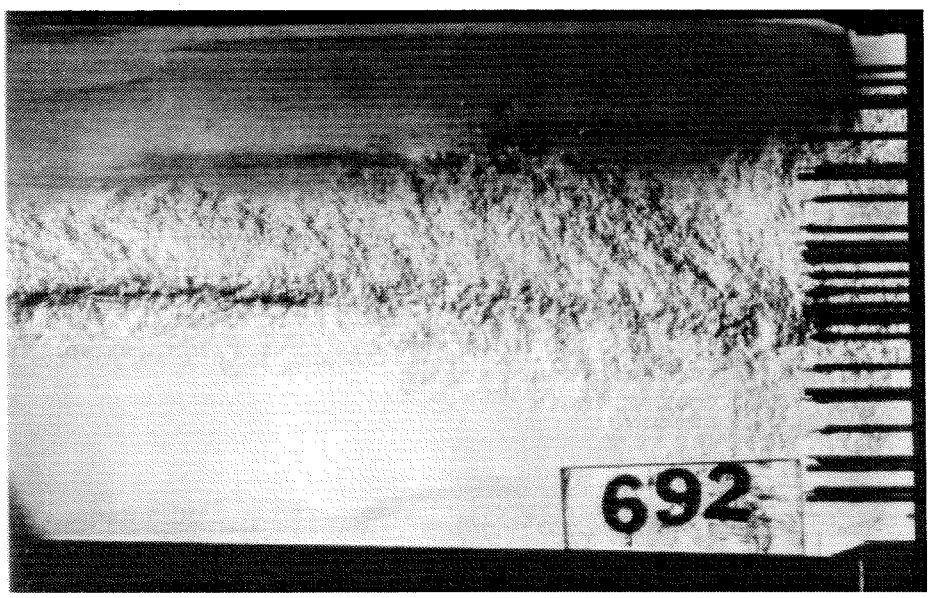

Figure C.15: Schlieren photograph of a Case 2h flow (Run 692). Upper stream is low-speed, reactant-rich ($\phi = 8$). This photograph show little large-scale structure.

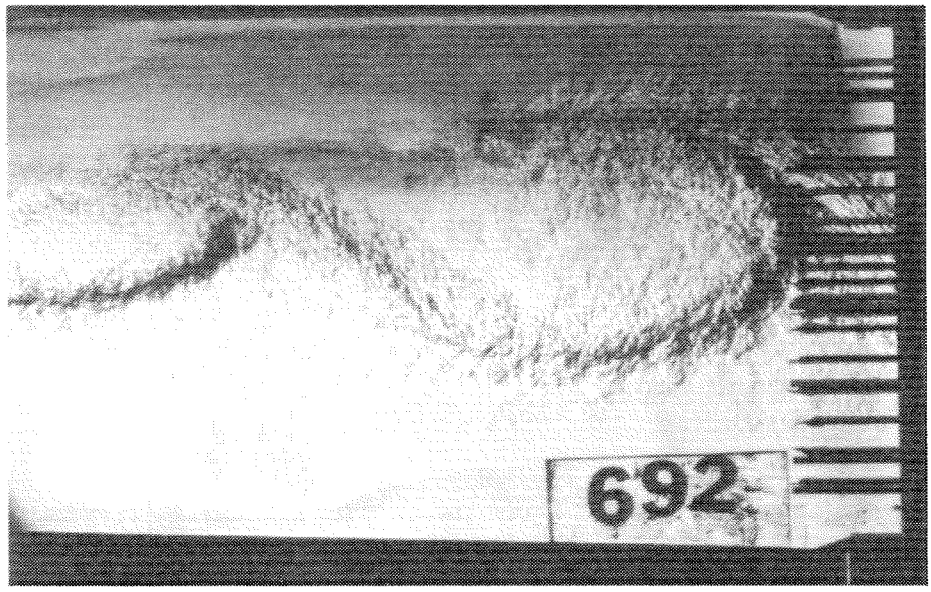

Figure C.16: Schlieren photograph of Case 2h flow (Run 692). Upper stream is low-speed, reactant-rich ($\phi = 8$). This photograph shows large-scale, two-dimensional structure.

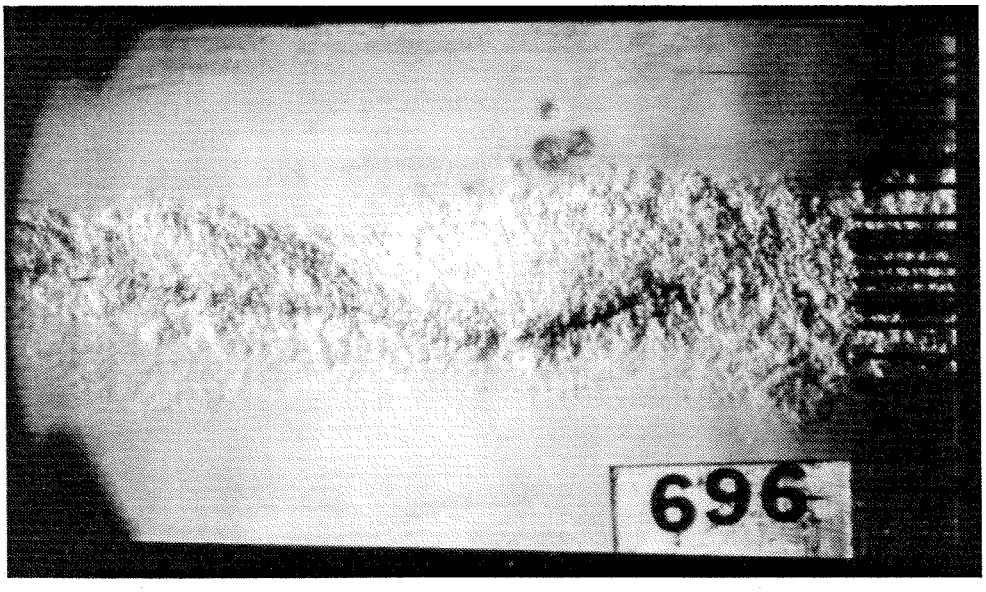

Figure C.17: Schlieren photograph of Case 2h (Run 696). Upper stream is low-speed, reactant rich ($\phi = 8$).

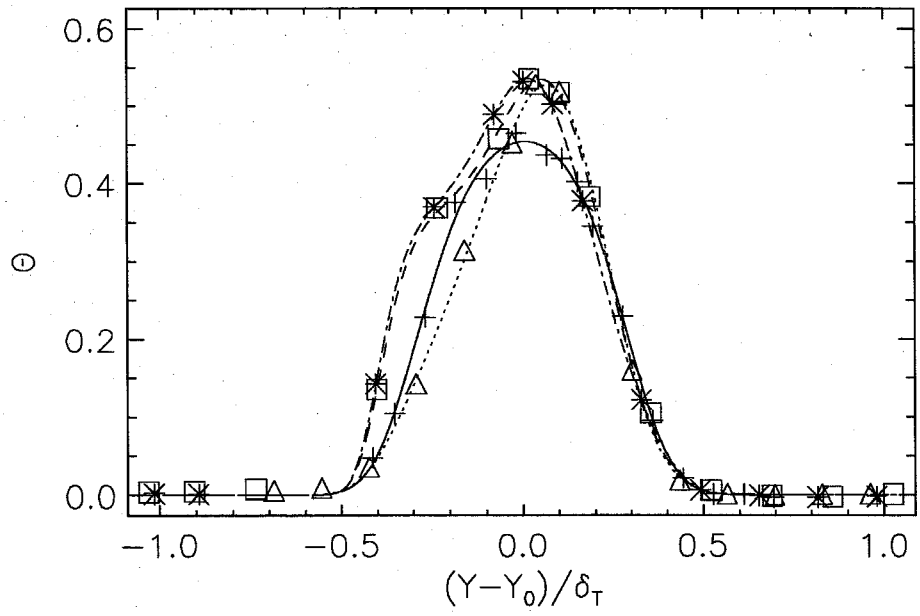

Figure C.18: Normalized temperature-rise profiles for Case 2h. Solid line/crosses: Run 692, dotted line/triangles: Run 696, dashed line/boxes: Run 699, dot-dashed line/stars: Run 701. Note the three distinct profile shapes.

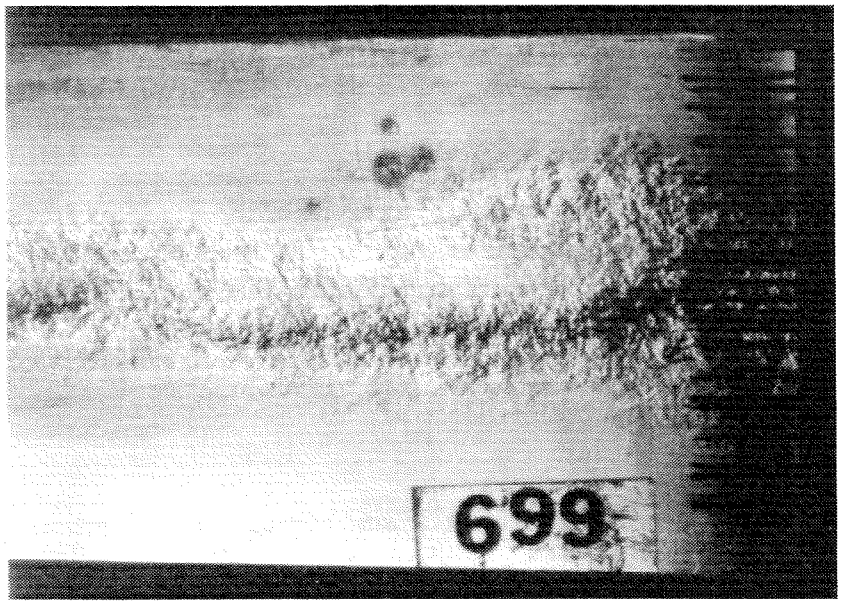

Figure C.19: Schlieren photograph of Case 2h flow (Run 699). Upper stream is low-speed, reactant-rich ($\phi = 8$).

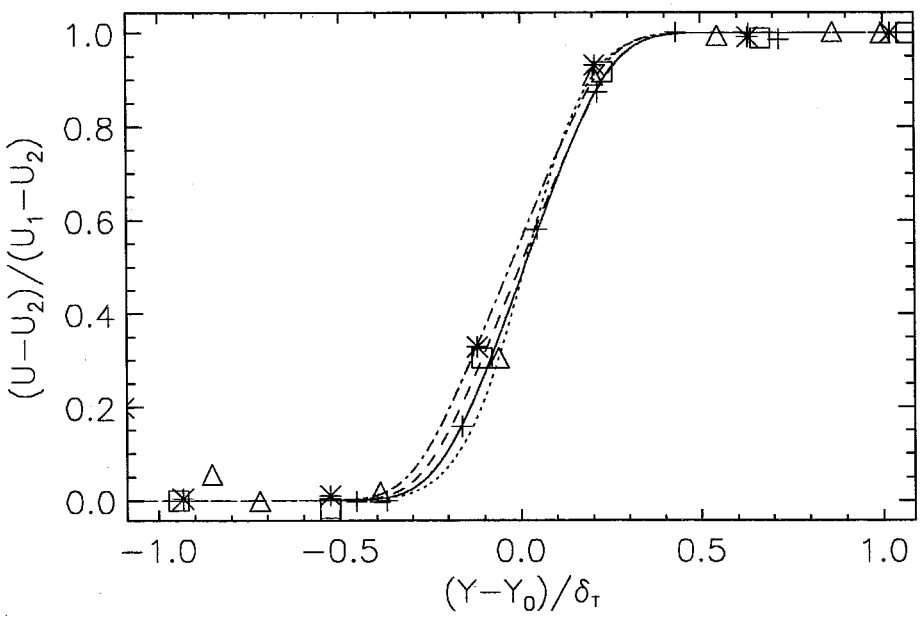

Figure C.20: Normalized velocity profiles, Case 2h flow. Solid line/crosses: Run 692, dotted line/triangles: Run 696, dashed line/boxes: Run 699, dot-dashed line/stars: Run 701. The profile fits for Runs 699 and 701 were constrained by Eq. B.14.

repeating each other. The profile that they have is lopsided with a noticeable hump on one shoulder. This hump suggests that the flow may be bi-stable, with the peak of heat release is shifting (in a binary sense) from one position to the other. These 'hump' cases also have a notably thinner temperature thickness (see Table C.6 or Table C.7), while the velocity profile thickness seems not to be much thinner than that of the Case 1 and 2 flows.

The normalized velocity profiles, Figure C.20, match well despite the large changes in shear layer thickness and temperature-rise profiles.

In one sense, Run 696 is "normal" because the temperature thickness is the closest to the previous values, the profile is tilted away form the reactant-rich freestream, and the profile looks normal. Despite this, since three other experiments at this condition produced different results, this result cannot be seen as anything other than one of many manifestations of an unstable condition.

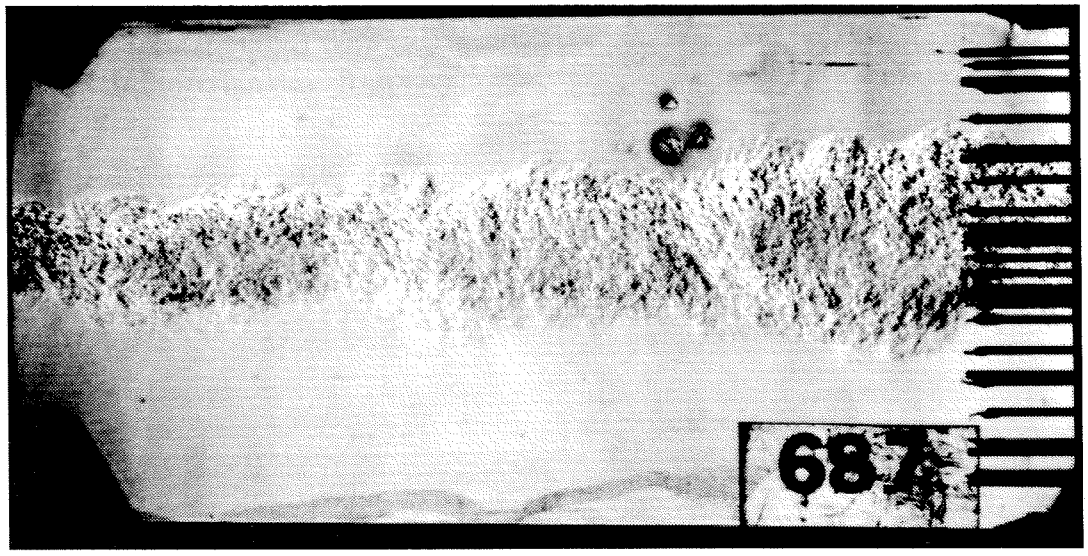

Figure C.21: Schlieren photograph of Case 2f flow (Run 687). Upper stream is low-speed, reactant-lean ($\phi = 1/8$).

The Case 2f experiments may be less susceptible to the curvature-induced instabilities, since the lower heat release would result in weaker curvature (acceleration) induced disturbances. Figures C.21 and C.23 are schlieren photographs of the two

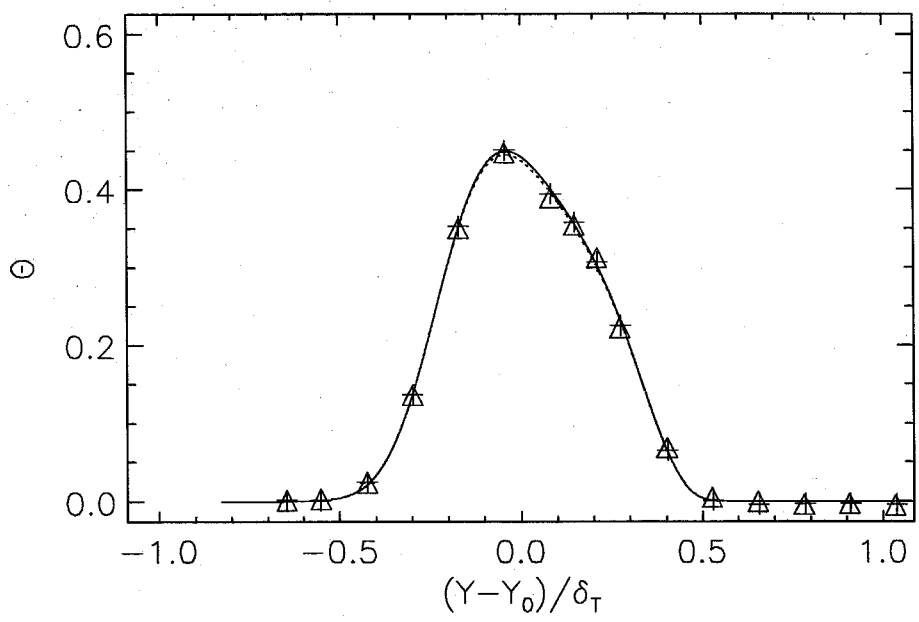

Figure C.22: Normalized temperature-rise profiles, Case 2f. Solid line/crosses: Run 687, dotted line/triangles: Run 689.

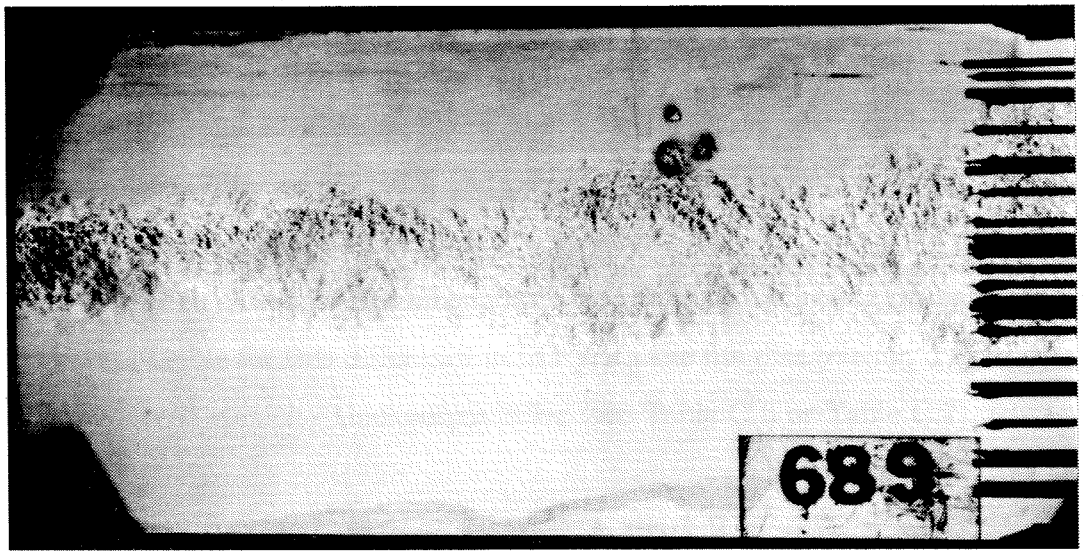

Figure C.23: Schlieren photograph of Case 2f flow (Run 689). Upper stream is low-speed, reactant-lean ($\phi = 1/8$).

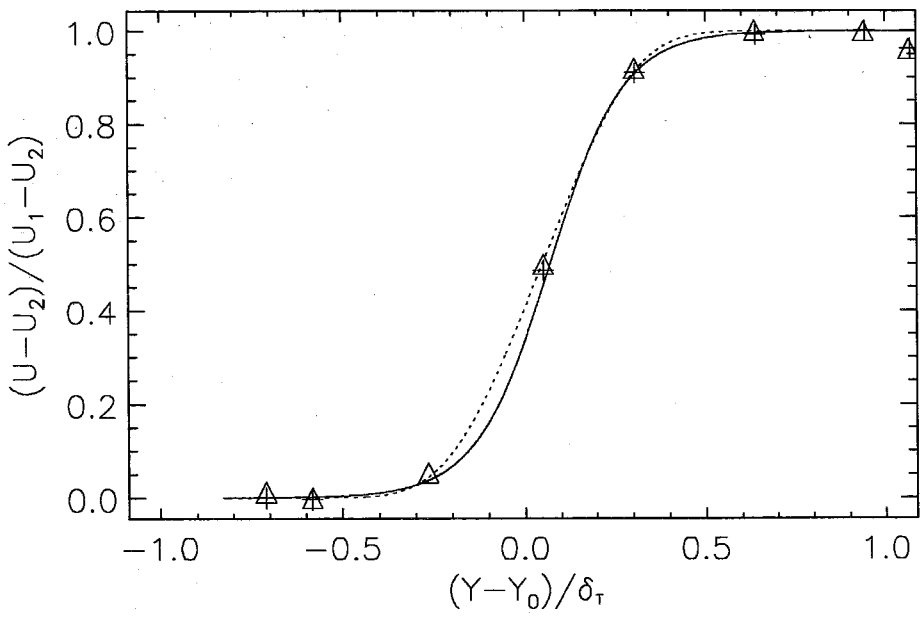

Figure C.24: Normalized velocity profiles, Case 2f. Solid line/crosses: Run 687, dotted line/triangles: Run 689

runs at this condition.

The normalized temperature rises are shown in Figure C.22. The two profiles fit almost directly on top of each other. Although the profile tilts away from the reactant-rich stream (in this case, the high-speed stream), the profile has a bulging high-speed side. The temperature and product thicknesses are nearly identical.

However, the velocity fits (Figure C.24) were somewhat different, although the data points agree closely. A missing point (from a malfunctioning probe in run 687) may be responsible for this difference in fit. With the fits disagreeing, it is no surprise that the inferred vorticity thicknesses differ (see Table C.6 or Table C.7).

C.1.3 Flip experiments: Cases 1 and 2

The experiments presented in this section (the Case 1 and 2 flows) can be used to form estimates of the mixed fluid fraction and a mixed-fluid volumetric composition

δ_m/δ_T $\phi = 1/8$ / $\phi = 8$		1h			2f	
		r693	r695	r697	r687	r689
1f	r688	0.401	0.405	0.427	0.448	0.446
	r691	0.395	0.399	0.421	0.442	0.440
2h	r692	0.380	0.384	0.406	0.448	0.446
	r696	0.375	0.380	0.402	0.422	0.420
	r699	0.417	0.421	0.443	0.464	0.462
	r701	0.417	0.421	0.443	0.464	0.462

Table C.2: Mixed fluid fraction, δ_m/δ_T, inferred from all "flip" experiment pairs in Cases 1 and 2. Flows with $\phi = 8$ are along the left, flows with $\phi = 1/8$ are along the top.

$\mathcal{E}_V$ $\phi = 1/8$ / $\phi = 8$		1h			2f	
		r693	r695	r697	r687	r689
1f	r688	1.50	1.46	1.29	1.16	1.17
	r691	1.47	1.43	1.26	1.13	1.14
2h	r692	1.37	1.33	1.19	1.06	1.07
	r696	1.34	1.31	1.15	1.04	1.05
	r699	1.60	1.56	1.37	1.24	1.25
	r701	1.60	1.56	1.37	1.24	1.25

Table C.3: Volumetric mixed-fluid composition ratio, $\mathcal{E}_V$, inferred from all "flip" experiment pairs in Cases 1 and 2. Flows with $\phi = 8$ are along the left, flows with $\phi = 1/8$ are along the top.

ratio. Although, for completeness, results using the Case 2h flows will be presented, the lack of repeatability makes the values derived thereof questionable. The values from the Case 2h derived results were not presented in the main text.

The mixed-fluid fraction, δ_m/δ_T, is a normalized sum of the product fractions, δ_p, as discussed in Appendix B (Eq. B.7). Table C.2 shows the complete set of calculated mixed-fluid fractions. Since Case 2h flows are suspect (in the sense that they do not repeat well) the important results are in the top two rows. These values lie between 0.395 and 0.448, roughly 10% to 20% below the incompressible value of 0.49 quoted by Dimotakis (1989).

Table C.3 shows the inferred mixed-fluid volumetric composition ratio, $\mathcal{E}_V$ (defined in Appendix B). The values for the 1f-1h "flips" are high, exceeding even the Dimotakis (1986) entrainment ratio value (for $s = 0.38, r = 1.0$) of 1.31. The values

for the 1f-2f "flips", on the other hand, match well with the results of Mungal & Dimotakis (1984),

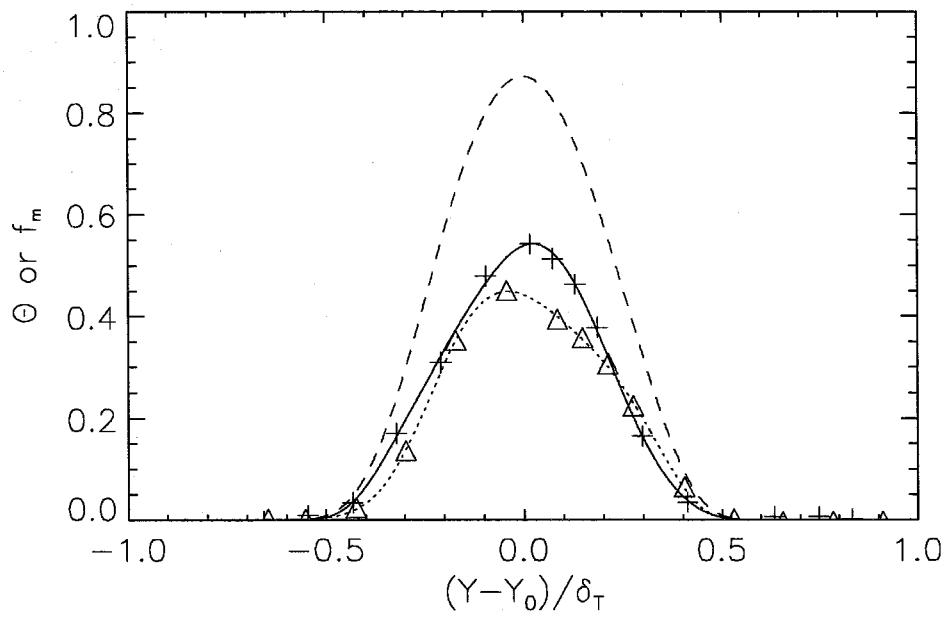

Figure C.25: Normalized temperature and mixed-fluid fraction (dashed line) profiles for "flip" formed by Cases 1f (solid line/crosses: Run 691) and 2f (dotted line/triangles: Run 687).

Temperature profiles for the 1f-2f "flip" are shown in Figure C.25. The two product-profile peaks are shifted from the center (away from the respective reactant-rich streams), but only by, roughly, 2% and 5%. Mungal & Dimotakis (1984) had observed tilts in the product profile of roughly 10% for the same stoichiometry. The profile for Run 687 actually rises above the profile for Run 691 on the high-speed side, where Run 687 should be reactant-rich. Additionally, the converse happens on the low-speed stream. This suggests that temperature-profile centering may not be providing a good comparison of the data here. As a confirmation, look at the velocity profiles for these runs (Figure C.26). Run 687 seems clearly shifted to the right. This suggests that the run 687 profile should be shifted to the left for a better comparison. In the current work, velocity centering has not been used due to the difficulties of

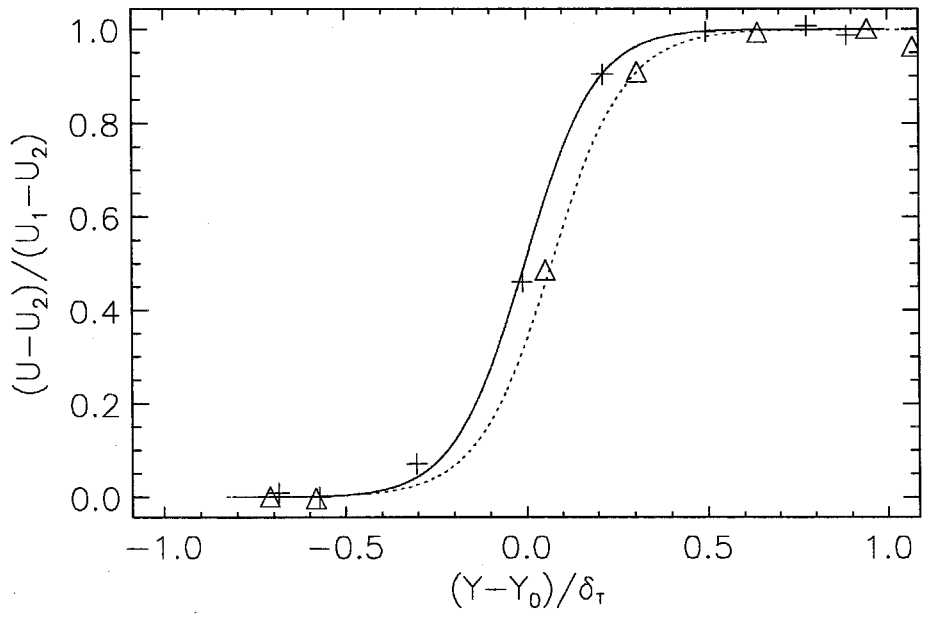

Figure C.26: Normalized velocity profiles, for representative 1f-2f "flip experiment. 1f flow: solid line/crosses (Run 691), 2f flow: dotted line/triangles (Run 687).

accurately fitting the velocity profiles. The dashed line is the inferred mixed fluid fraction as a function of the cross-stream coordinate, y.

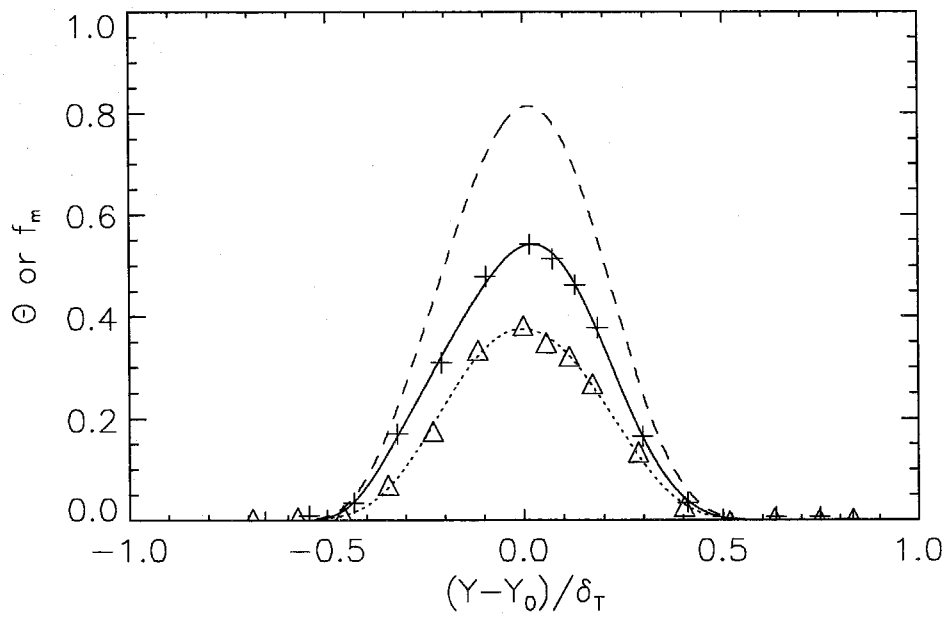

Figure C.27: Normalized temperature and mixed-fluid fraction (dashed line) profiles for "flip" formed by Cases 1f (solid line/crosses: Run 691) and 2f (dotted line/triangles: Run 687).

Temperature profiles for the 1f-1h "flip" are shown in Figure C.27.The two profiles peak at nearly the same coordinate (roughly 2.5% towards the high-speed side) which is unlike previous gas-phase reacting-flow data. Furthermore, the velocity profiles (Figure C.28) also show little shift, suggesting that this result is not a misalignment of the data. The mixed-fluid fraction rises above 80% in the center of the flow.

C.2 Higher Reynolds number: Cases 3 and 4

This case has a nominal density ratio $s = 0.98$ and a nominal velocity ratio $r = 0.4$ with a nominal high-speed stream velocity of 165 m/s. The slightly lower density ratio is caused by the density increase in the $M = 0.5$ high-speed stream.

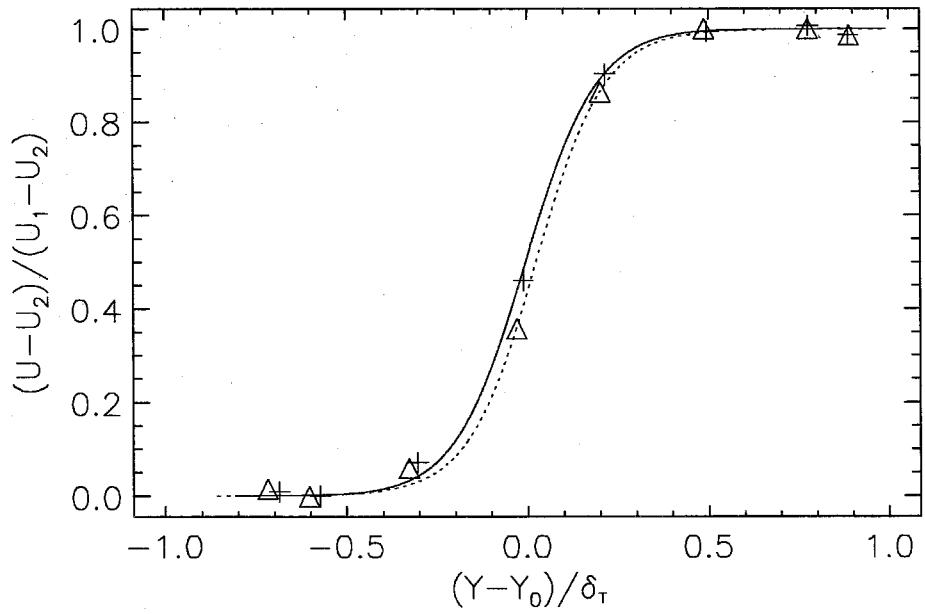

Figure C.28: Normalized velocity profiles, for representative 1f-1h "flip" experiment. 1f flow: solid line/crosses (Run 691), 1h flow: dotted line/triangles (Run 693).

C.2.1 Upper (H_2) stream fast: Case 3

This experiment, with the upper stream operating at a nominal velocity of 165 m/s, comes closest to the design operation of this facility. However, to maintain consistency with the other conditions, the upper-stream supply was operated in the passively controlled (no active feedback) mode.

The temperature profiles for the Case 3c non-reacting runs are shown in Figure C.29. Profiles are shifted so that the center of the fitted velocity profiles (Figure C.31) are at the same location. Although the profiles appear to be shifted, both have a characteristic shape, with a peak in the middle of the shear layer.

Figure C.30 shows an upstream photograph of a Case 3h reacting flow. Like many of the upstream photographs, structure is more difficult to see. In the upstream quarter to half of the image there is evidence that light has been deflected off of the schlieren optics, resulting in dark banding near the splitter plate. Figure C.32

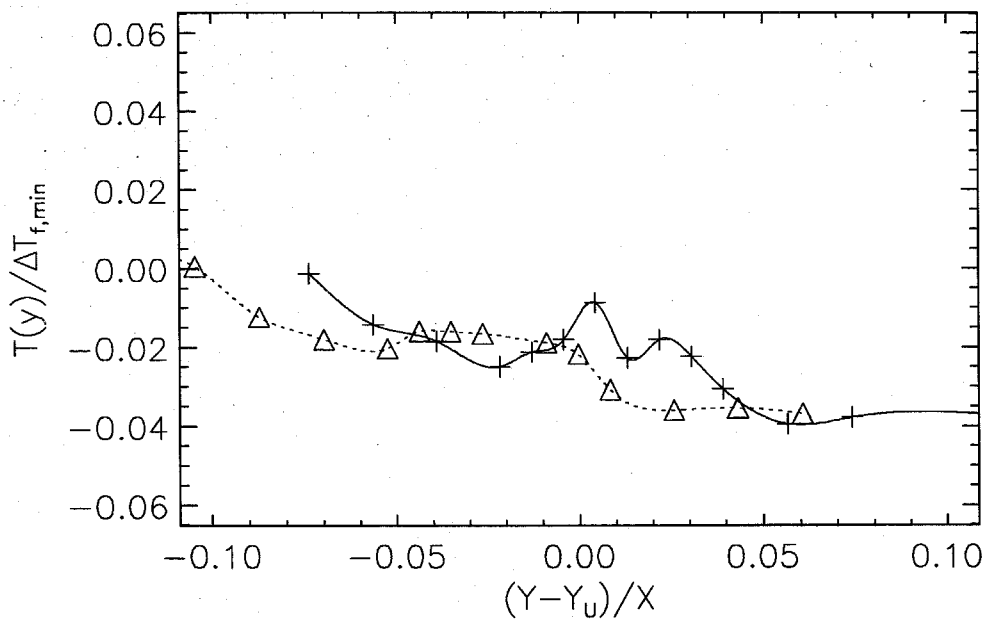

Figure C.29: Measured temperature profiles, Case 3c. Temperatures have been normalized by the smaller of the two adiabatic flame temperature rises in this study. Solid line/crosses: Run 644, Dotted line/triangles: Run 654.

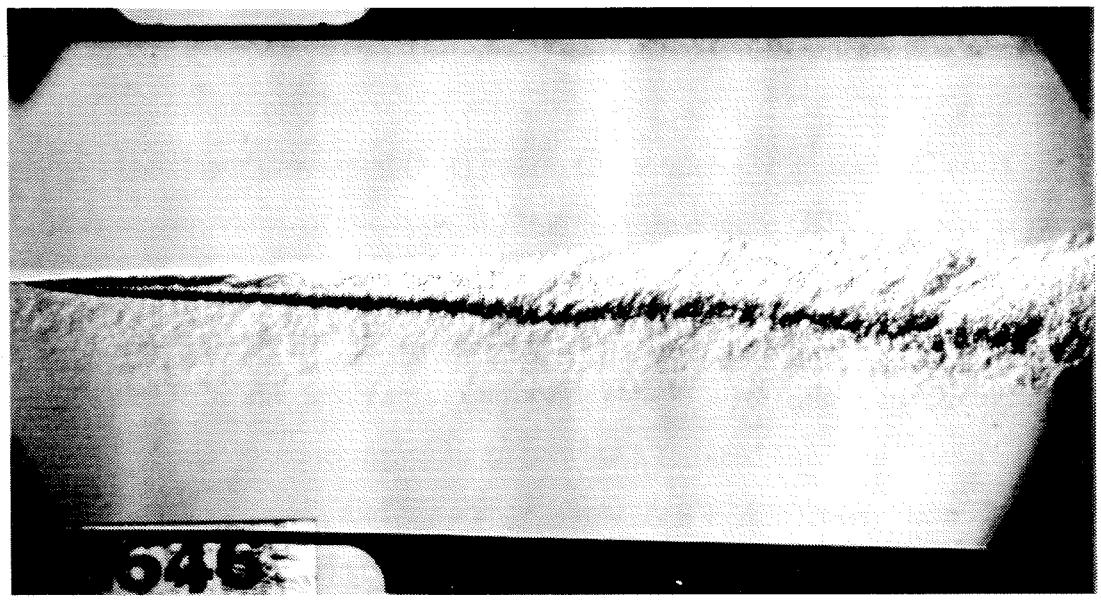

Figure C.30: Schlieren photograph of Case 3h flow (Run 646). Photograph of upstream region of shear layer. Upper stream is high-speed, reactant-rich ($\phi = 1/8$).

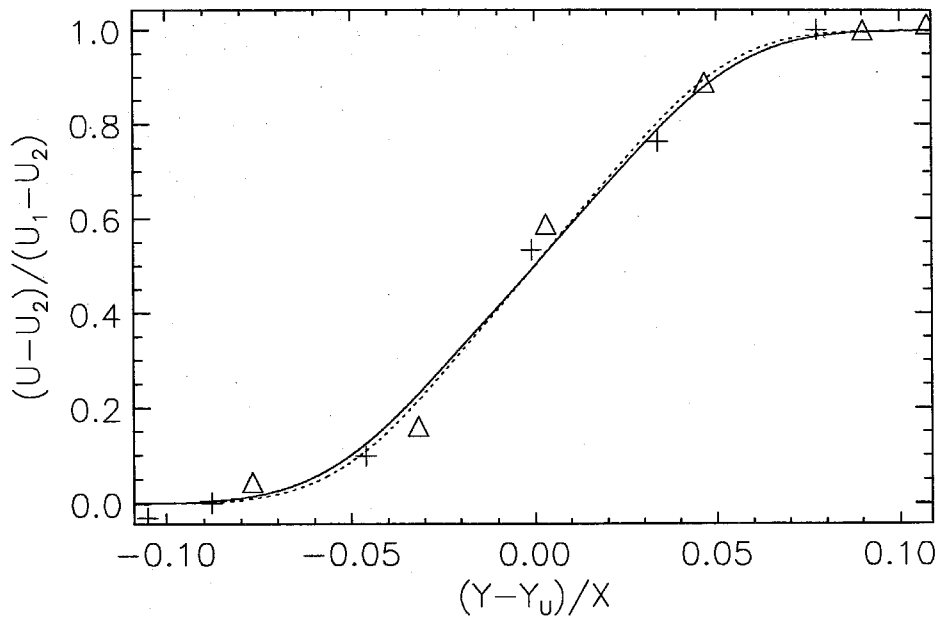

Figure C.31: Normalized velocity profiles, Case 3c. Solid line/crosses: Run 644, dotted line/triangles: Run 654. For these two runs Eq. B.14 constrained the profile fits.

shows a magnified view of the near-splitter-plate region, showing this banding. The distortions that appear to be turbulence in the lower stream are the result of gas from the hydrogen-carrying upper stream leaking around the sides of splitter plate, forming a thin layer of reacted (hot) gas on the windows. Figures C.33 and C.35 show two downstream views of the type 3h/3hk flow. In Figure C.33, the rake is just past the downstream end of the image.

Figure C.34 shows the normalized temperature profiles for the three runs of Cases 3h and 3hk. Run 3hk is a run at the same condition with lower NO concentration and slightly lower F_2 concentrations to provide a reduced chemical-kinetics rate. The three profiles repeat well, and have approximately a 10% tilt away from the reactant-rich (here the high-speed) stream. The velocity profiles (Figure C.36) also show good matching between the flows.

Case 3hk, the kinetics experiment, is in good agreement with the other two cases.

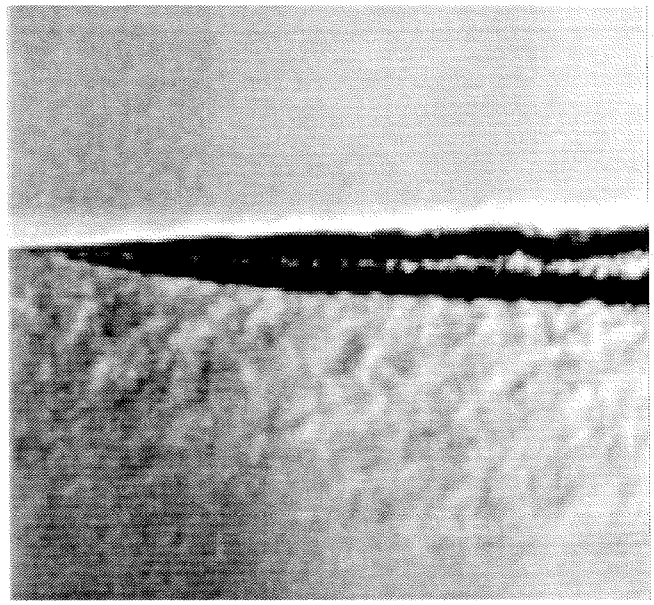

Figure C.32: Magnified view (3x) of splitter tip region of Case 3h flow (Run 646). Upper stream is high-speed reactant rich ($\phi = 1/8$).

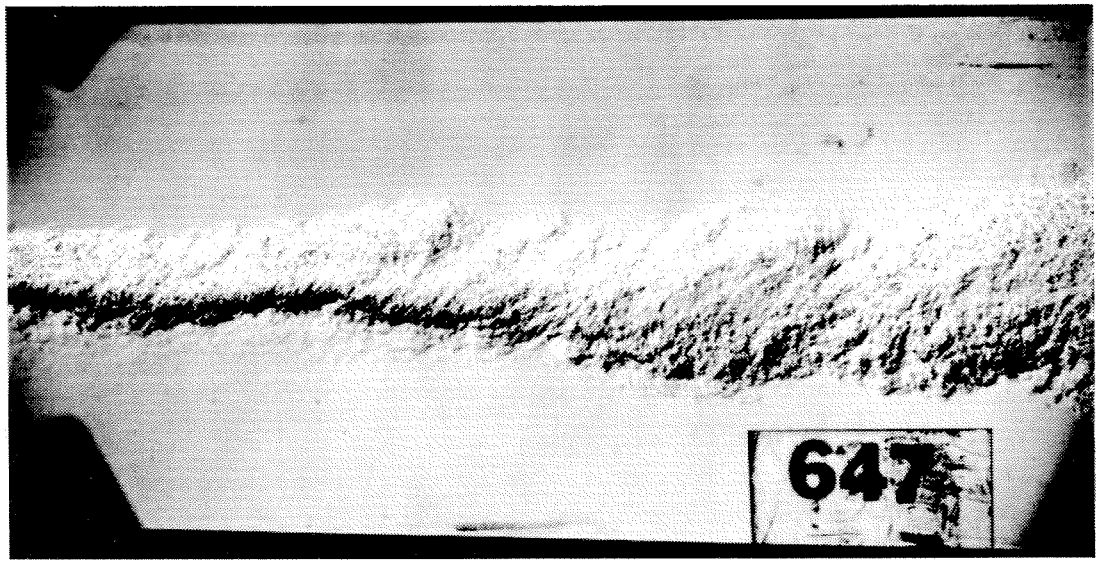

Figure C.33: Schlieren photograph of Case 3h flow (Run 647). Upper stream is high-speed, reactant-rich ($\phi = 1/8$).

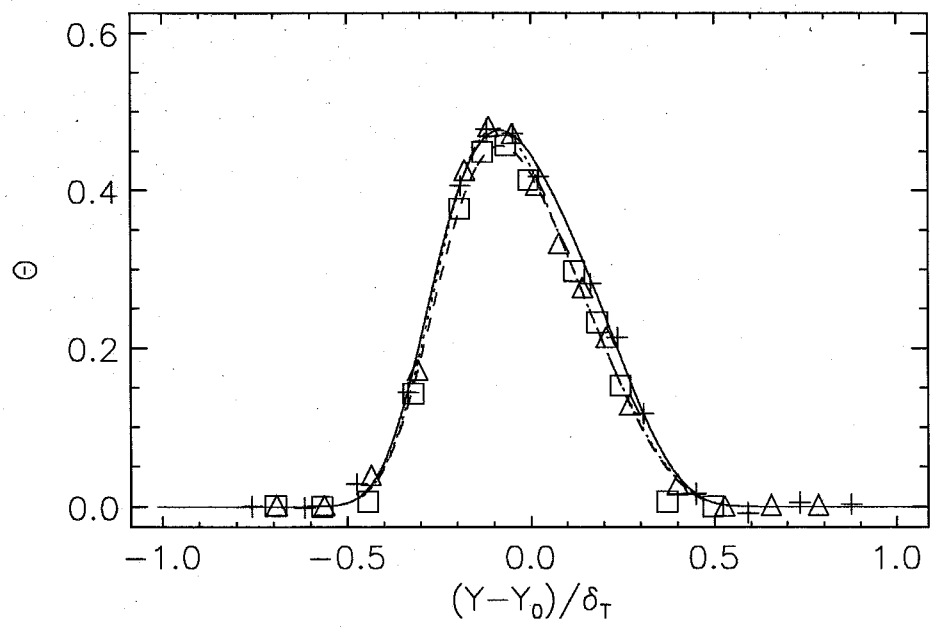

Figure C.34: Normalized temperature profiles, Cases 3h and 3hk. Solid line/crosses: Run 646, dotted line/triangles: Run 647, dashed line/boxes: Run 649.

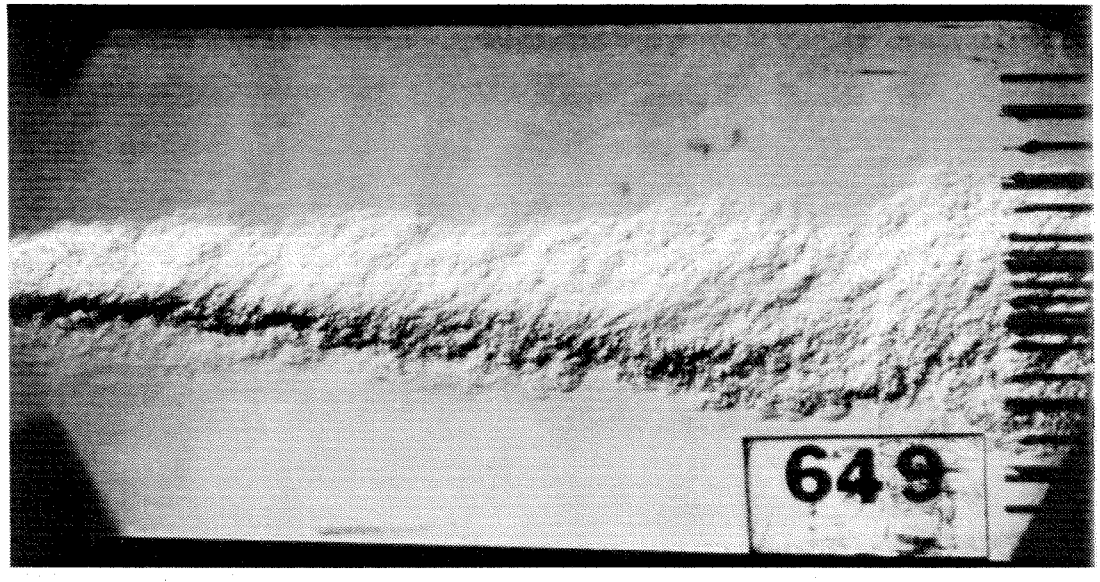

Figure C.35: Schlieren photograph of Case 3hk (Run 649). Upper stream is high-speed, reactant-rich ($\phi = 1/8$). This case is a kinetics test with a reduction in NO concentration.

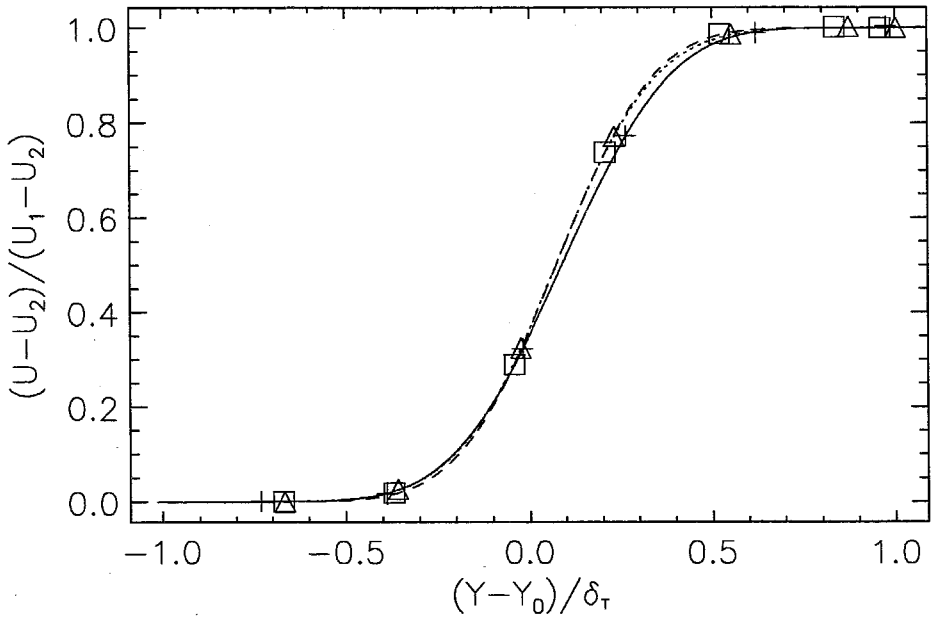

Figure C.36: Normalized velocity profiles, Cases 3h and 3hk. Solid line/crosses: Run 646, dotted line/triangles: Run 647, dashed line/boxes: Run 649.

While the product fraction, δ_p/δ_T, is lower, this is due to a higher temperature thickness. An examination of the temperature profiles (Figure C.34), however, shows that the data points (boxes) in the corners of the profile are below the curve. If the fit were to come closer to these points, the temperature (1%) thickness would be reduced, while the product (integral) thickness would change little. This kinetics test was used to validate the experiments in this chapter, as it was the highest velocity, H_2-rich (F_2-rich is much faster) and preferentially entrains the H_2-carrying stream (Case 4h, with the velocities flipped, preferentially entrains F_2, the lean reactant). Since the results of the experiments agree, and both Da are greater than the fast-chemistry limit ($Da = 5$) of Hall (191), the experiments in this chapter are concluded to be in the mixing-limited regime.

Figure C.37: Schlieren photograph of Case 3f flow (Run 645). Upper stream is high-speed, reactant lean ($\phi = 1/8$).

Schlieren photographs of the F_2-rich Case 3f flows are shown in Figures C.37 and C.39. Both pictures exhibit clear large-scale, two-dimensional structures. The temperature profiles (Figure C.38) show relatively good agreement, but there does appear to be a small systematic difference in the profiles. The velocity profiles (Figure C.40) also show a small difference, although it appears that it might just be a slight shift in the y-coordinate. As shown by the results (Tables C.6 and C.7), there are

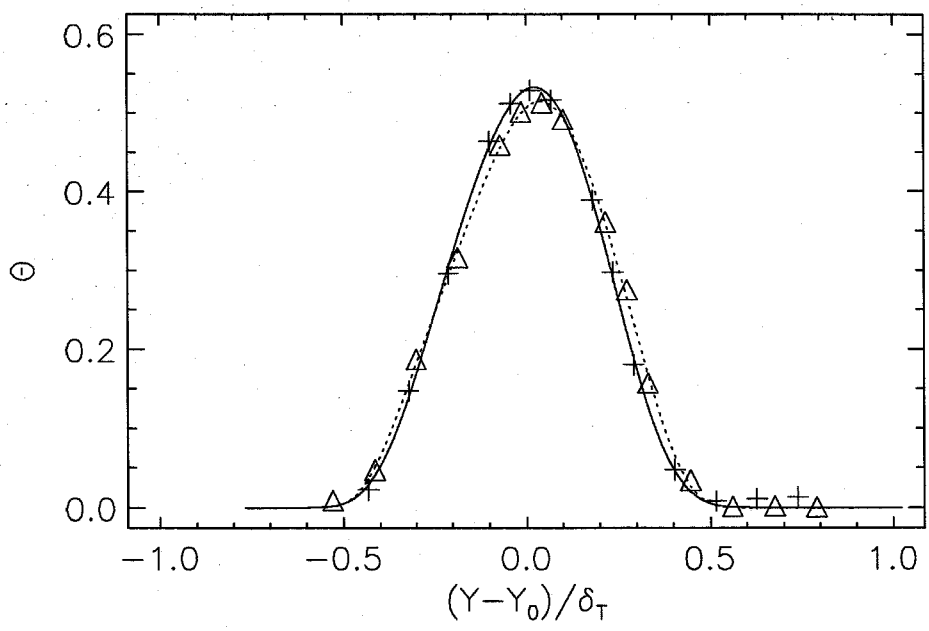

Figure C.38: Normalized temperature-rise profiles, Case 3f. Solid line/crosses: Run 645, dotted lines/triangles: Run 648.

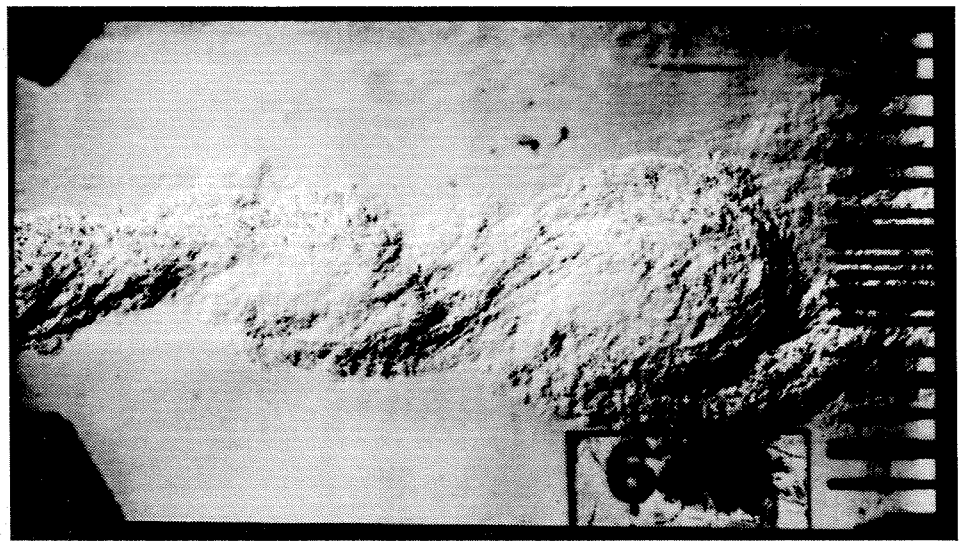

Figure C.39: Schlieren photograph of Case 3f flow (Run 648). Upper stream is high-speed, reactant-lean ($\phi = 1/8$).

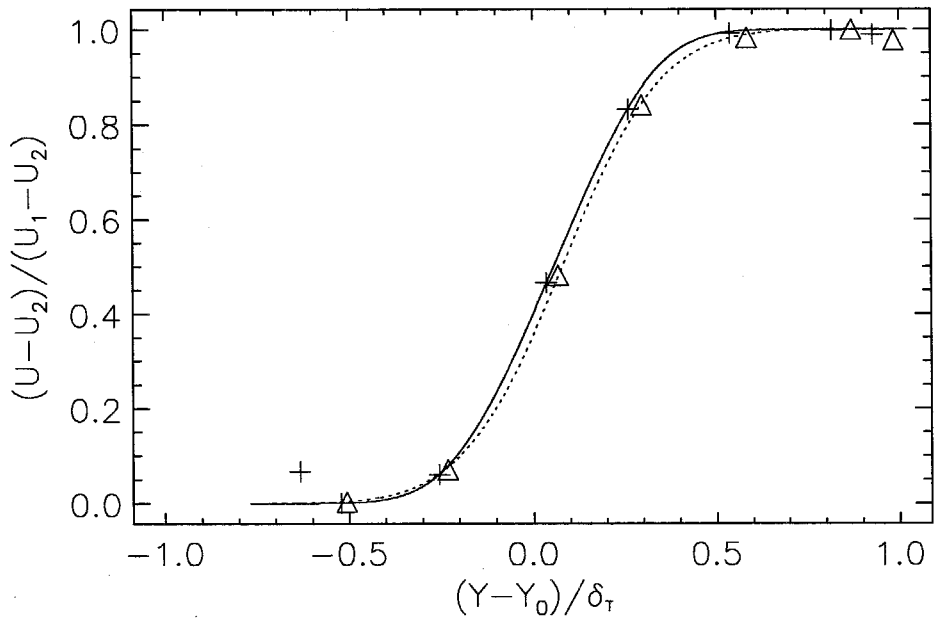

Figure C.40: Normalized velocity profiles, Case 3f. Solid line/crosses: Run 645, dotted lines/triangles: Run 648.

only small differences and those might be caused by the small change in velocity ratio.

C.2.2 Lower (F_2) stream fast: Case 4

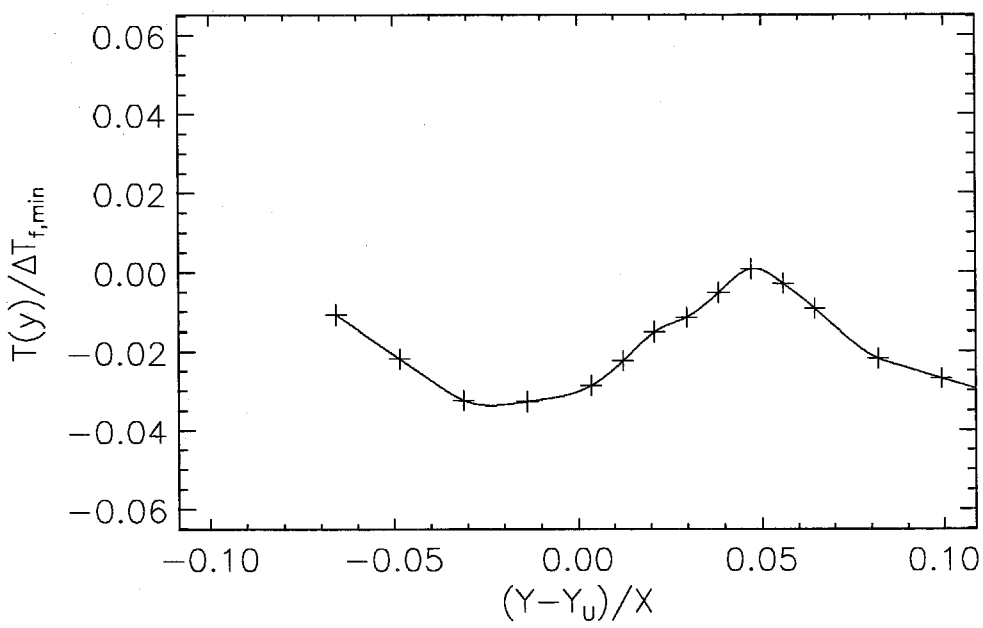

Figure C.41: Measured temperature profile, Case 4c (Run 659). Temperature is normalized by the smallest adiabatic flame temperature rise in this study.

These experiments were performed at close to the lower-stream operating-envelope limits. The run length was only 1.5 s, with approximately 0.7 s of that time being required to bring the flow to a steady state. As with the Case 2 flows, the lower stream is the high-speed stream and this causes difficulties in the near-splitter-plate region of the flow. Specifically, the upper guidewall is held parallel to the upper stream, while the lower-stream guidewall is diverged (in reacting runs, converged in non-reacting runs) to accommodated the dilatation of the reacting flow. The resultant turning of the flow results in curvature of the shear-layer in the near-splitter-plate region.

The Case 4c temperature profile (Figure C.41) shows a distinct peak in the middle of the layer, characteristic of these flows. The velocity profile (Figure C.42), as typical for non-reacting flows, is close to a simple tanh profile.

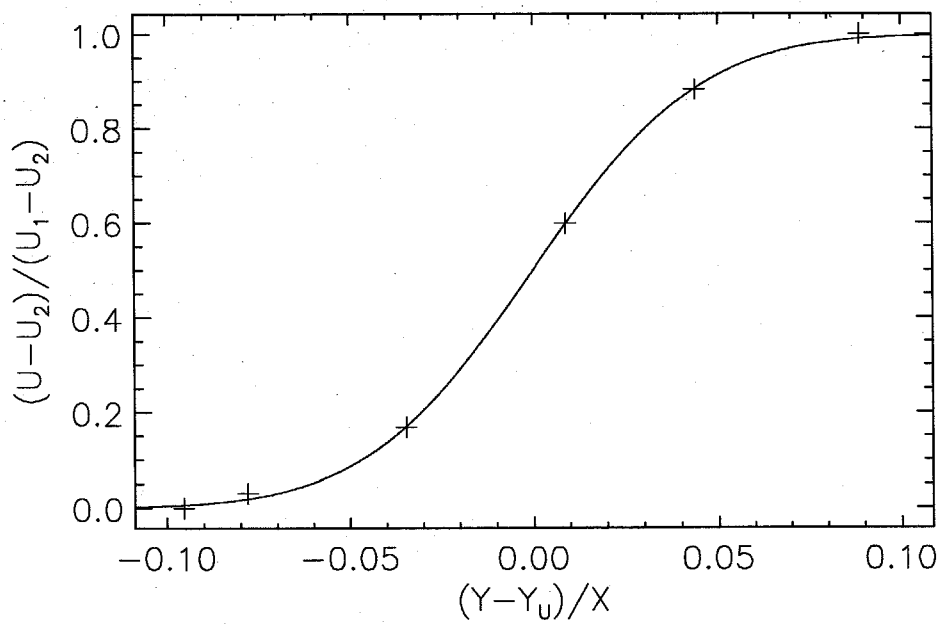

Figure C.42: Normalized velocity profile, Case 4c (Run 659)

Figure C.43: Schlieren photograph of Case 4h flow (Run 662). Upper stream is low-speed, reactant-rich ($\phi = 8$).

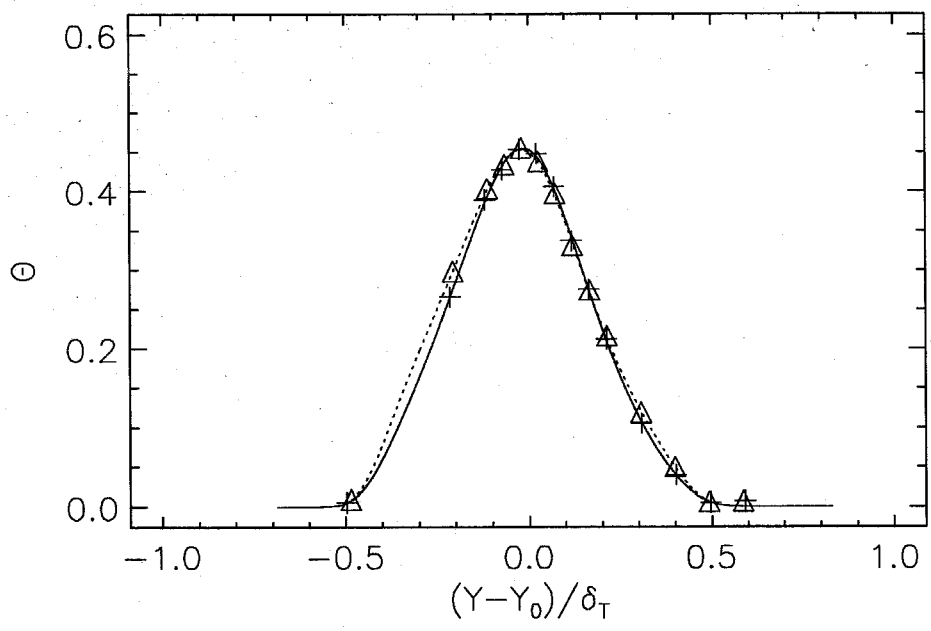

Figure C.44: Normalized temperature-rise profiles, Case 4h. Solid line/crosses: Run 662, dotted line/triangles: Run 663.

Figure C.45: Schlieren photograph of Case 4h flow (Run 663). Upper stream is low-speed, reactant-rich ($\phi = 8$).

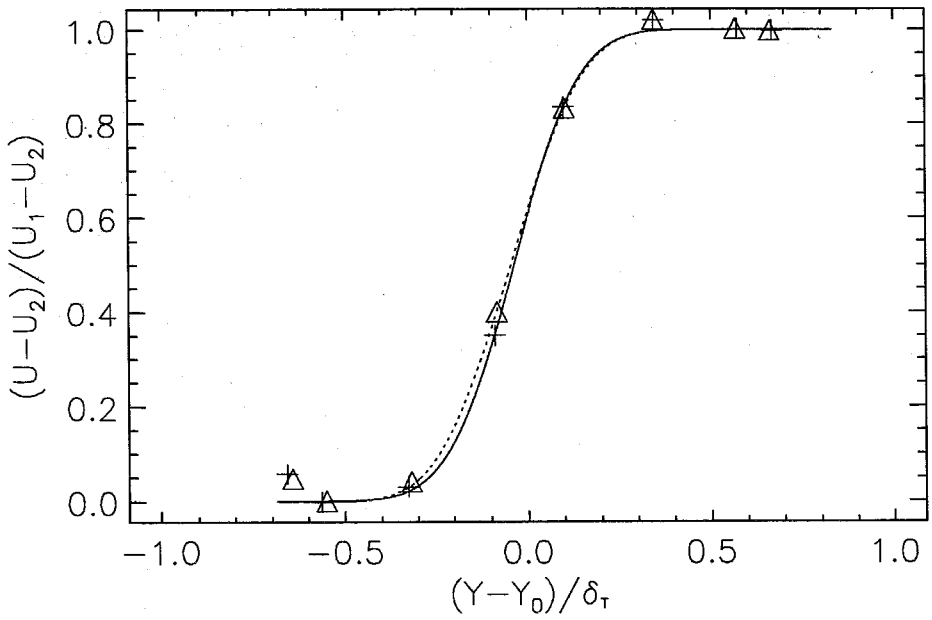

Figure C.46: Normalized velocity profile, Case 4h. Solid line/crosses: Run 662, dotted line/triangles: Run 663.

The photographs from the Case 4h flows (Figures C.43 and C.45) show that the flow is unstable. The shear layer appears to be flapping. This would explain why the temperature thickness, δ_T, is thicker for these cases than for the other (Cases 3h, 3f and 4f) cases at these velocities. Note that although δ_T is higher, the product thickness, δ_p, is comparable to those from Case 3f, despite the variations of the shear layer.

The temperature profiles (Figure C.44) seem to match well, but have few points on the lower-speed side. These profiles have a somewhat lower maximum Θ than the Case 3f profiles, but this may be, as discussed above, because the flow is flapping, spreading the product over a wider range in y. The velocity profiles (Figure C.46) also match well. Despite the large flagellation of the shear layer, the flow seems to be repeatable.

Figure C.47 shows an upstream photograph of the Case 4f, F_2-rich flow. Close

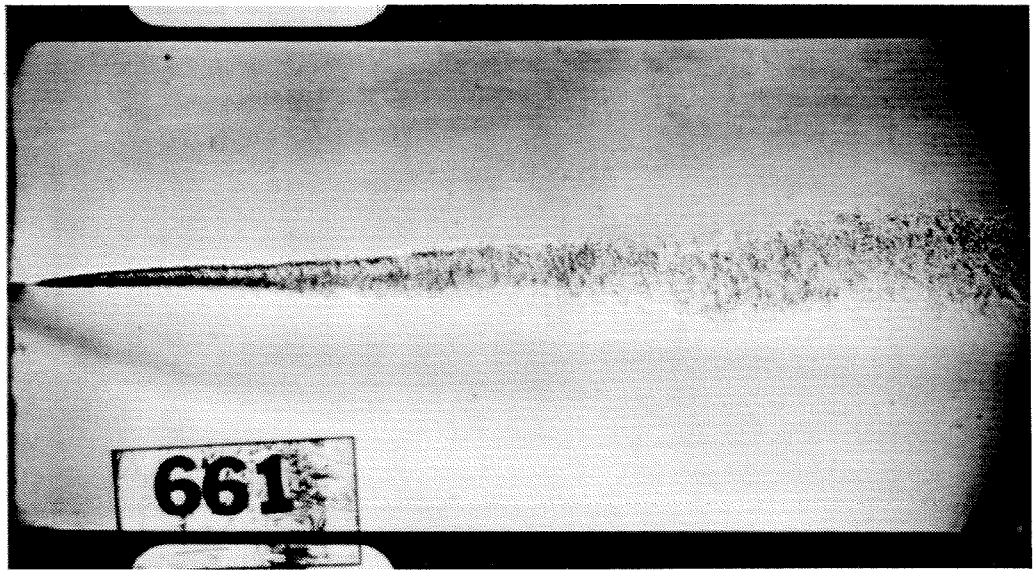

Figure C.47: Schlieren photograph of upstream portion of Case 4f flow (Run 661). Upper stream is low-speed, reactant-lean ($\phi = 1/8$).

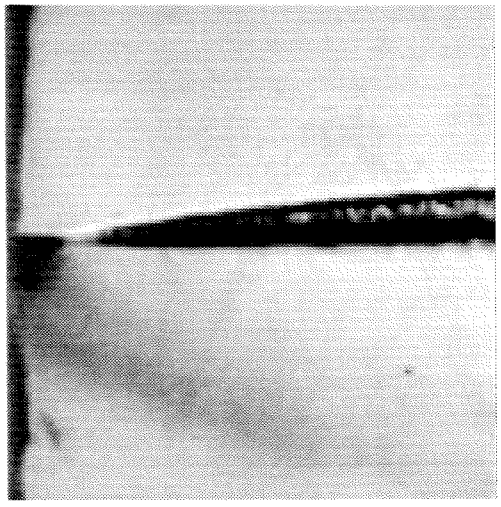

Figure C.48: Magnified (3x) schlieren photograph of splitter-plate region of Case 4f flow (Run 661). Upper stream is low-speed, reactant-lean ($\phi = 1/8$). Notice that the shear layer is growing into the upper stream.

Figure C.49: Schlieren photograph of Case 4f flow (Run 660). Upper stream is low-speed, reactant-lean ($\phi = 1/8$).

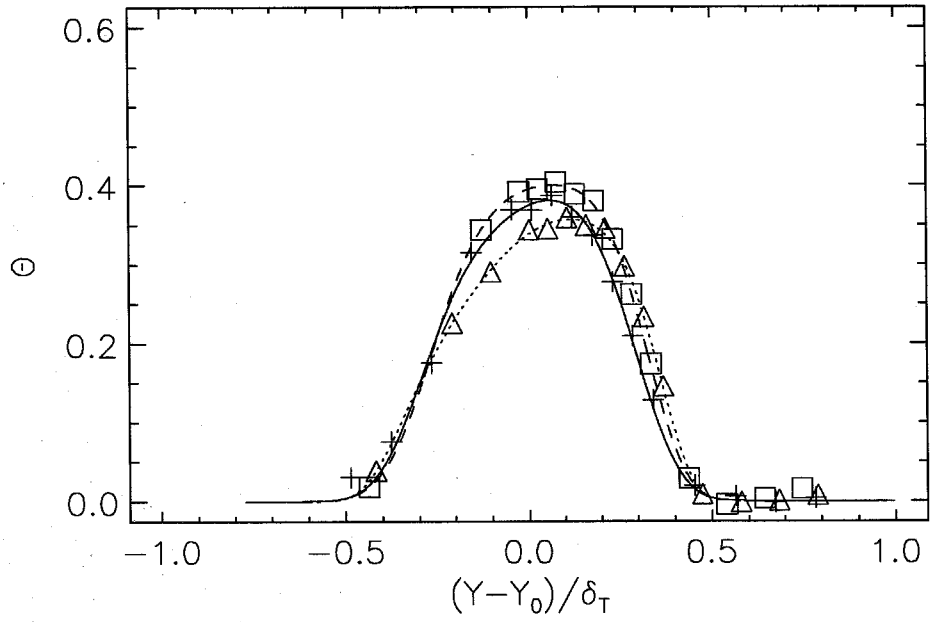

Figure C.50: Normalized temperature-rise profile, Case 4f. Solid line/crosses: Run 660, dotted line/triangles: Run 661, dashed line/boxes: Run 664.

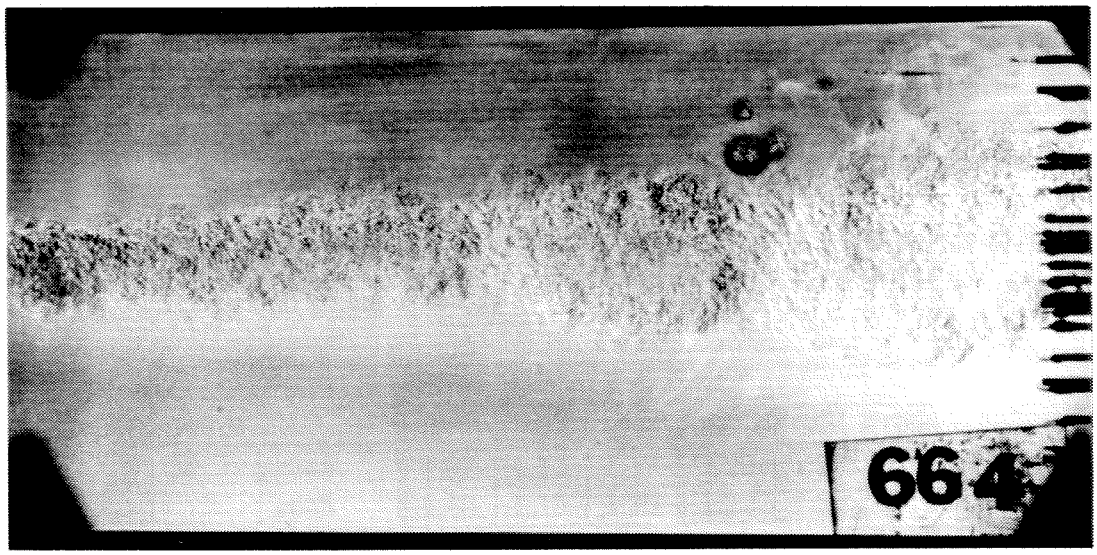

Figure C.51: Schlieren photograph of Case 4f flow (Run 664). Upper steam is low-speed, reactant-lean ($\phi = 1/8$).

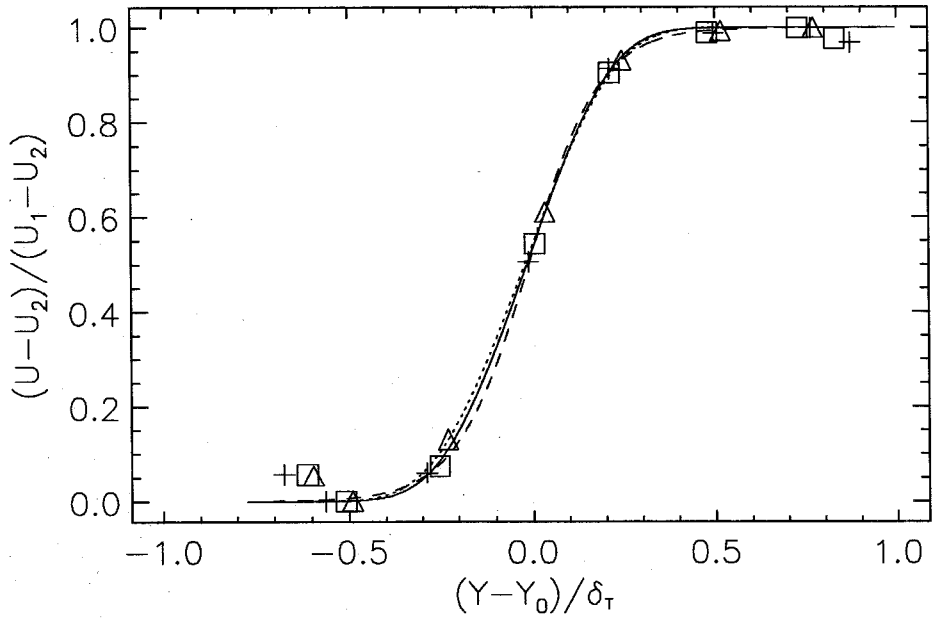

Figure C.52: Normalized velocity profiles, Case 4f. Solid line/crosses: Run 660, dotted line/triangles: Run 661, dashed line/boxes: Run 664.

δ_m/δ_T $\phi = 1/8$		3h		3hk	4f		
$\phi = 8$		r646	r647	r649	r660	r661	r664
3f	r645	0.443	0.430	0.423	0.419	0.421	0.436
	r648	0.446	0.434	0.427	0.423	0.425	0.439
4h	r662	0.398	0.386	0.379	0.375	0.377	0.391
	r663	0.407	0.395	0.388	0.384	0.386	0.400

Table C.4: Mixed fluid fraction, δ_m/δ_T, inferred from all "flip" experiment pairs in Cases 3 and 4. Flows with $\phi = 8$ are along the left, flows with $\phi = 1/8$ are along the top.

$\mathcal{E}_V$ $\phi = 1/8$		3h		3hk	4f		
$\phi = 8$		r646	r647	r649	r660	r661	r664
3f	r645	1.07	1.13	1.17	1.20	1.19	1.10
	r648	1.10	1.15	1.19	1.22	1.20	1.12
3h	r662	0.87	0.91	0.95	0.97	0.96	0.88
	r663	0.92	0.96	1.00	1.02	1.01	0.92

Table C.5: Mixed fluid volumetric composition ratio $\mathcal{E}_v$, inferred from all "flip" experiment pairs in Cases 3 and 4. Flows with $\phi = 8$ are along the left, flows with $\phi = 1/8$ are along the top.

examination of the near-splitter-plate region shows that the shear layer is curved, as expected for this flow. Figure C.48 shows a magnified view of the splitter-plate region. The lower edge of the flow, as it leaves the splitter plate, is nearly parallel to the splitter plate upper surface, which contrasts with Figure C.32, where, with the upper stream as the high-speed stream, the flow grows quickly into the lower stream. Figures C.49 and C.51 show the downstream portion of the Case 4f flow.

The temperature profiles (Figure C.50) show some variation between the runs. The shape of the profile is also strange, both because of its broad, but short form, but also because the peak response is tilted toward the reactant rich freestream. The velocity profiles (Figure C.52)show little difference between the flows. The differences in the temperature profiles show up in the product fraction.

C.2.3 Flip experiments: Cases 3 and 4

For completeness, the mixed-fluid fraction (Figure C.4) and volumetric entrainment ratio (Table C.5) were calculated for all possible flip experiment pairs formed by

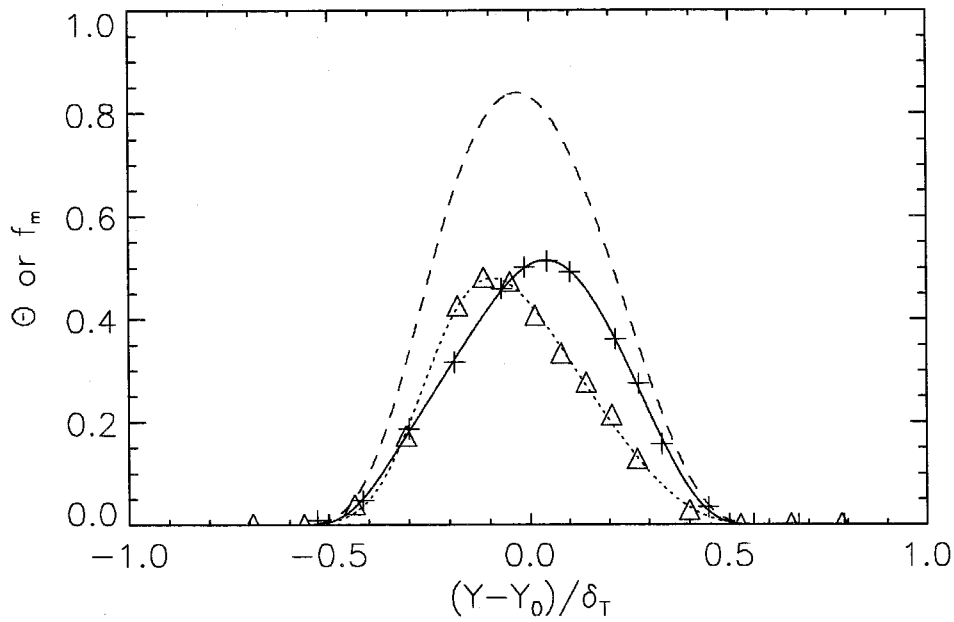

Figure C.53: Normalized temperature-rise and mixed-fluid response (dashed line) profiles for the "flip" formed by Cases 3f and 3h. Solid line/crosses: Case 3f (Run 648), dotted line/triangles: Case 3h (Run 647).

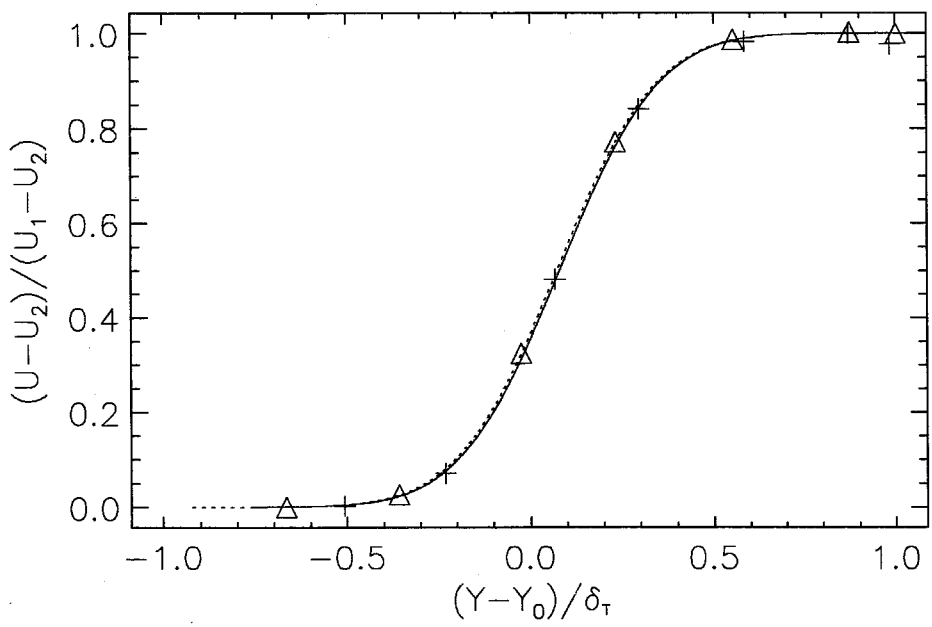

Figure C.54: Normalized velocity profiles, for representative 3f-3h "flip" experiment. Solid line/crosses: Case 3f (Run 648), dotted line/triangles: Case 3h (Run 647)

the Case 3 and 4 flows. However, the results using the Case 4h flows are questionable since it is suspected that the visible flagellation of the layer has inflated the temperature thickness, and thus probably deflated the product fraction from which these statistics have been calculated. Although the profiles of the 4f Cases also present a question as to the nature of the flow, the results using the 4f flows are quite close to those using the 3h and 3hk flows.

Figure C.53 shows the "flip" experiment formed by combining the Case 3f and 3h flows. The peaks of the two temperature-rise profiles are tilted away from their respective reactant-rich freestreams, and the $\phi = 8$ case has a larger area (product fraction), indicating $\mathcal{E}_n > 1$. The mixed fluid response reaches (at its peak) to roughly 80 to 85%. The velocity profiles for this "flip" (Figure C.54) collapse well, indicating that the flow itself seems not to have changed much.

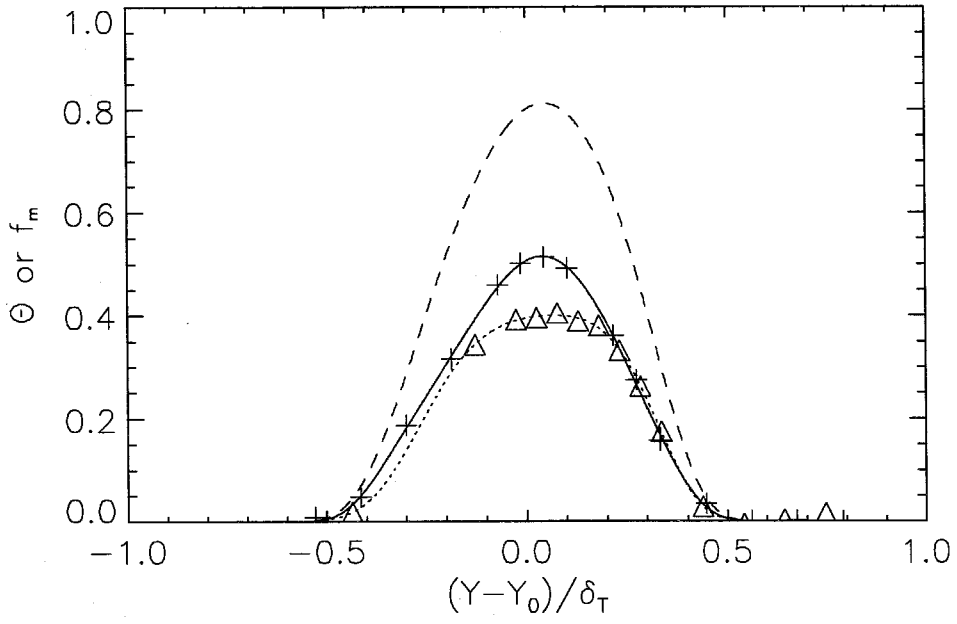

Figure C.55: Normalized temperature and mixed-fluid response (dashed line) profiles for "flip" experiment formed from Cases 3f and 4f. Solid line/crosses: Case 3f (Run 648), dotted line/triangles: Case 4f (Run 664).

The temperature and mixed-fluid profiles from the flip experiment formed by Cases

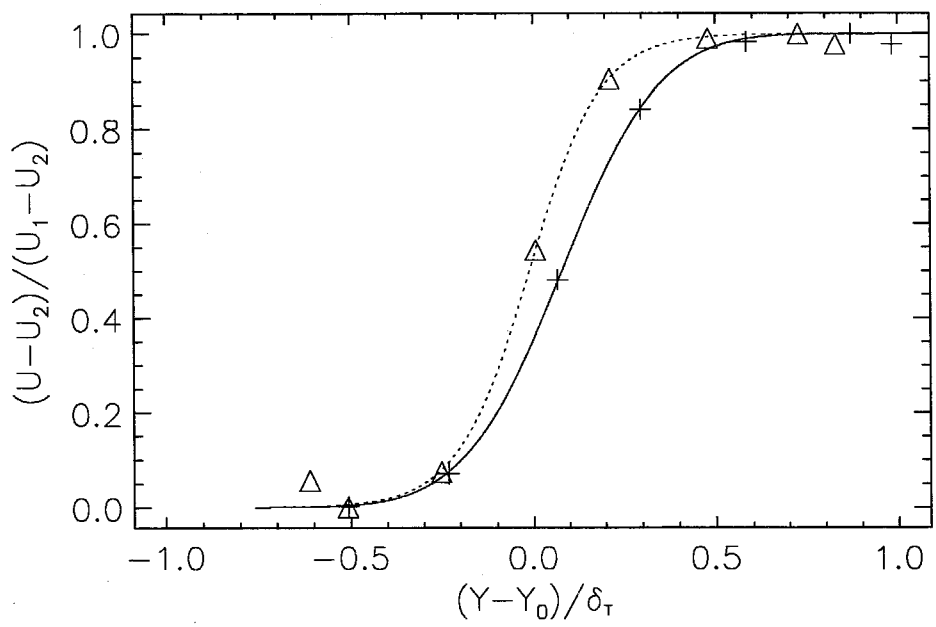

Figure C.56: Normalized velocity profiles from representative 3f-4f "flip". Solid line/crosses: Case 3f (Run 648), dotted line/triangles: Case 4f (Run 664).

3f and 4f are shown in Figure C.55. The peaks of the temperature-rise measurements are both shifted towards the high-speed stream, with little separation (in y) of the maxima. Despite this, the peak of the mixed fluid response reaches just over 80%. The velocity profiles (Figure C.56) are significantly shifted, which indicates a strong change in the flow (which might be the cause of the "backwards" tilt on the Case 4f temperature profile).

Run #	Cond.	U_1	U_2	$\log_{10}(Re_x)$	δ_T/x	δ_p/x	δ_p/δ_T	δ_ω/x	Use
644	3c	165.8	61.4	6.34	-	-	-	0.115	C
645	3f	156.5	62.4	6.29	0.156	0.041	0.262	0.086	TPM
646	3h	165.5	60.3	6.34	0.122	0.029	0.236	0.072	TPM
647	3h	163.8	60.3	6.34	0.136	0.030	0.222	0.072	TPM
648	3f	167.0	60.5	6.35	0.152	0.040	0.266	0.073	TPM
649	3hk	167.7	60.6	6.35	0.139	0.030	0.214	0.073	TPM
654	3c	168.3	55.8	6.38	-	-	-	0.109	C
659	4c	166.8	60.1	6.36	-	-	-	0.090	C
660	4f	168.1	61.2	6.35	0.157	0.033	0.210	0.073	TPM
661	4f	169.4	62.8	6.35	0.166	0.035	0.212	0.081	TPM
662	4h	167.8	61.5	6.34	0.184	0.039	0.212	0.064	TP
663	4h	168.8	59.0	6.36	0.187	0.041	0.222	0.073	TP
664	4f	168.8	59.7	6.36	0.169	0.039	0.228	0.066	TPM
684	2c	101.3	41.2	6.08	-	-	-	0.049	C
685	1c	99.2	40.6	6.11	-	-	-	0.063	C
686	1c	102.2	39.1	6.09	-	-	-	0.067	C
687	2f	100.6	38.0	6.11	0.137	0.032	0.232	0.056	TPM
688	1f	100.1	38.2	6.11	0.164	0.045	0.272	0.061	TPM
689	2f	102.3	39.0	6.11	0.137	0.032	0.230	0.074	TPM
691	1f	95.7	38.6	6.07	0.155	0.041	0.265	0.061	TPM
692	2h	99.5	33.3	6.13	0.208	0.051	0.248	0.098	TP
693	1h	97.8	41.0	6.07	0.151	0.027	0.179	0.055	TPM
695	1h	95.8	35.2	6.10	0.152	0.028	0.184	0.051	TPM
696	2h	101.4	39.5	6.11	0.132	0.032	0.243	0.047	TP
697	1h	98.5	37.8	6.10	0.135	0.028	0.209	0.065	TPM
699	2h	100.9	39.4	6.10	0.104	0.030	0.290	0.055	TP
701	2h	100.8	41.2	6.09	0.107	0.031	0.290	0.057	TP

Table C.6: List of results by run. Use column indicates how the data was used in the main text: C means cold run temperature reference, T indicates temperature thickness P indicates product thickness and fraction M indicates used as part of mixed fluid estimates.

Cond.	Run #	U_1	U_2	$\log_{10}(Re_x)$	δ_T/x	δ_p/x	δ_p/δ_T	δ_ω/x	Use
1c	685	99.2	40.6	6.08	-	-	-	0.063	C
	686	102.2	39.1	6.11	-	-	-	0.067	C
1h	693	97.8	41.0	6.07	0.151	0.027	0.179	0.055	TPM
	695	95.8	35.2	6.10	0.152	0.028	0.184	0.051	TPM
	697	98.5	37.8	6.10	0.135	0.028	0.209	0.065	TPM
1f	688	100.1	38.2	6.11	0.164	0.045	0.272	0.061	TPM
	691	95.7	38.6	6.07	0.155	0.041	0.265	0.061	TPM
2c	684	101.3	41.2	6.09	-	-	-	0.049	C
2h	692	99.5	33.3	6.13	0.208	0.051	0.248	0.098	TP
	696	101.4	39.5	6.10	0.132	0.032	0.243	0.047	TP
	699	100.9	39.4	6.11	0.104	0.030	0.290	0.055	TP
	701	100.8	41.2	6.09	0.107	0.031	0.290	0.057	TP
2f	687	100.6	38.0	6.11	0.137	0.032	0.232	0.056	TPM
	689	102.3	39.0	6.11	0.137	0.032	0.230	0.074	TPM
3c	644	165.8	61.4	6.34	-	-	-	0.115	C
	654	168.3	55.8	6.38	-	-	-	0.109	C
3h	646	165.5	60.3	6.34	0.122	0.029	0.236	0.072	TPM
	647	163.8	60.3	6.34	0.136	0.030	0.222	0.072	TPM
3hk	649	167.7	60.6	6.35	0.139	0.030	0.214	0.073	TPM
3f	645	156.5	62.4	6.29	0.156	0.041	0.262	0.086	TPM
	648	167.0	60.5	6.35	0.152	0.040	0.266	0.073	TPM
4c	659	166.8	60.1	6.36	-	-	-	0.090	C
4h	662	167.8	61.5	6.34	0.184	0.039	0.212	0.064	TP
	663	168.8	59.0	6.36	0.187	0.041	0.222	0.073	TP
4f	660	168.1	61.2	6.35	0.157	0.033	0.210	0.073	TPM
	661	169.4	62.8	6.35	0.166	0.035	0.212	0.081	TPM
	664	168.8	59.7	6.36	0.169	0.039	0.228	0.066	TPM

Table C.7: List of results by condition. Use column indicates how the data was used in the main text: C means cold run temperature reference, T indicates temperature thickness P indicates product thickness and fraction M indicates used as part of mixed fluid estimates.